# Magnetic Properties from Density-Functional Theory Calculations

*A THESIS*

*submitted by*

JOSEPH BLAKE

*for the award of the degree*

*of*

DOCTOR OF PHILOSOPHY



Department of Physics

Royal Holloway, University of London

August 2021

*If you're going through hell, keep going.*


WINSTON CHURCHILL

*To, my family and friends.*

# Declaration

This is to certify that the thesis, and contents within, titled Magnetic Properties from Density-Functional Theory Calculations, to Royal Holloway, University of London, for the award of the degree of Doctor of Philosophy, is my own work. Where I have used/consulted others work, I have clearly stated.

Signature: Joseph Blake

Printed Name : Joseph Blake

Date: 10th August 2021

# Acknowledgements

# Abstract

Magnetic systems are the cornerstone of contemporary life, with their unavoidable use in everyday routines. This fundamental dependency drives the exploration for materials that exhibit both advantageous and distinctive magnetic properties. At the same time, familiar materials are subjected to ever more intelligent experimentation: further understanding the more complex magnetic phenomena present. Additionally, computational advancements have led to an increase in the complexity of theoretical examinations. Thus, first-principles calculations stand uniquely poised, ready with ever-increasing improvements, to understand the characteristics of these magnetic materials.

Double-perovskites exhibit complex and beneficial magnetic relationships, for instance, colossal magnetoresistance. The synthesised $Tl_2NiMnO_6$ experimentally broke the trend by manifesting ferromagnetic insulation. First-principle calculations using electronic band structures, density of states and the effective masses of holes and electrons have predicted the material to be a ferromagnetic semiconductor. Effective masses of holes and electrons revealed insight into the transport properties, unveiling anisotropy potentially linked to the colossal magnetoresistance present in the material.

Molecular magnets are versatile in their application of spintronics, making them a popular choice for investigating. We complete first-principles calculations on the $Cr_{10}(OMe)_{20}(O_2CCMe_3)_{10}$ ($Cr_{10}$), and $Cr_8F_8(CH_3)_3CCO_2H$ ($Cr_8$) molecular rings to investigate the different magnetic states, using $Cr_8$ as a comparison for the frustrated next-nearest neighbour interaction in $Cr_{10}$. We use ionic constraints to enforce $D_5$ symmetry in the $Cr_{10}$ molecule, allowing for reliable extraction of the exchange interaction pa-

rameter and comparable spin-densities. The $Cr_{10}$ molecule possesses a ferromagnetic ground state with the potential for non-co-linear spin-wave excitations whose wavelength is commensurate with the ring.

The iron pnictides superconductors, FeAs and FeSe, simultaneously exhibit complex magnetic interactions, forming a spin-wave. We perform electronic band structure calculations on three competing magnetic arrangements with the meta-GGA, rSCAN, utilising a cold-smearing scheme, revealing, for FeAs, a band gap with Fermi level located inside: completely different from previous first principle band structures. Further reported is the dependency of the strength of magnetism exhibited to the number of magnetic sites present and the direction of the magnetic arrangement.

# Table of Contents

# List of Tables

# List of Figures

# Chapter 1

# Introduction

## 1.1  Magnetism

A significant amount of modern-day science depends upon probing materials with varying particles to discern their microscopic and macroscopic properties. Of these materials, magnetic ones pose a wide range of exciting and beneficial phenomena. There is an ever-growing number of experimental devices and techniques to achieve this insight, such as Mössbauer, X-ray, neutron spectroscopies, SQUID magnetometer, electron paramagnetic resonance and scanning microscopes. A combination of these methods provides a comprehensive picture of the magnetic behaviour exhibited by materials. Unfortunately, theoretical works have struggled to catch up as a result of the computational demand. However, in recent years, computing advancements in speed and memory have increased the complexity of theoretical calculations. Therefore, allowing theoretical investigations to support and offer explanations to the magnetic phenomena observed as well as make predictions for experimental verification.

Magnetism is the physical phenomenon where electrons, with either $+\frac{1}{2}$ or $-\frac{1}{2}$ spin, occupy in unequal numbers an orbital (typically d and f orbitals) in such quantities to generate a magnetic moment.

Magnetism is not a new phenomenon. It has captured the imagination and sparked the curiosity of humans for thousands of years. From the combination of both those fundamental blocks of science came magnetic tools. Since the ancient Greeks, the rare formation of magnetite ($Fe_3O_4$)

was used as the famous lodestone to act as a compass or a leading stone [1].

It is only in the last 100 years or so that the fantastic properties of magnetic materials have led to technologies that brought about the most significant societal advancements in human history [2]. Therefore, understanding the ground state properties of the magnetic materials to allow for manipulation is of the utmost importance.

## 1.2   An Incompatibility with Classical Physics

For the complete description of magnetism, utilising an *ad hoc* approach with a classical description and relevant quantum mechanical corrections is insufficient. It was shown in the 1930s by Bohr and van Leeuwen [3] that magnetism is unintelligible within the structure of rigorous classical theory with moving charges. This feature becomes apparent through the use of thermodynamics and statistical mechanics. A classical Hamiltonian of N particles possessing charges $e$ and masses $m$ in a magnetic field ($\mathbf{A}$) takes the form:

$$H = \sum_{i=1}^{3N} \frac{1}{2m} (p_i - \frac{e}{c}\mathbf{A}_i)^2 + V(\mathbf{q}_1, \mathbf{q}_2, \cdots, \mathbf{q}_N) \tag{1.2.1}$$

where $\mathbf{p}_i$ and $\mathbf{q}_i$ are canonical momenta and coordinates, $c$ is the velocity of light and $V$ is the interaction potential. The classical partition function becomes;

$$Z = \int_{-\infty}^{+\infty} e^{\beta V} \int_{-\infty}^{+\infty} \exp\left( -\frac{\beta}{2m} \sum_{i=1}^{3N} (p_i - \frac{e}{c}\mathbf{A}_i)^2 \right) dq_1, \cdots, dq_{3N} dp_1, \cdots, p_{3N} \tag{1.2.2}$$

where $\beta = 1/k_B T$ and $k_B$ is the Boltzmann constant. The partition function is independent of the magnetic field, only when the magnetisation, $M$, is

represented as:

$$M = k_B T \frac{\partial}{\partial H} \ln(Z) \tag{1.2.3}$$

disappears. The magnetisation going to zero is incompatible with physical observations of magnetism and, therefore, classical Physics cannot explain the phenomenon of magnetism [4]. Therefore only quantum mechanical methods can represent magnetic materials; putting importance on the success and accuracy of those methods.

## 1.3 The Local Moment Picture

There are two main branches for explaining magnetism within a system: the local moment picture and itinerancy. These competing models of explanation were the subject of controversy for decades when concerning the 3d- transition metals. However, it was only through probing the Fermi surfaces and band structures of the d-electrons [5] in the transition metals that concluded the controversy: the d-electrons in transition metals are itinerant [6, 7]. The itinerancy of electrons signifies that they can transfer from one atom to the next. The ground state properties of itinerant magnets are fairly well-described by band theory, putting importance upon electronic structure calculations.

The local moments model is, as its namesake suggests, based upon the principle where the electrons responsible for magnetism are localised to an ion. Thus, the representation of localised magnetism conforms to the Heisenberg Model. Furthermore, local moments are usually associated with magnetic insulators, owing to the Mott mechanism for strong electron-electron correlation.

In the Heisenberg model for localised moments, meeting the above requirements, the exchange interaction obeys the Anderson-superexchange [8], favouring a negative sign indicating short-ranged antiferromagnetic or-

dering.

Another model which describes long-distance exchange is the Ruderman-Kittel-Kasuya-Yosida interaction [9–11]. This interaction involves localised 4f electrons and conduction electrons, which results in a hybridised narrow band.

## 1.4 Itinerant Magnetism

Itinerant magnetism is the contrary behaviour to the local moment picture. Itinerancy in a system arises from magnetic ions which constitute an alloy or an intermetallic aggregate. In these instances, the unpaired electrons are not subject to only accommodate energy levels about a single magnetic ion. Instead, the unpaired electrons are delocalised as the original energy levels have broadened to narrow bands. The interatomic separations determine the size of the broadening. There are many well-known cases of itinerant magnetism from the 3d transition metals, whereby the magnetic properties are directly caused by the 3d electrons.

### 1.4.1 Stoner Theory

There are many detailed descriptions of Stoner theory, so this will be a brief description of the main results and uses of the Stoner criterion [12–14]. Stoner theory is a means to describe the mechanism behind and determining if a material is ferromagnetic or will become ferromagnetic. The theory is based on a simple band model of materials including effective exchange energy, the energy gained when spins flip from anti-parallel to parallel and the density of states. From these quantities, the Equation 1.4.1 can be formed and used.

$$U_{\text{eff}} N(E_{\text{F}}) > 1 \qquad (1.4.1)$$

Where $N(E_\mathsf{F})$ is the density of states at the Fermi level.

For a 3d transition metal, if $[1 - U_{\mathrm{eff}} N(E_\mathsf{F})] > 0$, then the lowest energy state corresponds to no electrons moving from spin-down bands to spin-up bands and the system is non-magnetic. If $[1 - U_{\mathrm{eff}} N(E_\mathsf{F})] < 0$, the 3d bands are exchange-split and the system is ferromagnetic.

Stoner theory still provides computational success and a good description of materials [15].

## 1.5   Thesis Outline

In this work, we perform first-principles calculations to determine the magnetic phenomena in complex magnetic systems[1][2]. The overviews of the chapters are as follows:

### Chapter 2

The many-body Schrödinger equation is introduced, and the approximations made to develop it into the density-functional theory framework for ground state calculations are discussed. The impact of the choice of exchange-correlation functional and pseudopotential have on the Kohn-sham equation are mentioned. A brief introduction to the computational format which the CASTEP code [16] uses to achieve first principles is explored. The density-functional theory framework is expanded to the *ad-hoc* format, which includes magnetism. Core magnetic concepts are discussed and lead into a description of complex magnetism.

### Chapter 3

This chapter details a first-principles investigation into the electronic structure of the double perovskite, $Tl_2NiMnO_6$, to ascertain its conducting and

magnetic properties. The effect of colossal magnetoresistance on the system is explored, and through curve fitting to the band structure, the effective masses of the carriers are determined.

## Chapter 4

The magnetic complexity of the single molecular magnet, $Cr_{10}$, is investigated in this chapter alongside the $Cr_8$ molecule. First, the symmetry of the molecule is explored through two branches of $C_1$ and $D_5$ point groups. Ionic constraints are used to ensure the $D_5$ point group was maintained while investigating the ground state magnetic arrangement. Next, the effective exchange interaction is determined through the broken symmetry approach while exploring the differences between exchange-correlation functionals, LDA, PBE and rSCAN. Using the fixed spin moment constraint on the DFT calculations allowed for the determination of the ground state magnetic structure which disagreed with experiment. Spin density isosurfaces showed subtle differences between the XC functionals and highlighted the influence of the frustrated next-nearest neighbour interactions of the $Cr_{10}$ molecule. Finally, the possibility of magnetostriction within the molecular magnet was explored through a magnetostrictive force.

The non-frustrated next nearest neighbour exchange interactions of the $Cr_8$ molecule allowed for a comparison with $Cr_{10}$ and provided insight into the suitability of the nearest neighbour Heisenberg model.

## Chapter 5

The effects of the different XC functionals, LDA, PBE and rSCAN, on the complex bond-dependant magnetism in the iron pnictide, FeAs, is investigated. Through geometric optimisations, the performances of the functionals are compared via the lattice parameters to experiment and other first-principles investigations. In addition, a variety of antiferromagnetic

configurations relating to all spin parallel, anti-parallel pairs were examined. Finally, the band structure of iron arsenide was investigated via two paths through the Brillouin zone, requiring an evaluation of the smearing scheme employed. The external code OPTADOS was utilised to determine the Fermi-level as a verification of the CASTEP determined Fermi-energy due to band occupation concerns.

Further investigations were conducted on the FeSe iron pnictide, which experienced similar results to FeAs. The folded band structure using the PBE and rSCAN functional acted as a good comparison with the experimental ARPES measurements and provided further insights into the magnetic dependency on the complexity of the functional used.

## Chapter 6

In this chapter, conclusions are presented for the previous chapters, including an evaluation of the methods employed.

# Chapter 2

# Theory

## 2.1 Introduction

The wave function is a powerful mathematical and physical construct, which in principle, contains all the information of a quantum mechanical object. Solving the many-body Schrödinger equation provides one with a means of obtaining the wave function . In reality, solving an N-body problem is computationally and analytically exhaustive, making it impossible to use. This impracticality requires the use of approximations to find the ground state solutions. Hohenberg, Kohn and Sham developed these approximations into the modern form of density-functional theory (DFT). DFT relies on one main variational parameter, the electron density which allows for the N-body equation to be re-written as N-one-body equations, simplifying the problem. In this representation, a single electron interacts with all other electrons via an effective exchange-correlation potential. Pseudopotentials and plane-wave basis sets assist in solving the Kohn-Sham equations. *Ad hoc* extensions to the density and Kohn-Sham potential allow for the inclusion of spin and therefore magnetism within the system. The spin-polarisation of a system arises in the exchange-correlation functional.

## 2.2 Ground State Electronic Structure

### 2.2.1 Many-Body Schrödinger Equation

On the quantum level, gravity ceases to have a dominant influence on objects, and as such, the non-relativistic Schrödinger equation describes the interactions, on the proviso that the velocity is significantly smaller than the speed of light. The time-dependent version of the Schrödinger equation is far too unmanageable, due to a large number of dimensions associated with the wave function ($3n_{electron}$ + $3N_{nuclei}$ +1) and the evolution of time. Instead of solving the time-dependent equation directly, the use of stationary states (orbitals) allows for a more straightforward approach. The associated time-independent many-body Schrödinger equation for this approach takes the form;

$$\hat{H}\psi(\mathbf{X}_j, \mathbf{r}_k) = E\psi(\mathbf{X}_j, \mathbf{r}_k) \tag{2.2.1}$$

Where $\hat{H}$ is the Hamiltonian operator, E, the total ground state energy of the system, $\mathbf{X}_j$ are the coordinates of the nuclei and $\mathbf{r}_k$ are the coordinates of the electrons. For a system where only the electrons and nuclei are of interest, the Hamiltonian operator becomes;

$$\hat{H} = \hat{T}_N + \hat{T}_e + \hat{V}_{NN} + \hat{V}_{ee} + \hat{V}_{Ne}$$

$$= \sum_j \left[ -\frac{\hbar^2}{2M_j}\nabla_j^2 + \sum_{l>j} V_I(\mathbf{X}_j - \mathbf{X}_l) \right]$$

$$+ \sum_k \left[ -\frac{\hbar^2}{2m}\nabla_k^2 + \sum_{m>k} \frac{e^2}{|\mathbf{r}_k - \mathbf{r}_m|} + \sum_j U_{e-I}(\mathbf{r}_k - \mathbf{X}_j) \right] \tag{2.2.2}$$

Where $\hat{T}$ is the kinetic energy operator, $\hat{V}$ are the potentials produced by the three interactions; nuclear-nuclear, electron-electron and nuclear-electron. $M_j$ is the mass of the nuclei, and $m$ is the mass of the electron. The quantity $V_I(\mathbf{X}_j - \mathbf{X}_l)$ is the interaction potential between the nuclei,

$U_{e-I}(\mathbf{r}_k - \mathbf{X}_j)$ is the interaction between an electron at $\mathbf{r}_k$ and and a nucleus at $\mathbf{X}_j$.

The Partial differential nature of Equations 2.2.1 and 2.2.2 generate a large number of degrees of freedom, $3n_{electrons} + 3N_{nuclei}$. When Equations 2.2.1 and 2.2.2 are applied to a real system, a numerical solution on a high-performance computer can only happen for six to seven interacting ions or electrons. Therefore, approximations are required for Equations 2.2.1 and 2.2.2 to be useful investigative tools.

### 2.2.2 Born-Oppenheimer Approximation

The discussion proceeds with the separation of the motion of the electrons from the nuclei. That is, the nuclei are in fixed positions and the electrons navigate through them. The nuclei move over longer time-scales, and so the electrons will move into the lowest energy states quicker than the nuclei can react. This observation, therefore, suggests that the electron distribution dictates the potential in which the nuclei move.

The Hamiltonian in 2.2.2 is a summation of the nuclear and electronic contributions to the system,

$$H = H_n + H_e \tag{2.2.3}$$

Where $H_n$ contains the nuclear elements of 2.2.2

$$H_n = \sum_j \left[ -\frac{\hbar^2}{2M_j}\nabla_j^2 + \sum_{l>j} V_I(\mathbf{X}_j - \mathbf{X}_l) \right] \tag{2.2.4}$$

and $H_e$ contains the electronic.

$$H_e = \sum_k \left[ -\frac{\hbar^2}{2m}\nabla_k^2 + \sum_{m>k} \frac{e^2}{|\mathbf{r}_k - \mathbf{r}_m|} + \sum_j U_{e-I}(\mathbf{r}_k - \mathbf{X}_j) \right] \tag{2.2.5}$$

26

Applying the separation to the Hamiltonian, the positions of the nuclei freeze, and the Schrödinger equation is rewritten and solved for travelling electrons only.

$$H_e \psi_{\mathbf{K}}(\mathbf{X}, \mathbf{r}) = E_{\mathbf{K}}(\mathbf{X}) \psi_{\mathbf{K}}(\mathbf{X}, \mathbf{r}) \tag{2.2.6}$$

Use of the single letters $\mathbf{X}$ and $\mathbf{r}$ indicates the set of all nuclear and electronic coordinates, respectively. The wave function of the state and the energy of the system depend upon the nuclear positions, $\sum_j U_{e-I}(\mathbf{r}_k - \mathbf{X}_j)$.

The evaluation of the impact of the nuclear motion onto the electrons is accessible through the acceptance of solving Equation 2.2.6 at each instant of the positions of the nuclei ($\mathbf{X}$). The core electrons will move with the nuclei as they vibrate; however, the influence on the conduction and valance electrons leads to the phenomenon of electron-phonon coupling, which is beyond this treatise. Therefore, outside of the electron-phonon coupling, the Schrödinger equation (Equation 2.2.5) is solved for fixed nuclear positions and then solved using electronic wave functions.

Even with the simplification of the Schrödinger equation to only consider the electronic interactions in a fixed nuclear potential still falls short of being able to handle any complex (real) systems. The dimensionality of the equation is too complex to be solved. The issue resides within the interaction between the pairs of all the electrons (the electron-electron term). The term couples the electrons together inducing a correlation between the electronic states. The current form of the Schrödinger equation is a 1 N-body equation, which still requires further approximation to make it computationally and mathematically manageable.

### 2.2.3 Density-Functional Theory

While the appearance of Equation 2.2.5 is relatively simple, the process to try and solve it is compounding in difficulty. The correlation between electrons makes the equation too complicated for any system more advanced

than the nearly-free electron model. Density-functional theory (DFT) is the description of the approximations involved in the simplification of the complex form of the Schrödinger equation; particularly in the separation of the coupled terms.

### 2.2.3.1   Hohenberg-Kohn Theorems

The first significant advancement in DFT came in the form of the Hohenberg-Kohn theorems [4, 17–19] , which provided the computational skeleton of how to calculate the ground state density and energy. There are two theorems, which state;

1. The total ground state energy of an electronic system is a unique functional of the total density $n(\mathbf{r})$:

$$E[n] = F[n] + \int n(\mathbf{r})v^{\text{ext}}(\mathbf{r})d\mathbf{r} \qquad (2.2.7)$$

where $F[n]$ is also a unique functional of the electron density but is independent of the external potential.

2. For an electronic system, the total energy ($E[n]$) has a minimum equal to the ground state energy at the actual ground state density.

The first theorem describes the nature of the terms in the Hamiltonian: functionals of the electronic density of the system. The second theorem provides means to find the minimum energy by varying the ground state

density. The density which provides the minimum energy must be the actual ground state density.

While the Hohenberg-Kohn theorems provide an excellent foundation for determining the ground state energy and density, they provide no means for rigorous computation.

### 2.2.3.2 The Kohn-Sham Method

A prominent advancement came from the Kohn-Sham equations [20, 21]. The treatment described electrons in a non-interacting, fictitious potential, which produce the same ground state density as the physical system. The interaction within the fictitious system is only through the total density, which corresponds on a one-to-one basis with the ground state energy. Due to this relationship, all the information about the system is contained within this interaction. The creation of the fictitious system allows for a massive simplification of the problem into coupled single-particle equations which only interact through the electron density. To show this, the universal functional (F[n]) of the Equation 2.2.7 must devolve into three parts;

$$F[n] = T[n] + \iint \frac{n(\mathbf{r})n(\mathbf{r}')}{|\mathbf{r} - \mathbf{r}'|} d\mathbf{r} d\mathbf{r}' + E_{xc}[n] \qquad (2.2.8)$$

with the kinetic, Hartree and exchange-correlation energy respectively as the first, second and third term.
The Kohn-Sham method uses the variational principle to form;

$$\frac{\delta E[n]}{\delta n(\mathbf{r})} + \mu \frac{\delta(N - \int n(\mathbf{r})d\mathbf{r})}{\delta n(\mathbf{r})} = 0 \qquad (2.2.9)$$

where $\mu$ is a Lagrange multiplier which deals with the particle conservation. The kinetic energy is now split up and consists of two parts, one term for the energy of the non-interacting electrons ($T_0$) and another term to contain the remainder ($T_{xc}$) , $T = T_0 + T_{xc}$. It is essential to note this separation of the kinetic energy as it allows for the determination of the functional derivative

using the Kohn-Sham orbitals,

$$n(\mathbf{r}) = \sum_{i=1}^{N} |\phi_i(\mathbf{r})|^2 \tag{2.2.10}$$

as well as,

$$T_0[n] = \sum_{i=1}^{N} \int \nabla \phi_i^*(\mathbf{r}) \nabla \phi_i(\mathbf{r}) d\mathbf{r} \tag{2.2.11}$$

where $\phi_i(\mathbf{r})$ represents the single-particle wave functions. For the Equations 2.2.10 and 2.2.11 the summations extend over the lowest N-occupied states.

Through varying Equation 2.2.11 and adding a potential energy term, the Schrödinger equation becomes the Euler-Lagrange equation. The variance form which Equation 2.2.11 takes is;

$$T_0[n] = \sum_{i=1}^{N} \varepsilon_i - \int v'(\mathbf{r}) n(\mathbf{r}) d\mathbf{r} \tag{2.2.12}$$

Achieved from the postulate of the single-particle equation; $(-\nabla^2 + v'(\mathbf{r}))\phi_i(\mathbf{r}) = \varepsilon_i \phi_i(\mathbf{r})$ and premultiplying with $\phi_i^*(\mathbf{r})$, integrating and summing up. The connections in the fictitious system are now of a state where the variation embodied in Equation 2.2.9 is performable. The potential within Equation 2.2.12 becomes the effective potential, experienced by all electrons;

$$v^{\text{eff}}(\mathbf{r}) = v^{\text{ext}}(\mathbf{r}) + 2 \int \frac{n(\mathbf{r}')}{|\mathbf{r} - \mathbf{r}'|} d\mathbf{r}' + v^{\text{xc}}(\mathbf{r}) \tag{2.2.13}$$

where,

$$v^{\text{xc}}(\mathbf{r}) = \frac{\delta(E_{xc} + T_{xc})}{\delta n(\mathbf{r})} \tag{2.2.14}$$

Which makes the single-particle equation become the Kohn-Sham equation;

$$[-\nabla^2 + v^{\text{eff}}(\mathbf{r}) - \varepsilon_i]\phi_i(\mathbf{r}) = 0 \tag{2.2.15}$$

The Kohn-Sham equation is equivalent to the Schrödinger equation with

the modification of the external potential into the effective potential. The effective potential still relies upon the electron density, which in turn depends upon the single-particle states $\phi_i$. Through this, the Kohn-Sham equation is a self-consistent field problem and allows for a redefinition of the total energy.

$$E[n] = \sum_{\substack{i=1, \\ \varepsilon_i \leq E_F}}^{N} \varepsilon_i - \iint \frac{n(\mathbf{r})n(\mathbf{r}')}{|\mathbf{r}-\mathbf{r}'|}d\mathbf{r}d\mathbf{r}' - \int v^{\mathsf{xc}}(\mathbf{r})n(\mathbf{r})d\mathbf{r} + \tilde{E}_{xc}[n] \quad (2.2.16)$$

Whereby the total energy consists of a sum over the eigenvalues, $\varepsilon_i$, with the double counting terms subtracted. The use of $\tilde{E}_{xc}$ permits the inclusion of exchange-correlation kinetic energy, $T_{xc}$.

### 2.2.4 Exchange and Correlation

The Hartree energy of Equation 2.2.15 ($\iint \frac{n(\mathbf{r})n(\mathbf{r}')}{|\mathbf{r}-\mathbf{r}'|}d\mathbf{r}d\mathbf{r}'$) depicts the electrostatic interactions of the system. The representation completely ignores the discrete nature of the electron by allowing them to interact with themselves. The exchange-correlation potential ($v_{xc}$) contains all the differences between the time-independent Schrödinger equation and the the Kohn-Sham equations. In principle, there should be an exact form the exchange-correlation potential takes, providing exact ground state energy and density. However, in practice, it is impossible to achieve.

Correlation and exchange personify the discrete nature of electrons. Firstly, correlation: the primary effect of the Coulomb interaction is to repel like-charges (electrons). Therefore, the assumption of the uniform electron cloud is false; the electrons are point charges, and their actual wave functions will behave in a manner such that the probability of finding two close together will be much less than if their motion was independent. This dependance is correlation; their motion is correlated. Secondly, exchange; true electron wave functions must be entirely anti-symmetric. Two elec-

trons with the same spin cannot occupy the same space. If the interaction between parallel spin electrons are monitored within the charge distribution, as one electron moves and leaves the state then the electrons with the opposite spin fill this hole. The exchange effect exactly cancels out the density of electrons of parallel spin at the now filled position. The total integrated exchange charge is just that of a single electron. Thus, the electrons experience an exchange energy from the anti-symmetric nature of the wave functions.

### 2.2.4.1  Exchange-Correlation Functionals

Due to the computationally exhaustive process required to find the exact form of the XC potential (the same as solving the many-body Schrödinger time-independent equation), approximations are required. The local density approximation (LDA) [20] operates under the scheme of a homogeneous, interacting electron gas: modelling the exchange-correlation energy as;

$$E_{xc}^{\mathsf{LDA}}[n] = \int n(\mathbf{r})\varepsilon_{xc}(n(\mathbf{r}))d\mathbf{r} \qquad (2.2.17)$$

whereby $T_{xc}$ is included in $E_{xc}[n]$. $\varepsilon_{xc}(n)$ is not the eigenenergy but a function of the density instead of a functional. Equation 2.2.17 divides the inhomogeneous electron system into small 'boxes', each containing a homogeneous interacting electron gas with a density $n(\mathbf{r})$, suitable for the 'box' at $\mathbf{r}$. Therefore providing the locality aspect of the approximation. Requiring a slow varying density, the LDA can only predict isotropic interactions. In a system where the density varies quickly, LDA would not be valid. The energy of the approximation depends on spherical averages, which provides excellent results for many materials.

Increasing in the complexity of XC functionals, while maintaining locality is the generalised gradient approximation (GGA). This semi-local functional uses some information about the gradient of the density at r. Introducing

the gradient of the density into E requires consideration of the shape it takes. There are many different forms; one popular choice is developed by Perdew, Burke and Ernzerhof (PBE) [22].

$$E_{xc}^{\mathsf{GGA}}[n] = \int n(\mathbf{r})\varepsilon_{xc}(n(\mathbf{r}), \nabla n(\mathbf{r}))d\mathbf{r} \qquad (2.2.18)$$

PBE is computationally simpler than other GGAs while maintaining important physical features: not relying on tuning parameters but the fundamental limits of the exact XC functional.

An extension to the GGA's can be made by including the Kohn-Sham orbital kinetic energy densities. The meta-GGA's are still semi-local but contain implicit nonlocal functions ($n(\mathbf{r})$) [23–26]. The semi-local approximation of the meta-GGAs can be expressed as:

$$E_{xc}^{\mathsf{meta\text{-}GGA}}[n] = \int n\varepsilon_{xc}(n(\mathbf{r}), \nabla n(\mathbf{r}), \tau)d^3\mathbf{r} \qquad (2.2.19)$$

where,

$$\tau = \sum_i^{\mathsf{occ}} \frac{1}{2}|\nabla\psi_i|^2$$

which represents the positive orbital kinetic energy densities. Strongly Constrained and Appropriately Normed (SCAN) [27] and subsequently Regularised Strongly Constrained and Appropriately Normed (rSCAN) [28] have made major improvements as the first meta-GGA which satisfies all known possible exact constraints [27]. The exact constraints and norms are listed in full in Sun *et al.* [27] and so will only be briefly explained here. The purpose of using constraints is to allow the XC functional to adhere to physical constraints which exact DFT possesses and therefore are necessarily true for all systems of electrons. The appropriately normed aspect of SCAN relates to modelling a *"system for which semi-local functional can be exact or extremely accurate"* [27]. These were taken to be the exchange and correlation energies of four rare gas atoms (Ne, Ar, Kr and Xe), the exchange and correlation surface energies of four jellium slabs and the interaction

energy of $Ar_2$ at repulsive atomic distances. The SCAN functional, however, suffered from numerical instabilities in the construction of the pseudopotential and the solution to atomic all-electron generalised Kohn-Sham equation. In order to improve this, rSCAN regularised the SCAN XC functional which controlled the numerical challenges while remaining as close to the original SCAN functional as possible. The modifications of rSCAN exist in the isoorbital indicator, which connects different approximations of the exchange correlation energy. The changes eliminates the unphysical divergence of the exchange correlation potential.

### 2.2.5 Pseudopotentials

The valence wave functions oscillate quickly inside the core-region due to the strong ionic potential; these sustain the orthogonality between the core and valance electrons. The pseudopotential must be generated such that no nodes are present within the core-region of the pseudo-wave function as well as the pseudopotentials and pseudo-wave functions becoming identical to the all-electron wave function outside a cut-off radius ($r_c$), see Figure 2.1. When these conditions are not met, non-physical states can be introduced into the calculations; often referred to as ghost states. Multiple methods exist to generate pseudopotentials, which are beyond this treatise. Pseudopotentials speed up calculations due to the reduction in computational complexity as they decrease the number of electronic states that must be calculated.

Within this thesis, the ultrasoft pseudopotentials were used instead of norm-conserving pseudopotentials as they allow for lower plane wave cut off. This reduces the number of plane waves within the calculation and reduces the computational demand of the calculations.
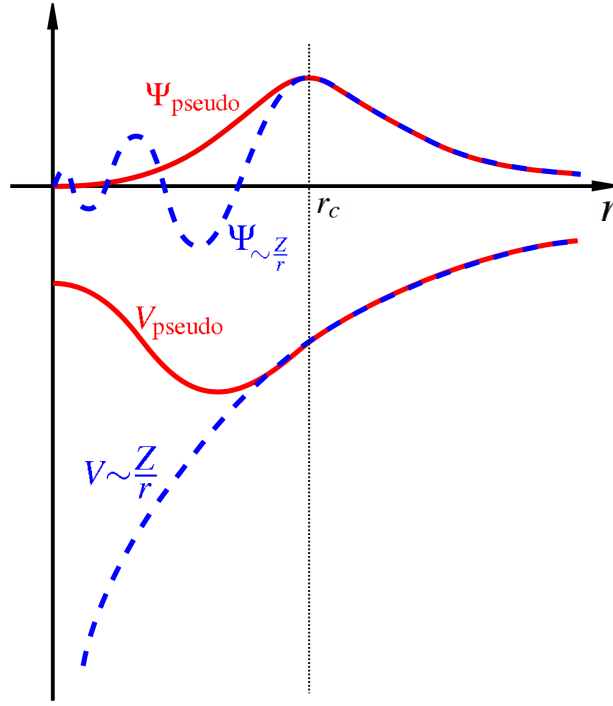
Figure 2.1: Comparison between the pseudo-wave function and pseudopotential (red) with a coulomb potential representing the all-electron wave function and potential (Blue). Source of image from Wolfram Quester.

## 2.3 Ground State Electronic Structure Calculations

The previous sections have outlined the framework for DFT calculations, but the practical element of conducting calculations requires consideration.

### 2.3.1 Arriving at the Ground State

The main objective of every DFT code is to find the ground state of the material. Every physical property of a material can be determined from the ground state total energy and density. These calculations must be efficient and conducted within a limited amount of memory, and with moderate use of the CPU time.

### 2.3.1.1    The Ground State Density and Total Energy

For the total energy in DFT to be a valid representation, it must be self-consistent. The approach to generate a quantity must return that quantity when it is used as an input. Within DFT, the most fundamental example is the electronic density generated by the occupied Kohn-Sham orbitals, which depend upon the Kohn-Sham potential, generated from the electronic density.

The process of self-consistency begins with a trial wave functions, $\psi_{i,k}$, which in turn generates a trial density, $n(\mathbf{r})$. Calculating the Kohn-Sham potential, $v_{ks}$, and starting energy, $E$, use this trial density. From here the total energy is minimised with respect to the wave functions in the Kohn-Sham potential, producing a new set of wave functions, $\psi_{i,k}$. These new wave functions generate new total energy, $E$, and ground state density, $n(\mathbf{r})$. The new total energy is compared with the previous iterations, and the difference is checked with a user-defined tolerance; if the energy has not fluctuated more than the specified tolerance, it has converged. This process assumes that the final energy must be the minimum, and therefore the ground state based upon little variance between iterations; this can often not be the case but instead produce a local minimum. For a visual representation of this process, see Figure 2.2.
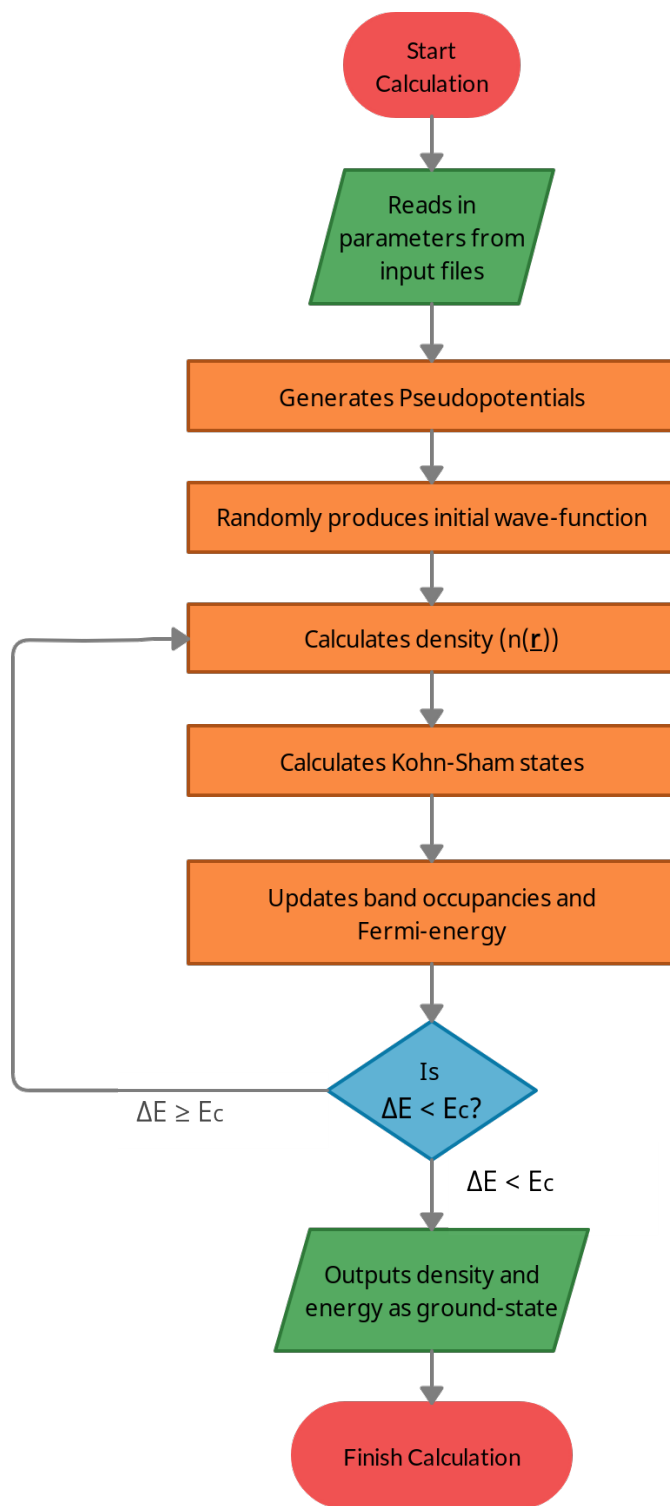
Figure 2.2: Flow-chart showing the process used by CASTEP [16] to calculate the ground state density and total energy.

## 2.3.2 The Basis Sets

At the forefront of any useable DFT code is the concept of efficiency through computational effort and memory consumption. The electronic states fall under this scrutiny by using a truncated Fourier expansion to represent them, $N_g$.

$$\psi_{i,\mathbf{k}}(r) = \sum_{G=0}^{N_k} c_{i,k,G} e^{i(k+G)\cdot r} \tag{2.3.1}$$

Following this scrutiny, the Hamiltonian operator is rewritten into a mixture of operators from the normal space and Fourier space coefficients. Thus, the kinetic energy can be represented as an uncomplicated diagonal form in Fourier space.

$$T[\psi_{i,\mathbf{k}}(r)] = \sum_{\mathbf{G}=0}^{N_k} c_{i,\mathbf{k},\mathbf{G}} \frac{|\mathbf{k}+\mathbf{G}|^2}{2} \tag{2.3.2}$$

Defining a limit to the Fourier series is essential in maintaining a low memory consumption. Kinetic energy offers a natural way to this solution by only considering basis states below a specific kinetic energy. Thus, the limit to the Fourier series becomes; $|\mathbf{k}+\mathbf{G}_{max}|^2 \leq E_{cut}$.

The XC potentials are diagonal in real space as they only depend on r due to their local nature. The operators are employed in real space by transforming the density into real space, and then the density is transformed back to reciprocal space. While this process sounds lengthy, it is efficiently performed through fast Fourier transforms (FFTs) owing to the basis set to be a multiple of small prime numbers.

### 2.3.2.1 The Wave Functions

The solutions to the single-particle Kohn-Sham Equations are the Kohn-Sham wave functions, shown in Equation 2.2.15. Upon writing Equation

2.2.15 in a matrix form, the problem becomes an eigenvector problem and can be solved via matrix diagonalisation with the limitation of potential energy degeneracies, represented as eigenvalues. The computational cost to diagonalise is $n_{pw}^3$, with the number of basis set elements depicted as $n_{pw}$. If this process were used, it would cause severe bottlenecks in plane-wave basis set codes as the number of $n_{pw} \gtrsim 100,000$.

The Hamiltonian as a matrix has a size of $n_{pw}^2$, making direct diagonalisation provides $n_{pw}$ wave functionswhich are so big that the order of magnitude is larger than the number of occupied states. This computational ordeal forces codes to use an iterative technique to minimise the energy of the wave functionsthrough the Kohn-Sham Hamiltonian [29]. This minimisation produces an arbitrary number of lowest energy wave functionsto be found.

### 2.3.2.2  Discretisation of Real Space through Grids

The discretisation of real space is possible through the Nyquist-Shannon theorem [30], which allows the utilisation of the finite Fourier series, holding the wave functions, to be represented by a discrete set of points in real space. Moreover, this discrete set of points can fully embody all the information stored within the Fourier series. Allowing the Fourier space to be represented by a grid of $N_x, N_y, N_z$ components, the real space grid will have a size of $N_x \times N_y \times N_z$. The Fourier expansion within the FFTs converts between the two grids, using a divide-and-conquer algorithm, such as that constructed by Cooley-Tukey [31].

The density and higher-order Fourier components, which is a product of the wave functions, are produced up to twice those in the wave function due to the convolution theorem. This size requires a more significant basis set and a finer grid in real space to represent it accurately. However, this fine detail usually has little effect on the density and, subsequently, total energy, acting as another mechanism to limit the size of the Fourier se-

ries. Within CASTEP [16], a user-defined flag, the grid-scale is the ratio for product terms within the Fourier series. For instance, the density of the wave functions, therefore using a fine grid-scale, is essential for ensuring the accuracy of calculations.

### 2.3.2.3 Sampling the Reciprocal Space

Within the density are electronic states, which need to be modelled accurately through sampling at a set number of points. The location of these points must be within the first Brillouin zone to correctly solve for the wave function of the infinite crystal. The sampling is performed through the use of an evenly spaced 3-dimensional grid called the Monkhorst-Pack (MP) grid [32]. This set is unbiased due to its equidistant points and is beneficial as an $n \times n \times n$ grid encapsulates interactions with up to the nearest $n^{th}$ neighbour unit cells. The importance of using a dense enough MP grid is imperative to reliable DFT calculations; use too coarse a grid, and the electronic states will not be well represented, leading to inaccuracies.

## 2.3.3 Electronic Band Structure

This section will focus on how CASTEP [16] determines the Fermi-level and the importance of k-point sampling for the higher-order Fourier components: bands crossing the Fermi-level.

### 2.3.3.1 Establishing the Fermi-Level

Fundamentally, statistical mechanics defines the Fermi-level as the highest occupied state any electron can occupy at T=0K. Thus, populating from the lowest energy states until the total number of electrons are placed relates to the Fermi-level. The last electron placed marks the highest occupied state and signifies the Fermi-level, as made clear from the Fermi-Dirac

distribution function at T=0K, Equation 2.3.3.

$$f_{i,\mathbf{k}} = (\exp(\frac{\varepsilon_{i,\mathbf{k}} - \mu}{k_B T}) + 1)^{-1} \tag{2.3.3}$$

In practice, an iterative process, beginning with a trial Fermi-energy, uses the relationship expressed in Equation 2.3.3 to converge to a Fermi-energy within a user-defined tolerance. This process relies on the sum of occupied states equalling the total number of electrons and the discretisation of reciprocal space. Hence, once again, the importance of using a k-point mesh that is both computationally economical and dense enough so that it can accurately represent the wave functionsresurfaces. If the sampling is too coarse, then the wave functionsare not accurately represented, which will affect the density and, therefore, the occupancy of the states; see Equation 2.3.4. Which, in turn, will lead to significant errors in the Fermi-energy.

$$n(\mathbf{r}) = \sum_i \int_{BZ} f_{i,\mathbf{k}} |\psi_{i,\mathbf{k}}(\mathbf{r})|^2 d\mathbf{k} \tag{2.3.4}$$

Where, the index $i$ represents the states and $f_i$ are the occupation numbers.

### 2.3.3.2 Smearing Schemes

The integration over the Brillouin zone in Equation 2.3.4 is conducted by summing over a finite set of k-points. For metallic systems, where partially occupied bands cross the Fermi-level, discontinuities arise from the occupation suddenly going from 1 to 0. For these instances, only a computationally exhaustive set of k-points would provide convergence. Supplanting the integer occupation numbers, $f_{i,\mathbf{k}}$, with a function that varies smoothly from 1 to 0 close to the Fermi-level alleviates this issue. Such a function is the Fermi-Dirac distribution, Equation 2.3.3.

An advantage of using the Fermi-Dirac smearing scheme is that the electronic smearing corresponds to a physical, thermal distribution at the user-defined temperature T. The disadvantage to the Fermi-Dirac smearing is that the function tails off very slowly, so to capture all of the occupied states, many slightly occupied conductions bands are needed.

The Gaussian smearing function [33], see Equation 2.3.5, fixes the long tails issues with a shifted and scaled error function for the state occupancy. Thus, in Gaussian smearing, the number of partially occupied conduction states required are significantly lower.

$$f(\varepsilon) = \frac{1}{2}\Big(1 - \text{erf}(\frac{\varepsilon - \mu}{\sigma})\Big) \tag{2.3.5}$$

Where $\sigma = k_B T$ and represents the broadening, $\mu$ is the chemical potential and $\text{erf}(x)$ is the standard error function.

The failings of Gaussian smearing are the unphysical nature of the smearing width and the contribution to the free energy caused by the broadening, forcing the total energy and forces significantly higher than the actual value, at T=0K. The total energy can be extrapolated back to T=0K *post hoc* calculation; however, the forces and stresses cannot.

Another method commonly used is the cold smearing [34] approach which incorporates and fixes the long tail issue while simultaneously not yielding unrealistic negative occupancies such as the Methfessel-Paxon smearing [35] creates. The cold smearing distribution takes the form:

$$f(x_i) = \frac{1}{2}\left[\sqrt{\frac{2}{\pi}}\text{exp}(-x_i^2 - \sqrt{2}x_i - \frac{1}{2}) + 1 - \text{erf}\left(x_i + \frac{1}{\sqrt{2}}\right)\right] \tag{2.3.6}$$

where $x_i = \frac{\varepsilon_i - \mu}{\sigma}$. A similarity with the Methfessel-Paxon scheme is the elimination of lower than second-order contributions to the free energy from the broadening. Therefore, the total energy and forces are very close to the absolute, zero temperature, values; including substantial values of the

broadening parameter.

## 2.4 Spin-Dependant Ground State Electronic Structure

### 2.4.1 Dirac Theory

In the previous sections, the spin of the electron is mostly ignored, except when invoking the Pauli-exclusion principle. It is readily apparent that spin, as an observable, is of paramount importance in accurately describing magnetic materials [4, 36–43]. The Dirac equation is the fully relativistic formulation of the Kohn-Sham equations;

$$H_D \psi_i = \varepsilon_i \psi_i \tag{2.4.1}$$

Where $\psi_i$ is a four-component single-particle wave function and $H_D$ is the Dirac single-particle Hamiltonian;

$$H_D = c\boldsymbol{\alpha} \cdot \mathbf{p} + \beta m c^2 + V \tag{2.4.2}$$

The quantity $\boldsymbol{\alpha}$ is a vector operator with the Pauli spin matrices, $\sigma_k$, as the components;

$$\alpha_k = \begin{pmatrix} 0 & \sigma_k \\ \sigma_k & 0 \end{pmatrix} \tag{2.4.3}$$

With the standard representation of;

$$\sigma_1 = \begin{pmatrix} 0 & 1 \\ 1 & 0 \end{pmatrix}, \sigma_2 = \begin{pmatrix} 0 & -i \\ i & 0 \end{pmatrix}, \sigma_3 = \begin{pmatrix} 1 & 0 \\ 0 & -1 \end{pmatrix} \tag{2.4.4}$$

Which represent the $x,y$ and $z$ Pauli spin matrices, respectively. The quantity $\mathbf{p}$ in Equation 2.4.2 is the momentum operator, which takes the form of

$\mathbf{p} = -i\hbar\nabla.\beta$ is a matrix of the form;

$$\beta = \begin{pmatrix} \mathbf{1} & 0 \\ 0 & -\mathbf{1} \end{pmatrix} \tag{2.4.5}$$

With

$$\mathbf{1} = \begin{pmatrix} 1 & 0 \\ 0 & 1 \end{pmatrix} \tag{2.4.6}$$

The last term in Equation 2.4.2, V, represents an effective potential which we associated with the form of $v_{\text{eff}}$ from Equation 2.2.13.

There are two main properties from the Dirac theory of the electron which are relevant for magnetism. The first is a quantum mechanical derivation of magnetisation which connects the electron spin with Maxwell's equations and is referred to as Gordon's decomposition of the current; which is not examined here. The second is the classification of spin-orbit coupling, which directly leads to magneto-crystalline anisotropy.

### 2.4.2  Spin-Orbit Coupling

The spin-orbit interaction is a relativistic interaction which connects the particles spin and its motion inside a potential. Due to the relativistic nature of this interaction, the Dirac Hamiltonian is used along-side radial components and spherical harmonics. The spin-orbit correction takes the form;

$$H_D\tilde{\psi} = \varepsilon'\tilde{\psi} + H_{SO}\tilde{\psi} \tag{2.4.7}$$

where

$$H_{SO} = \frac{\hbar}{(2Mc)^2}\frac{1}{r}\frac{dV}{dr}\begin{pmatrix} (\boldsymbol{\sigma}\cdot\mathbf{L})\mathbf{1} \\ 0 \end{pmatrix} \tag{2.4.8}$$

$\tilde{\psi}$ is the four-component wave function ;

$$\tilde{\psi} = \begin{pmatrix} \tilde{\phi} \\ \tilde{\chi} \end{pmatrix} \qquad (2.4.9)$$

where

$$\tilde{\phi} = \tilde{g} Y_L \chi_S \qquad (2.4.10)$$

$Y_L$ is the spherical harmonic of order $L = (\ell, m)$ and $\chi_+ = \begin{pmatrix} 1 \\ 0 \end{pmatrix}$ and $\chi_- = \begin{pmatrix} 0 \\ 1 \end{pmatrix}$. $\tilde{\chi}$ takes the form of;

$$\tilde{\chi} = i \left( \frac{\boldsymbol{\sigma} \cdot \mathbf{x}}{r} \right) \left( -\tilde{f} + \frac{1}{2Mcr} \tilde{g} \boldsymbol{\sigma} \cdot \mathbf{L} \right) Y_{L-\chi s} \qquad (2.4.11)$$

and the approximate radial functions $\tilde{g}$ and $\tilde{f}$ are;

$$\varepsilon' \tilde{g} = -\frac{\hbar^2}{2M} \frac{1}{r^2} \frac{d}{dr} \left( r^2 \frac{d\tilde{g}}{dr} \right) + \left[ V + \frac{\hbar^2}{2M} \frac{\ell(\ell+1)}{r^2} \right] \tilde{g} - \frac{\hbar^2}{4M^2c^2} \frac{dV}{dr} \frac{d\tilde{g}}{dr} \quad (2.4.12)$$

$$\tilde{f} = \frac{\hbar}{2Mc} \frac{d\tilde{g}}{dr} \qquad (2.4.13)$$

with the proper normalisation of;

$$\int (\tilde{g}^2 + \tilde{f}^2) r^2 dr = 1 \qquad (2.4.14)$$

The form Equation 2.4.8 takes is the spin-orbit coupling operator which enables a determination for how much the function $\tilde{\psi}$ fails to be an exact solution of the spherical potential Dirac equation. In most cases, the matrix element of $H_{SO}$ is computed and then added to the Hamiltonian matrix in a variational model. This process breaks degeneracy of the spin-degenerate bands. The spin-orbit treatment is dependant upon the basis used, and different treatments are required for each basis, for instance, Linear Augmented Plane Waves (LAPW) and Relativistic Augmented Plane Waves

(RAPW).

## 2.4.3 Spin-Density-Functional Theory

The spin-density-functional theory operates from the work of von Barth and Hedin [44] and Rajagopal and Callaway [45], who were the first to orchestrate the use of matrix formalism to represent the density and external variables instead of single variables. This formalism allows for better computational performances and eases the mathematics associated with it. The most straightforward inclusion of magnetic materials in DFT is to attach two spinors ( $\chi_+$ and $\chi_-$) to the wave function . These two-component spinors require a Hamiltonian of the size of a 2 $\times$ 2 matrix. This Hamiltonian has three parts; the kinetic energy, the external potential and the Coulomb interaction of the electrons. The operators take the following, respective, form:

$$T_{\alpha\beta} = -\delta_{\alpha\beta} \sum_{i=1}^{N} \nabla_i^2 \tag{2.4.15}$$

$$V_{\alpha\beta} = \sum_{i=1}^{N} v_{\alpha\beta}^{\text{ext}}(\mathbf{r}_i) \tag{2.4.16}$$

$$U_{\alpha\beta} = \sum_{\substack{i=1,j=1 \\ i \neq j}} \frac{\delta_{\alpha\beta}}{|\mathbf{r}_i - \mathbf{r}_j|} \tag{2.4.17}$$

Where $\alpha$ and $\beta$ are the spin indices for up and down, respectively. The formulation of these interactions comes from the spinor function Hamiltonian. The electron-density operator and the determination of the electron density (Equations 2.4.18 and 2.4.19) remain unchanged from non-spin inclusive DFT. However, in this formalism, the spinor function provides the many-body state.

$$\hat{n}(\mathbf{r}) = \sum_{i=1}^{N} \delta(\mathbf{r} - \mathbf{r}_i) \tag{2.4.18}$$

$$n(\mathbf{r}) = \langle \Phi | \hat{n}(\mathbf{r}) | \Phi \rangle \tag{2.4.19}$$

where $|\Phi\rangle$ is a many-body state.

Determination of the total energy of the magnetic system begins by re-defining Equation 2.2.7 in the Hohenberg-Kohn theorem with the functionals depending on the spin-density matrix, $\tilde{n}(\mathbf{r})$; with elements $n_{\beta\alpha}(\mathbf{r})(\beta = 1, 2$ and $\alpha = 1, 2)$ defined by:

$$n_{\beta\alpha}(\mathbf{r}) = N \sum_{\sigma_2, \cdots, \sigma_N} \int \rho(\mathbf{r}\beta, \mathbf{r}_2\sigma_2, \cdots, \mathbf{r}_N\sigma_N | \mathbf{r}\alpha, \mathbf{r}_2\sigma_2, \cdots, \mathbf{r}_N\sigma_N) d\mathbf{r}_2, \cdots, d\mathbf{r}_N \tag{2.4.20}$$

and

$$E[\tilde{n}] = F[\tilde{n}] + V[\tilde{n}] \tag{2.4.21}$$

with

$$F[\tilde{n}] = T[\tilde{n}] + \iint \frac{n(\mathbf{r})n(\mathbf{r}')}{|\mathbf{r} - \mathbf{r}'|} d\mathbf{r}d\mathbf{r}' + E_{xc}[\tilde{n}] \tag{2.4.22}$$

$$V[\tilde{n}] = \inf_{\rho \in M(\tilde{n})} \text{Tr}\langle \rho V \rangle = \inf_{\rho \in M(\tilde{n})} \sum_{\alpha\beta} \int v_{\alpha\beta}^{\text{ext}}(\mathbf{r})n_{\beta\alpha}(\mathbf{r})d\mathbf{r} \tag{2.4.23}$$

As with non-spin inclusive DFT, the spin-DFT methods are the same with care taken to include the effects of spin. The density matrix elements can be simplified, upon the assumption that there exists single-particle functions, $\phi_{i\alpha}(\mathbf{r})$, that allow the elements to become;

$$n_{\beta\alpha}(\mathbf{r}) = \sum_{\substack{i=1 \\ \varepsilon_{i\alpha}\varepsilon_{i\beta} \leq E_F}}^{N} \phi_{i\beta}(\mathbf{r})\phi_{i\alpha}^*(\mathbf{r}) \tag{2.4.24}$$

where the indices $\alpha$ and $\beta$ are $\alpha = 1, 2$ and $\beta = 1, 2$ due to the electron spin.

The kinetic energy splits into the kinetic energy of non-interacting particles,

$T_0[\tilde{n}]$, and the remainder, $T_{xc}[\tilde{n}]$.

$$T_0[\tilde{n}] = \sum_{\alpha=1}^{2} \sum_{\substack{i=1 \\ \varepsilon_{i\alpha} \leq E_F}}^{N} \int \nabla\phi_{i\alpha}^*(\mathbf{r})\nabla\phi_{i\alpha}(\mathbf{r})d\mathbf{r} \qquad (2.4.25)$$

The appearance of the Fermi energy follows from the density, as only eigenvalues below the Fermi energy are required as this is not the finite-temperature extension to DFT.

$$n(\mathbf{r}) = \sum_{\alpha=1}^{2} \sum_{\substack{i=1 \\ \varepsilon_{i\alpha} \leq E_F}}^{N} |\phi_{i\alpha}(\mathbf{r})|^2 \qquad (2.4.26)$$

The ansatz finishes with the postulation of the spin-Kohn-Sham equation.

$$\sum_{\beta} \left( -\delta_{\alpha\beta}\boldsymbol{\nabla}^2 + v'_{\alpha\beta}(\mathbf{r}) - \varepsilon_i\delta_{\alpha\beta} \right)\phi_{i\beta}(\mathbf{r}) = 0 \qquad (2.4.27)$$

Minimisation of the total energy occurs in an attempt to determine the potential matrix. The spin-Kohn-Sham equation allows for the kinetic energy to be written as;

$$T_0[\tilde{n}] = \sum_{i=1}^{N} \varepsilon_i - \sum_{\alpha\beta} \int v'_\alpha\beta(\mathbf{r})n_\beta(\mathbf{r})d\mathbf{r} \qquad (2.4.28)$$

This form of the kinetic energy can be substituted into Equation 2.4.22, allowing for the variational energy to be easily determined. Equation 2.4.29 provides means for determining the effective potential matrix Equation 2.4.30.

$$\frac{\delta E[\tilde{n}]}{\delta\tilde{n}_{\alpha\beta}(\mathbf{r})} = 0 \qquad (2.4.29)$$

$$v'_{\alpha\beta}(\mathbf{r}) \equiv v^{\text{eff}}_{\alpha\beta}(\mathbf{r}) = v^{\text{ext}}_{\alpha\beta}(\mathbf{r}) + 2\delta_{\alpha\beta} \int \frac{n(\mathbf{r}')}{|\mathbf{r}-\mathbf{r}'|}d\mathbf{r}' + v^{\text{xc}}_{\alpha\beta}(\mathbf{r}) \qquad (2.4.30)$$

where

$$v^{\text{xc}}_{\alpha\beta}(\mathbf{r}) = \frac{\delta}{\delta\tilde{n}_{\beta\alpha}(\mathbf{r})}\left( E_{xc}[\tilde{n}] + T_{xc}[\tilde{n}] \right) \qquad (2.4.31)$$

Equations 2.4.27, 2.4.30 and 2.4.31 form the Kohn-Sham equations which are coupled together. The total energy can be reformed in a similar arrangement to Equation 2.2.16;

$$E[\tilde{n}] = \sum_{\substack{i=1, \\ \varepsilon_i \leq E_F}}^{N} \varepsilon_i - \iint \frac{n(\mathbf{r})n(\mathbf{r}')}{|\mathbf{r} - \mathbf{r}'|} d\mathbf{r} d\mathbf{r}' - \sum_{\alpha\beta} \int v_{\alpha\beta}^{\text{xc}}(\mathbf{r})n_{\alpha\beta}(\mathbf{r})d\mathbf{r} + E_{xc}[\tilde{n}] \quad (2.4.32)$$

Most notability, the difference is the inclusion of differentiating between spin-up and spin-down electrons.

### 2.4.3.1 Spin-Exchange-Correlation Functionals

The LDA adaption for spin-polarised systems, LSDA, differs as the exchange-correlation energy functional is written in terms of a uniform spin-density, $n_\uparrow$, $n_\downarrow$.

$$E_{xc}^{LSDA}[n_\uparrow, n_\downarrow] = \int n(\mathbf{r})\varepsilon_{xc}(n_\uparrow(\mathbf{r}), n_\downarrow(\mathbf{r}))d\mathbf{r} \quad (2.4.33)$$

The validity of the LDA exists only in a slowly varying density; the same is true for LSDA with a slowly varying spin-density. This condition does not seem appropriate for real atoms, molecules and solids; which have the ability for excitations. While LSDA may seem inappropriate, an electron gas exists in which $n_\uparrow$ and $n_\downarrow$ are constant and for which LSDA is exact. Despite the simplicity of LSDA, there are many real systems in which it accurately describes the magnetic information.

The semi-local functionals of the GGAs are also adaptable to representing magnetism within the system. Operating in a similar model to the non-magnetic case the magnetic-GGAs take, in some essence, the following form;

$$E_{xc}^{GGA}[n_\uparrow, n_\downarrow] = \int \varepsilon_{xc}(n_\uparrow, n_\downarrow, \boldsymbol{\nabla}n_\uparrow, \boldsymbol{\nabla}n_\downarrow)d\mathbf{r} \quad (2.4.34)$$

While the input quantity ($\varepsilon_{xc}(n_\uparrow, n_\downarrow)$) to LSDA is, in principle, unique. There is no such unique input quantity ($\varepsilon_{xc}(n_\uparrow, n_\downarrow, \boldsymbol{\nabla}n_\uparrow, \boldsymbol{\nabla}n_\downarrow)$) for the GGAs.

Instead the GGAs adhere to a rigorous 'conservative philosophy of approximations' which allows for the construct of nearly-unique GGAs possessing all the known correct formal feature of LSDA [22].

The meta-GGAs are also capable of the *ad-hoc* adaptation to spin, with the exchange correlation functional taking the shape:

$$E_{xc}^{\text{meta-GGA}}[n_\uparrow, n_\downarrow] = \int \varepsilon_{xc}(n_\uparrow, n_\downarrow, \boldsymbol{\nabla} n_\uparrow, \boldsymbol{\nabla} n_\downarrow, \tau_\uparrow, \tau_\downarrow) d^3 r \qquad (2.4.35)$$

with the orbital kinetic energy as:

$$\tau_\sigma = \sum_i^{\text{occ}} \frac{1}{2} |\nabla \psi_{i,\sigma}|^2$$

Where $\sigma =\uparrow$ or $\downarrow$ for majority and minority spin channels respectively.

## 2.5   Complex Magnetism

### 2.5.1   Co-linear and Non-Co-linear Magnetism

A co-linear magnet has the property of all the magnetic ions aligning along a common quantisation axis; for mathematical convenience, it is the z-axis. Ferromagnet's magnetic moments ($M_i$ = M) have the same moment value on all of the magnetic sites in the system, with their positions denoted at $\mathbf{R}_i$. An antiferromagnet possesses a staggered arrangement of magnetic moments ($M_i = \pm$M) of the same size, but of opposing direction to its neighbours. In materials, the magnetic structure can take the form of more complex antiferromagnetic configurations; for instance, the up-up-down-down state. Ferrimagnetic arrangement occurs when the magnitude of the magnetic moments differ from one site to the next. The direction of the moments in the Ferrimagnetic state still obey the basis of antiferromagnetism but form sub-lattices. The most excellent examples of ferromag-

nets and antiferromagnets are the 3d transition metals: hcp-Co, fcc-Ni and bcc-Fe have ferromagnetic ground-states while bcc-Cr and fcc-Mn can be antiferromagnetic.

In non-co-linear magnetic structures, the quantisation axis ($\hat{e}_M$) is not the same for all of the magnetic ions. The axis can change direction from one site to the next. The most typical non-co-linear magnetic structure is an incommensurate (where the magnetic periodicity exceeds the structural) spiral spin-density wave. These magnetic structures often occur in systems with a topologically frustrated antiferromagnetic interaction, for instance antiferromagnetically interacting ions in a triangular lattice. Another common cause for this magnetic structure is in systems with competing exchange interactions between neighbours, such as in the case of fcc-Fe.

For the bcc-Cr and fcc-Mn cases, the magnetic states can take on a more complex, non-co-linear form. Cr exhibits a frozen sinusoidal spin-density wave. The magnetism, of which, is characterised by a magnetisation which varies in space like a wave: integrating over space, leads to vanishing total magnetism.

$$\mathbf{m}(\mathbf{r}) = \mathbf{M}\cos(\mathbf{q}\mathbf{r})$$

$$\int_{\infty} \mathbf{m}(\mathbf{r})d\mathbf{r} = 0 \tag{2.5.1}$$

where q is the phase factor or Q-vector of the magnetic spiral, which experimentally is $q \approx 0.952\frac{2\pi}{a}$ for Cr.

## 2.5.2 Exchange Interactions

Ions in a system with magnetic moments, within a reasonable range, interact with each other via exchange interactions. An exchange interaction parameter, J, characterises the strength and type of this magnetic interac-

tion (antiferromagnetic or ferromagnetic). Exchange mechanisms pose an insight into the dynamics of those interactions. There are three primary types of exchange mechanism. Magnetic insulators typically have short-range order, and so the third mechanism (metallic exchange) is no suitable explanation for the observed behaviour.

1. Direct or Potential Exchange:

    This exchange aims to minimise the potential energy by reducing the electronic wave function overlap. The reduction in the overlap is achieved by the addition of nodes to the wave function. These nodes can occur upon the production of anti-symmetric spatial wave functions. These wave functions favour symmetric spin arrangement and thus generate ferromagnetic interactions.

    In the instance where the wave functions are localised on different ions, the minimisation of the potential between the ions leads to symmetric spatial wave functions; favouring anti-symmetric spins, generating antiferromagnetic interactions.

2. Kinetic or Super-Exchange:

    Super-exchange, fundamentally, describes the interaction of electrons hopping via an intermediate ion. It originates from the case in transition metals where the magnetic ions are so far apart that direct overlap of the wave functions is not possible. However, despite this distance, there is still a robust kinetic exchange. This exchange operates through minimising the kinetic energy by reducing the gradients of the wave functions through delocalisation of the electrons. In an insulating system, the electrons are localised, and so the kinetic exchange interaction arises from a perturbation of a virtual electron transfer, generating an antiferromagnetic interaction. Double exchange is a form of kinetic exchange in which a real electron is exchanged between ions of different species and with different oxidation states. This kinetic mechanism allows for ferromagnetic or

antiferromagnetic interactions. For instance, the Mn-O-Mn bond with an angle of $180^0$; the Mn $e_g$ orbitals are directly interacting with the 2p orbitals from the oxygen. One of the Mn ions has more electrons than the other. A transfer of one spin-up electron from the oxygen to the $Mn^{4+}$ occurs, and the oxygen's empty orbital is filled by the $Mn^{3+}$ ion. Electrons have then travelled between the metal ion preserving the spin, due to Hund's rules.

3. Metallic-Exchange:

Magnetism is typically introduced in materials through the 3d transition-metals or the lanthanides. In metallic systems, itinerant electrons are responsible for probing the lattice and forming the Fermi-Surface. The hopping of the electrons across the lattice means that the type of exchange interaction is long-range. In assisting in the formation of the Fermi-Surface, the magnetism is interwoven with the electronic structure of the system. The hopping of the electrons in transition metals are correlated, meaning that the electron hopping in/out of an atomic site possess the same spin orientation. Increasing the time-scale of observation to a value significantly larger than the time it takes for the electrons to hop (around femtoseconds), a quasi-static local magnetic moment can be observed at the site.

In the instance of a 4f-system, the exchange interaction between the 4f localised moments is interfered by the 5d and 6s itinerant electrons and takes the form of the Ruderman-Kittel-Kasuya-Yoshida (RKKY) interaction.

Magnetic insulators have the electronic property of association with atomic sites, meaning the magnetism depends on intra-atomic and local quantities.

### 2.5.3   Exchange Interaction Parameter

#### 2.5.3.1   The Heisenberg Model

The determination of the exchange interaction parameter stands upon different Spin-models, the most common, the Heisenberg model. The Heisenberg model is an extension to the Ising model, which grants the spins to point either up or down, with no phase transitions. The Heisenberg model permits the spins to behave classically with their degrees of freedom and can point in any three-dimensional direction. It is essential to note the distinction between the dimensionality of the lattice, d, and the dimensionality of the spins themselves, D-the order parameter. The Heisenberg Hamiltonian can be adapted to allow for discovering the type of magnetic interactions between the nearest, next-nearest and next-next-nearest neighbours within the system. The nearest-neighbour Heisenberg Hamiltonian takes the form of:

$$\hat{H} = -\sum_{\langle ij \rangle} J_{ij} \mathbf{S}_i \cdot \mathbf{S}_j \tag{2.5.2}$$

Where J is the exchange interaction parameter, and the spins $\mathbf{S}_i$ are treated as three-dimensional vectors as the spin is allowed to point in any one of three-dimensional spaces. The exchange interaction parameter between the spins is isotropic and in a localised spin system. When J>0 the arrangement of the spins between the nearest neighbours is ferromagnetic and if J<0 the arrangement is antiferromagnetic.

#### 2.5.3.2   Broken Symmetry Approach

The Broken-Symmetry approach (BS-approach) [46] is one of many strategies to extract the exchange interaction parameter from the system. The BS-approach relies upon the Heisenberg Hamiltonian. As its namesake suggests, the BS-approach operates through breaking the magnetic symmetry to determine the effective exchange interaction parameter. The BS-

approach Hamiltonian mirrors the Heisenberg Hamiltonian, with slight differences:

$$H = J \sum_{i<j}^{N} S_i \cdot S_j \qquad (2.5.3)$$

where $S_i(S_j)$ represent the magnetic moment on ion i (j), N is the total number of magnetic centres and J is the isotropic exchange interaction parameter for the nearest neighbours.

The total energy of a 1D system with cyclic boundary conditions can be calculated through:

$$E^{tot} = J \sum_{i=1}^{N} S_i \cdot S_{i+1} + S_N \cdot S_1 \qquad (2.5.4)$$

The BS-approach extracts the exchange interaction parameter through the energetic difference of the high-spin ordered (high symmetry) system and the broken symmetry system (low-spin ordered) as well as the total number of magnetic sites.

$$J_{ij} = \frac{E_{HS} - E_{BS}}{2S_i S_j} \qquad (2.5.5)$$

where the i$^{th}$ ion has the j$^{th}$ ion as its nearest neighbour. The exchange interaction parameter is an effective J as the value is determined via the interaction of all magnetic sites.

The BS-approach, despite its simplicity, works on a wide range of real magnetic systems. For more complex systems which require the need to include the spin-orbit interaction other, more complex, approaches exist but at a higher computational cost.

### 2.5.3.3 The Quantum Chemistry Approach

Quantum chemistry offers means to determine exchange interaction parameters. A multi-configurational scheme allows for a mixture of different

spin configurations and ascertains the energy eigenvalues corresponding to different total spin values. For example, with two interacting spins, $\mathbf{S}_1$ and $\mathbf{S}_2$, we can surmise the total $\mathbf{S'}=\mathbf{S}_1+\mathbf{S}_2$. This provides:

$$2\mathbf{S}_1\mathbf{S}_2 = \mathbf{S}^{\prime 2} - \mathbf{S}_1^2 - \mathbf{S}_2^2 \qquad (2.5.6)$$

with the eigenvalues:

$$[S'(S'+1) - S_1(S_1+1) - S_2(S_2+1)]$$

In the case where $S_1 = \frac{1}{2}$ and $S_2 = \frac{1}{2}$, the states produced are a singlet ($S'$=0) and a triplet ($S'$=1). The Heisenberg Hamiltonian eigenvalues are $\frac{3}{2}$ J and $-\frac{1}{2}$ J, respectively. Relating this to first-principles, basis functions are usually pure spin states, with the basis of spin functions $|\mathbf{m}_{S_1}, \mathbf{m}_{S_2}\rangle$, where our case has $S_1 = \frac{1}{2}$ and $S_2 = \frac{1}{2}$, the Heisenberg Hamiltonian takes for the shape of:

| $\mathbf{m}_{S_1}\mathbf{m}_{S_2}$ | $\left\|\frac{1}{2}\frac{1}{2}\right\rangle$ | $\left\|-\frac{1}{2}\frac{1}{2}\right\rangle$ | $\left\|\frac{1}{2}-\frac{1}{2}\right\rangle$ | $\left\|-\frac{1}{2}-\frac{1}{2}\right\rangle$ |
|---|---|---|---|---|
| $\left\|\frac{1}{2}\frac{1}{2}\right\rangle$ | $-\frac{J}{2}$ | | | |
| $\left\|-\frac{1}{2}\frac{1}{2}\right\rangle$ | | $\frac{J}{2}$ | $-J$ | |
| $\left\|\frac{1}{2}-\frac{1}{2}\right\rangle$ | | $-J$ | $\frac{J}{2}$ | |
| $\left\|-\frac{1}{2}-\frac{1}{2}\right\rangle$ | | | | $-\frac{J}{2}$ |

Through mixing the different $\mathbf{m}_s$ values via basis transformation, diagonalisation of the Heisenberg Hamiltonian takes place. Whereby the singlet and triplet states are represented, respectively, via:

$$S = 0 \quad E = \frac{3}{2}J \quad \frac{1}{\sqrt{2}}\left(\left|\frac{1}{2}-\frac{1}{2}\right\rangle - \left|-\frac{1}{2}\frac{1}{2}\right\rangle\right)$$

$$S = 1 \quad E = -\frac{1}{2}J \quad \begin{cases} \left| \frac{1}{2} \frac{1}{2} \right\rangle \\ \frac{1}{\sqrt{2}} \left( \left| \frac{1}{2} - \frac{1}{2} \right\rangle + \left| -\frac{1}{2} \frac{1}{2} \right\rangle \right) \\ \left| -\frac{1}{2} - \frac{1}{2} \right\rangle \end{cases}$$

The singlet and triplet states eigenvalues ($E_s$ and $E_t$, respectively) are instantly accessible in the above quantum chemistry multi-determinantal representation. Moreover, this representation offers a direct relationship with first-principles, letting the results map onto the Heisenberg model.

$$E_s - E_t = 2J \tag{2.5.7}$$

The disadvantage of this method comes from large systems such as molecular magnets, where the number of interactions exceeds computational resources and requires reduction. In addition, this method offers uncertainty about the result as only a tiny portion of the total number of interactions can be included in the diagonalisation.

# Chapter 3

# Colossal Magnetoresistance in Tl$_2$NiMnO$_6$

## 3.1 Introduction

Perovskite compounds are notorious for exhibiting unique magnetic behaviour, significantly influenced by other characteristics within the material [47–53] —for example, the multiferroic BiFeO$_3$ exhibits ferroelectricity ferromagnetism at room temperature from a lone pair Bi$^{3+}$ ion [54–59]. The importance of understanding these behaviours cannot be understated for their use in spintronics and future technologies.

The perovskite structure follows the form of ABX$_3$, where A and B are cations, and X (typically oxygen) is an anion, see Figure 3.1a for visualisation. The interesting magnetic behaviour continues to the double perovskites, which, as their namesake suggests, extends the perovskite's structural form.

The double perovskite possesses a structure consistent with A$_2$BB'O$_6$, where A is usually a rare-earth metal (but not exclusively) and B/B' are two transition metals, see Figure 3.1b for a visulation.

Double perovskites offer a rich insight into complex magnetic phenomena, such as magnetoresistance, magneto-capacitance and magnetodielectric behaviour [60–64]. These magnetism-dependant properties often emanate from phase changes, half-metalicity or spin-lattice coupling [65–67]. Of these phenomena, magnetoresistance provides the broadest range
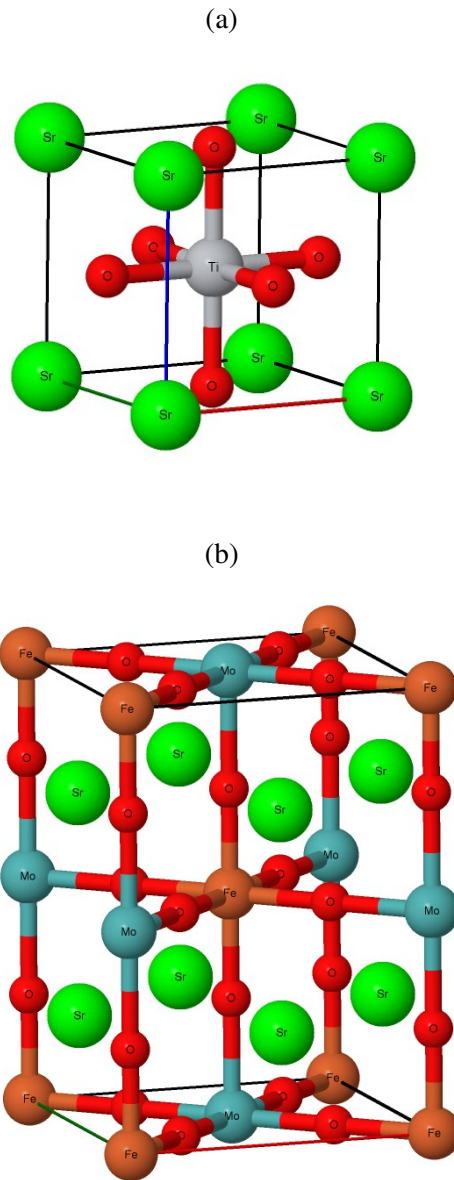
Figure 3.1: The perovskite structure as demonstrated by $SrTiO_3$ (a) and the double perovskite structure demonstrated by $Sr_2TiMoO_6$ (b).

of occurrence in strength; with a giant- and colossal magnetoresistance appearance [60, 63, 65–67]. These relate to the intensity of the resistance caused, with colossal as the more significant phenomenon.

Double perovskites are not limited to a single magnetic configuration and are found to have ferromagnetism such as $La_2NiMnO_6$ [68], $Sr_2FeMoO_6$ [69] and $Cr_2CrReO_6$ [70] as well as ferrimagnetism, for instance, $Cr_2CoMnO_6$ [71] and $A_2CrOsO_6$ (A=Sr,Ca) [72], and antiferromagnetism as found in

Ba$_2$PrRuO$_6$ [73] and Mn$_2$MnReO$_6$ [67]. Of these magnetic configurations magnetoresistance can manifest with little discrimination, between those magnetic states, in the frequency of which they appear in nature. For instance, the antiferromagnetic double perovskite, Sr$_2$CrWO$_6$, shows giant magnetoresistance [74], as does the ferrimagnetic Mn$_2$FeReO$_6$ [66], while the ferromagnetic La$_2$NiMnO$_6$ shows room-temperature magnetoresistance [75].

In trying to characterise the origins of these elaborate magnetic exhibitions, it is often helpful to look towards the electron-densities around the Fermi-energy as these contribute towards the Fermi-surface shape, and ultimately the transport properties.

First-principles investigations can provide insight into the electronic structure deep inside the material through the electronic density of states and band structures. For example, DFT calculations have offered explanations to the complex magnetism observed in double perovskites, such as the orbital magnetism of Sr$_2$FeMoO$_6$, Sr$_2$FeReO$_6$ and Sr$_2$CrWO$_6$ [76], through electronic structure investigations. Further, the *ab initio* investigation into the electronic transport and magnetotransport of Sr$_2$Fe$_{1+x}$Mo$_{1-x}$O$_6$ by Carvajal *et al.* [77]. Finally, the systematic DFT investigation performed by Bartel *et al.* on the Cs$_2$BB'Cl$_6$ double perovskite determined the suitability of band gap for optoelectrical applications [78]. These reveal the suitability of first-principles methods in determining the electronic structure of double perovskites and their complex magnetic relationships.

This chapter examines the double perovskite, Tl$_2$NiMnO$_6$, electronic structure, modelling the occupational disorder via the virtual crystal approximation [79, 80]. We shall also examine the band structure and density of states to gather information on the suspected insulating nature. We will also observe magnetic interactions and utilise the effective masses of the electrons and holes to determine transport properties with potential links the colossal magnetoresistance.

## 3.2 A Disordered Nature

The crystal structure of $Tl_2NiMnO_6$ possesses varying degrees of disorder caused by the occupancy of the $Ni^{2+}$ and $Mn^{4+}$ cations. Through quantitative refinement of the neutron diffraction data in the Rietveld plot, Ding *et al.* [81] determined the Ni/Mn occupation to be 0.85/0.15 and 0.658/0.342 on the B/B' sites, respectively. This culminated in the notion of an ordered (70%) and disordered (31.6%) samples. The degree of ordering was quantified as $|P_{Ni}-P_{Mn}|/(P_{Ni}+P_{Mn})\times100$, where $P_{Ni}$ and $P_{Mn}$ are the probabilities of occupying the B and B'- site by the Ni and Mn ions. However, the experimental analysis, which determined colossal magnetoresistance, was on the 70% ordered sample. Therefore, the DFT calculations were performed on this structure to allow for maximum experimental comparison and coherency.

Disordered materials are a computationally challenging area to study due to the lower symmetry and size of the unit cell. There are two approaches to consider with disordered materials, the "direct" approach (a phrase coined by Vanderbilt) [80] and the computationally inexpensive virtual crystal approximation (VCA) [79, 80].

The direct approach invokes a supercell to study one or more disordered configurations with artificially imposed periodic boundary conditions. The calculations involved in this approach are computationally demanding due to the use of very large supercells to mimic the distribution of local chemical environments.

The VCA employs the crystal within the primitive periodicity and composes the cell of fictitious "virtual" atoms that interpolate between the behaviour of the atoms with the parent compounds.

Electronic structure calculations using the VCA approach have been used with a reasonable degree of accuracy [82]. However, the effects of local distortions around atoms are not considered under the VCA approach

and cannot recreate the finer details of disorder in materials [80, 83–85]. Thus, the accuracy of the VCA scheme has limits. Nevertheless, while it is not appropriate for some semi-metals and soft mode lattice dynamics [86–88], it has shown good accuracy for ferromagnetic materials and other semi-metals [82, 89–93]. Further to this, Ramer *et al.* [94] show the VCA successfully describing ferroelectric perovskite solid solutions. The remit of this investigation is to use DFT, through electronic band structure, to provide insight into a ferromagnetic insulating double perovskite and to use effective masses to indicate transport properties, observing any initial colossal magnetoresistance effects. Thus, the VCA should provide a good approach.

## 3.3 Results

The results for this investigation orientate around the fine-grid sampling; see section 2.3.2 for more information. The first-principles calculations utilised a coarse fine-grid and a denser fine-grid, revealing the importance of converging this parameter for reliable *ab initio* studies.

### 3.3.1 Electronic Structure

Table 3.1 reveals the optimised lattice parameters for the coarse and dense fine-grid scales and compares them to the experimental values of Ding *et al.* [81]. The PBE lattice parameters optimised to a=5.31Å, b=5.39Å, and c=7.71Å, and a=5.25Å, b=5.36Å, and c=7.70Å for the coarse and fine-grid scales, respectively. We observe slight differences between the grid densities, with the fine-grid predicting smaller lattice parameters than the coarse grid. However, both optimisations are within 2% of the experimental values, which is a good agreement.

| | a (Å) | B (Å) | (Å) |
|---|---|---|---|
| Ding *et al.* | 5.27 | 5.39 | 7.67 |
| Coarse Fine Grid Scale (1.75) | 5.31 | 5.36 | 7.71 |
| Denser Fine Grid Scale (4.5) | 5.25 | 5.36 | 7.70 |

Table 3.1: The optimised lattice parameters compared to experiment, by Ding *et al.*[81]
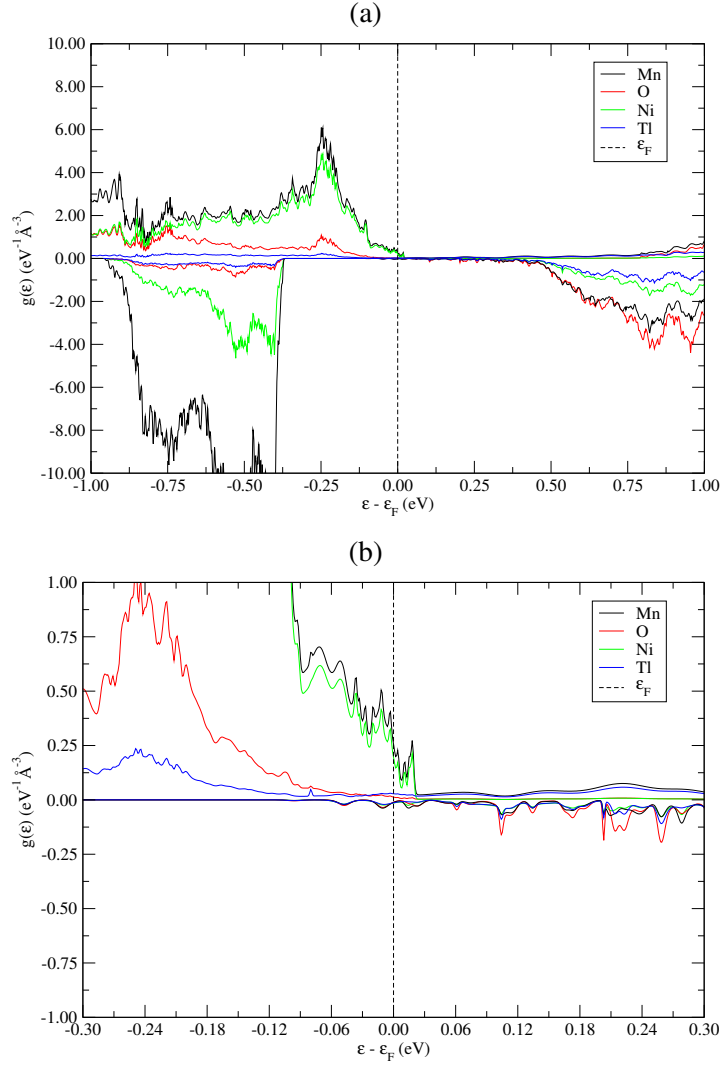


Figure 3.2: The partial density of states (PDOS) of $Tl_2NiMnO_6$ (a) compared with a close up around the Fermi-energy (b). PDOS obtained through use of the OPTA-DOS code [95, 96].The positive and negative regions of the DOS correspond to the majority and minority spin channels respectively.

Figure 3.2 shows the density of states for the coarse fine-grid scale; there was no significant visual difference with the denser fine-grid scale

The density of states at the Fermi-energy is 0.09 eV$^{-1}$Å$^{-3}$ for minority spin (beta) electrons and 0.67 eV$^{-1}$Å$^{-3}$ for majority spin (alpha) electrons for the coarse fine-grid scale and 0.56eV$^{-1}$Å$^{-3}$ and 0.06eV$^{-1}$Å$^{-3}$ for majority and minority spin electrons in the dense fine-grid scale. The density at the Fermi-level corresponds to a low carrier concentration and thus a poor conductor.

Further, there is a strong dominance of majority spin electrons below the Fermi-energy. The difference in occupation between majority and minority spins at and around the Fermi-level indicates Stoner ferromagnetism.

There is no band gap in the electronic density of states, in contradiction to the experimentally determined insulating nature of Tl$_2$NiMnO$_6$ [81]. The ions which contribute most to the density of states around the Fermi-energy are Ni and Mn. These ions are transition metals, which are well-known examples of DFT underestimating or failing to predict their band gaps [97]. Therefore, the Hubbard-U on-site correction was introduced.

Figures 3.3a-3.3d show the band structures of the coarse fine-grid and dense fine-grid scales, with their respective Hubbard-U values, added to the d-orbitals of the Ni and Mn ions. The central aspect of Figures 3.3a-3.3d is the difference in the number of valance bands, caused, in part, by the increased Hubbard-U value and the denser fine-grid scale changing CASTEPs representation of the charge density through different sampling rates.

Due to the different sampling rates caused by the fine-grid scale, the Hubbard-U values are significantly different and are determined via the plateau method, which involves increases the Hubbard U value and comparing the effects on forces, stress or ground state energy. This method is similar to typical convergence testing, however, the focus is on observing a plateau in the graph. In the plateau region, the effects of increasing the Hubbard U value on the properties of the system are similar and so a value from the region is selected. The difference in Hubbard-U values ultimately
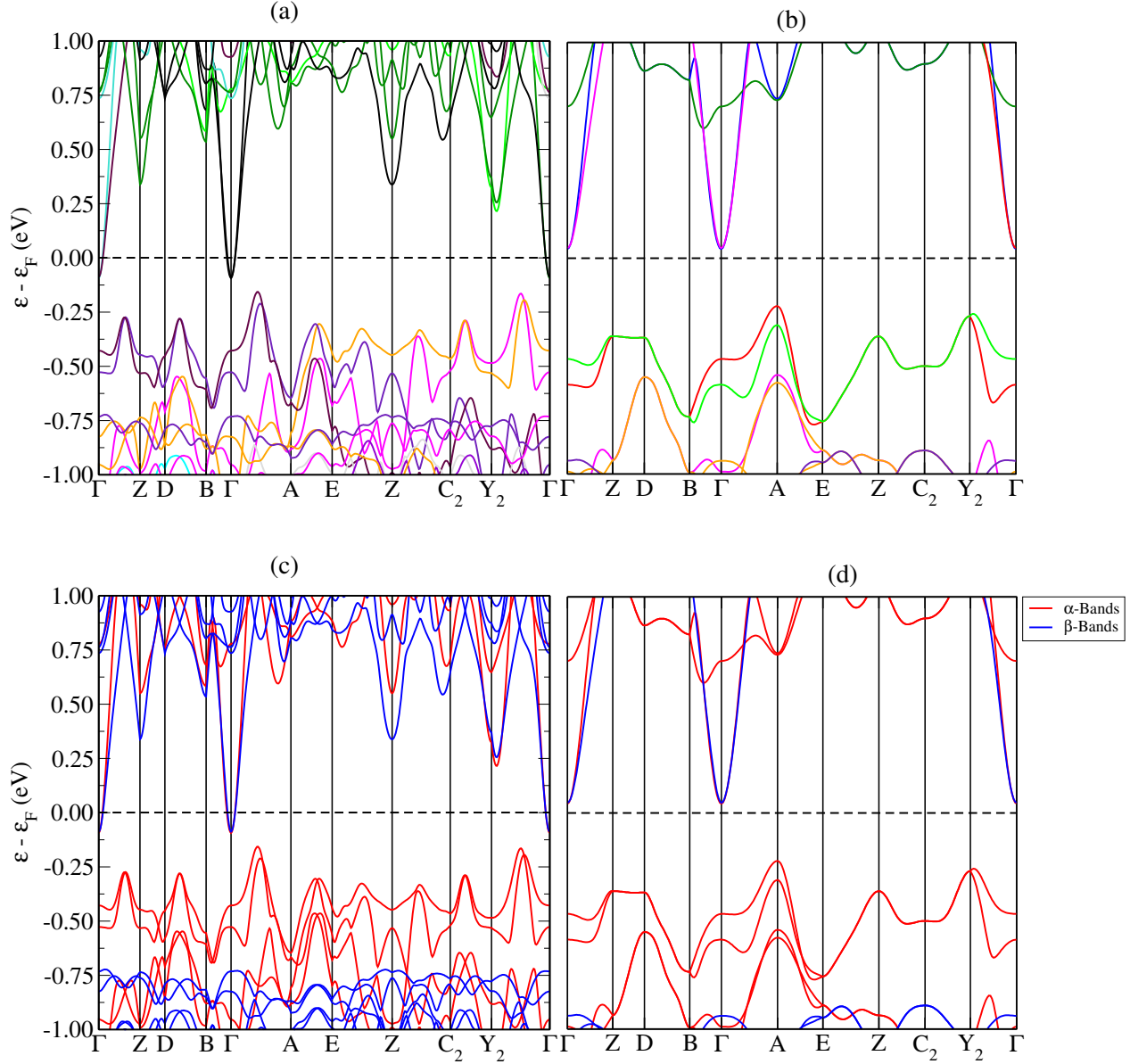
Figure 3.3: A comparison of the band structure for $Tl_2NiMnO_6$ between the coarse fine-grid (a), (c) and the dense fine gird (b),(d). Hubbard-U values of 1.50(3.00)eV and 1.25(2.75)eV for Mn and Ni, respectively for the coarse (dense) fine-grid scale. The distinction between $\alpha$- and $\beta$-bands in (c) and (d) are in colour and is used to demonstrate the majority spin channels dominance. Path through the Brillouin zone was chosen via SeeK-Path [98, 99]. The main source of the difference the bands between (a),(c) and (b),(d) come from effects of the increased Hubbard-U value.

affects the size of the band gap; however, both fine-grid scales produce a gap size associated with a semi-conductor and not an insulator.

The electronic band structure and density of states clearly show that

| Magnetic Moment ($\mu_B$) | Ni | Mn |
|---|---|---|
| Ding *et al.* | 0.99 | 1.51 |
| Coarse Fine Grid Scale (1.75) | 0.72 | 1.62 |
| Denser Fine Grid Scale (4.5) | 0.73 | 1.65 |

Table 3.2: The magnetic moments on the ions Ni and Mn compared to experimental values, by Ding *et al.*[81]

$Tl_2NiMnO_6$ possesses a ferromagnetic ground state. Table 3.2 reveals the magnetic moments associated with the ferromagnetic state for the coarse and dense fine-grid scales. There is very little difference between the magnetic moments of the different samplings, at a mean value of $0.02\mu_B$. Both the coarse and dense fine-grid scales underestimate the magnetic moments on the Ni ions by around 26%, while simultaneously overestimating the Mn magnetic moments by around 8% when compared to experimentally determined moments by Ding *et al.* [81].

There are residual magnetic moments, varying in strength between $0.2\mu_B$-$0.6\mu_B$, for Tl and O. This behaviour indicates itinerancy, which agrees with the electronic structure and the delocalisation apparent within the density of states, symbolising metallic behaviour.

Despite the drastic changes in the electronic structure between the coarse and dense fine-grid scales, the overarching behaviour is the same: the band gap is insufficient to exhibit insulating behaviour but instead demonstrates semiconduction, which does not prevent colossal magnetoresistance [100].

### 3.3.2 Effective Masses of Electrons and Holes

Due to the band structures exhibiting semiconduction, the effective masses of the charge carriers can be determined.

In semiconduction, electrons will cross the band gap between the valance

and conductions bands via excitations. Therefore, the minimum of the conduction band at $\Gamma$ will almost exclusively contain electrons, and the maxima of the valance band at point A will contain holes (see Figures 3.3b and 3.3d). Therefore, the energy-wave-vector for the charge carriers can be approximated using a modelled quadratic equation around the extrema as they are parabolic in these regions [100]. In this parabolic nature, the energy-wave-vector diagrams resemble a free electron, as described in the Kronig-Penney Model [101], the energy is represented by:

$$E = \frac{\hbar^2}{2m_{e,h}}k^2$$

where

$$\frac{d^2E}{dk^2} = \frac{\hbar^2}{m_{e,h}}$$

$$\therefore m_{e,h}^* = \hbar^2 \Big(\frac{d^2E}{dk^2}\Big)^{-1} \tag{3.3.1}$$

and $m_{e,h}^*$ is the effective mass of the electron or the hole [102].

The second derivative of energy with respect to the wave-vector is determinable through the quadratic curve fitting of the relevant bands in the electronic band structure, see Figures 3.3b and 3.3d. The equation describing that fitted curve represents the energy as a function of the wave-vector; differentiating this twice provides a value fitting the format of Equation 3.3.1.

The quadratic fittings in Figure 3.4 reveals a relatively good match for the conduction bands, partly due to the narrow nature of the parabolas. For the valance band, the broadness of the parabola in the $\Gamma$-A directions has made it difficult for the curve-fitting software to marry up the two. Through closer observation of the band, it can be considered two separate curves; that is, the shape of the parabola in the $\Gamma$-A direction is significantly broader than the shape in the A-E direction.

In principle, these two directions can be modelled through separate curves
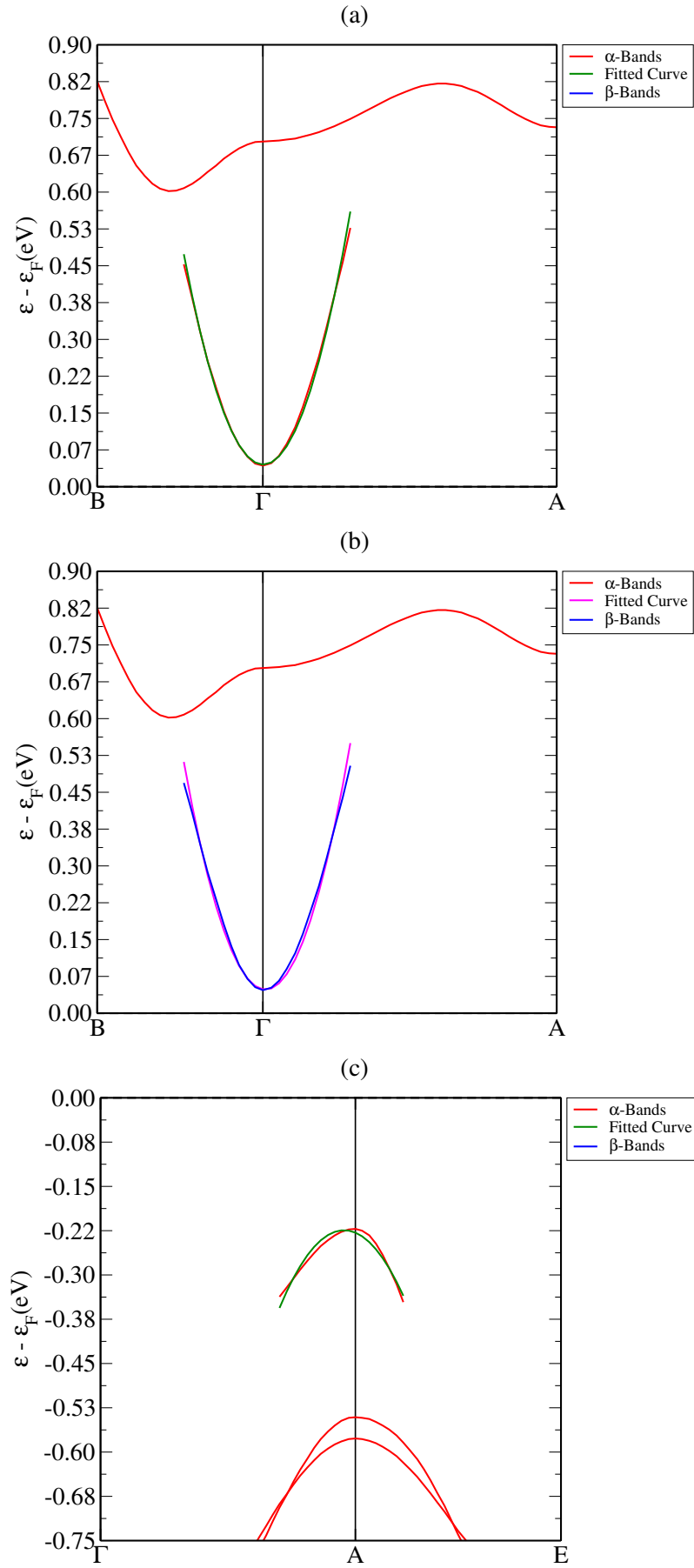
Figure 3.4: The quadratic curve fitting for the parabolic region of the bands. Zoomed in sections of the band structure shown in Figure 3.3. Figure (a) and (b) relate to the conduction bands for $\alpha$- and $\beta$-bands, respectively, and (c) relates to the $\alpha$ valance band. Some bands have been removed for clarity.
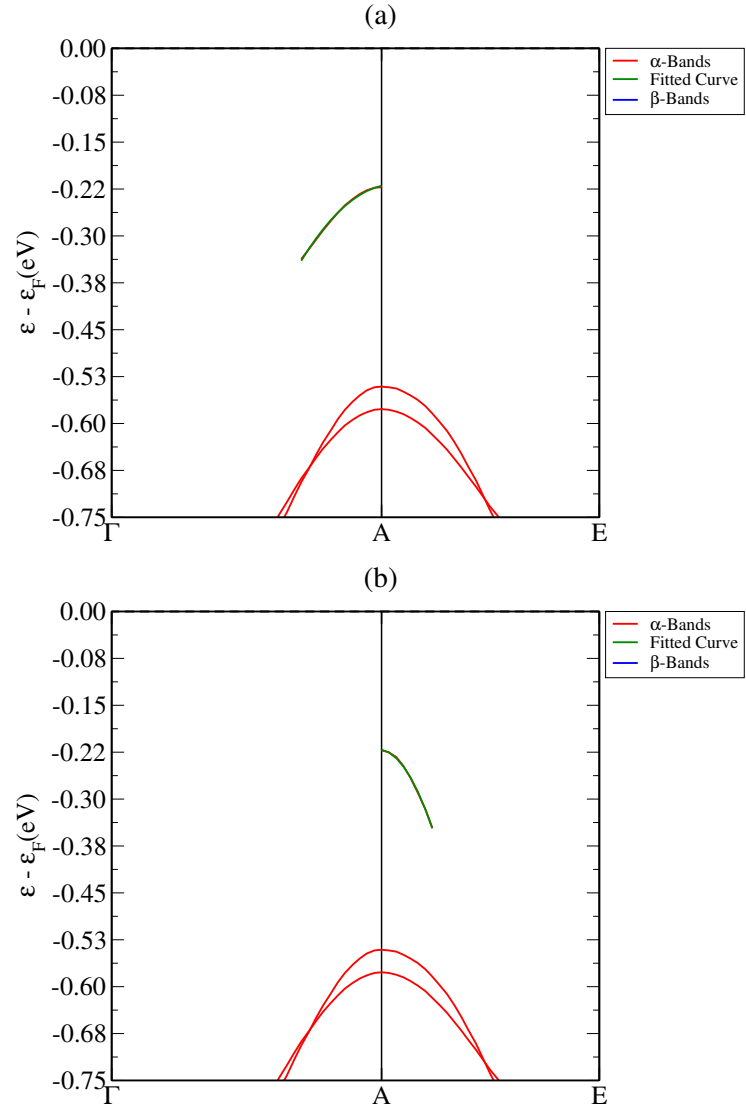
Figure 3.5: The quadratic curve fitting for the $\alpha$ valance band split between the directions $\Gamma$-A (a) and A-E (b). Some bands have been removed for clarity

fittings to accommodate anisotropy between these directions, as seen in Figure 3.5.

| | Symbol | |
|---|---|---|
| **Band minimum at $\Gamma$** | | |
| Minimum Energy | $E_{\alpha,c}$ (eV) | 0.0430 |
| Effective Mass | $m_e^*/m_o$ | 0.0119 |
| Minimum Energy | $E_{\beta,c}$ (eV) | 0.0470 |
| Effective Mass | $m_e^*/m_o$ | 0.0116 |

Table 3.3: The effective masses of the electrons as well as the bands minima used to determine them.

| | Symbol | |
|---|---|---|
| **Band Maximum at A** | | |
| Maximum Energy | $E_{\alpha,v}$ (eV) | -0.2219 |
| **Direction $\Gamma$-A** | | |
| Effective Mass | $m_h^*/m_o$ | 0.0673 |
| **Direction A-E** | | |
| Effective Mass | $m_h^*/m_o$ | 0.0217 |

Table 3.4: The effective masses of the holes in direction $\Gamma$-A and A-E.

Comparing the curve fitting of the majority spin valance band between Figures 3.4 and 3.5 shows a significant improvement in curve fitting through treating the two directions separately, suggesting greater confidence in the effective masses obtained.

The effective masses for the electrons as seen in Table 3.3, show two values for the electron masses corresponding to the majority spin (alpha) and minority spin (beta) electrons. The difference between these conduction electron masses are slight and can be considered indistinguishable as they are the band minima energy.

The holes mass found from the valance band, as seen in Table 3.4, are significantly heavier than the electron masses; this is not alarming given the shape of the band. The broadness of the valance band and the heaviness of the holes suggest that the holes are mainly responsible for charge-carrying in the system. The difference between the effective masses of the

holes in the different directions indicates that there will be different transport properties in these directions. The $\Gamma$-A direction effective mass is over three times heavier than the hole in the A-E direction, suggesting the difference in transport properties to be significant. The effective masses of the holes are relatively light when compared to silicon; however, with heavier elements, such as germanium [103], the values become less stark in contrast.

## 3.4   Discussion

The significant number of majority spin bands immediately below the Fermi-energy in Figure 3.3 indicates dominance of that spin channel as charge carriers. In addition, the elongated band at the $\Gamma$ point reduces the size of the band gap and offers the hopping of excited electrons, indicating that the double perovskite is a semiconductor. While the semi-empirical nature of Hubbard-U makes it unwise to discuss the size of the band gap quantitatively, qualitatively, it is small enough for excitations to overcome and does not alter the justification of the semiconducting conclusion.

The first-principles calculations converge to a ferromagnetic ground state, which agrees with Ding *et al.* [81]. However, there is around a 26% difference between magnetic moments. This could be related to the VCA scheme with the mixed occupancy on the magnetic ions but would require further investigations. Without spin-orbit coupling, the directions of the moments with respect to the crystal cannot be determined. Itinerancy can be observed from the broadness in the density of states and valance bands, as well as the residual magnetic moments on the Tl and O ions.

The difference in the masses of the holes in the valance band indicates that the $\Gamma$-A direction allows for a more straightforward travel than the A-E direction. This anisotropy could be a possible consequence of the material exhibiting magnetoresistance, forcing anisotropy on the charge carriers.

Furthermore, the difference in effective masses between the holes and the electrons shows that there is a disparity between their contribution to charge transport; this could assist in explaining the magnitude of the magnetoresistance observed in the system, as the holes are heavier and are exclusively majority spin holes. However, scattering rates have not been investigated and so determination of which charge transport mechanism plays a larger role (if any) cannot be stated. Furthermore, the difference in these masses adds more weight to this material exhibiting semiconducting behaviour. However, this would require the use of spin-orbit coupling and modelling an external field to confirm a relationship between the effective masses of the charge carriers and the colossal magnetoresistance.

The use of the VCA approach to model the occupational disorder rendered different results compared to the experimental. While the optimisation of the unit cell proved to be within the expected difference associated with PBE, there was a lack of insulating behaviour. It is unclear whether this is the shortcoming of VCA or a broader issue facing DFT that would require further investigations using the direct supercell method.

## 3.5   Conclusion

In conclusion, the *ab initio* investigation into the double perovskite, $Tl_2NiMnO_6$, reveals a ferromagnetic semiconducting ground state. Furthermore, the strong dominance of majority spin bands below the Fermi-energy indicates polarised charge carriers and dependence of transport properties on applied magnetic fields at finite temperature.

The difference in effective masses between the electrons and holes indicates an unequal contribution to transport in the system. However, further investigations involving scattering times are required to understand the nature of the divergence. This is incompatible with insulators but not for semiconductors. Furthermore, the disparity between heavy and light

holes reveals anisotropy within the material between different directions, potentially related to the colossal magnetoresistance.

## 3.6 Future Works

Further work is required with spin-orbit coupling to determine if the difference in masses for the holes between $\Gamma$-A and A-E relates to the direction of and external field. Spin-orbit coupling would also reveal any split-off hole valance bands as it would provide the spin-orbit energy introducing hyperfine splitting to the valance bands. Further work is also required to gather a more complete picture of the effective masses with the effective mass tensor for the majority spin valance bands and reconcile the multiple values. Further work should look into using different codes and software to calculate the effective masses of the holes and electrons.

The direct supercell method is needed to determine if the differences with experimental values emerges from the VCA approach or the level of theory implemented.

# Chapter 4

# Molecular Magnets

## 4.1 Introduction

Olivier Kahn, who is considered one of the founders of the research topic, described molecular magnetism as "*dealing with magnetic properties of isolated molecules and assemblies of molecules*" [104]. While the experimental and theoretical methods for studying molecular magnets has changed since those words [105], the fundamental defining nature of them has not. The versatility of synthesis for molecular magnets renders accessibility to a host of experimental probes, characterising the physical and magnetic attributes, such as optical, X-ray, Mössbauer and neutron spectroscopies, SQUID magnetometer, electron paramagnetic resonance and scanning microscopes [106–109]. The rich experimental basis for investigation birthed multiple theoretical frameworks. Such models included the isotropic exchange limit (Heisenberg model) and the fully anisotropic exchange limit (Ising model) [110]. These models had success in describing the characteristic magnetic behaviour exhibited by the molecular magnets, a minimum in the magnetic moment at a given temperature and accompanied by divergence at lower temperatures. The particular success of these models is orientated around correctly determining the strength and degree of anisotropy of the exchange coupling between two alternating spins [104, 111–115].

Following the initial success of molecular magnetism, the field grew into one where chemists designed materials with increasing complexity while physicists studied the novel magnetic phenomena observed [116]. Two

main classes of molecular magnets emerged through this development: single-molecule magnets (SSM) and multifunctional magnets [107].

As their namesake suggests, single molecular magnets are versatile single molecules exhibiting strong ground state magnetism, a negative zero-field splitting parameter and a spontaneous magnetic moment in line with the easy axis. SMMs display magnetic bistability at low temperatures owing to an energy barrier for magnetisation reversal. This means that the SMMs can become frozen in one of two potential wells; an effective magnetic memory [107, 117]. SMMs are often termed molecular nanomagnets due to their ability to become crystallised and have weak intermolecular interactions. This feature provides an advantage for experimental probes as they mainly detect intramolecular interactions [109, 118]. The isolative nature of SMMs and the prospect of manipulating them makes their use desirable for classical computer storage systems, future quantum computing and other spintronic areas [107, 109, 118]. Therefore, understanding the mechanisms responsible for their magnetism is vital to their widespread use.

This chapter uses *ab initio* calculations to understand the underlying mechanisms that experimentally generate different total magnetism ($S_{tot}$) for the single molecular magnet, $Cr_{10}$. This chapter will also compare the exchange interaction parameters of the $Cr_{10}$ molecule with the $Cr_8$ molecule to characterise the effect of the frustrated next-nearest neighbour interactions in $Cr_{10}$. We also compare the methodology of using crystal symmetry to optimise the $Cr_8$ molecule with linear ionic constraints to optimise the $Cr_{10}$ molecule. The main objective for $Cr_8$ is to use it as a benchmark for comparison with the $Cr_{10}$ investigation.

The $Cr_{10}$ molecule has been experimentally observed in both a ferromagnetic and antiferromagnetic ground states [106, 108]. The reason behind this phenomenon is partially related to the distances between the magnetic sites and the methods employed in synthesis [108], although they

are not fully understood. We also seek to understand the importance of symmetry in the phenomenon of $Cr_{10}$ molecule.

## 4.2 The Molecular Structures

### 4.2.1 The $Cr_{10}$ Structure

The molecule $Cr_{10}(OMe)_{20}(O_2CCMe_3)_{10}$, hereon abbreviated to $Cr_{10}$, consists of a 10 Chromium ion ring as the main edifice, with two sets of Oxygen bridges and a third bridge consisting of two Oxygens and a Carbon ion, see Figure 4.1. $Cr_{10}$ is magnetically bistable with antiferromagnetic and ferromagnetic ground states, both exhibiting interesting magnetic properties. We received an experimental configuration of the molecule from T.G. (ISIS)[3], who used neutron diffraction to determine the structure and magnetic information. The $Cr_{10}$ molecule is considerably large with 270 ions, as seen in Figure 4.1.
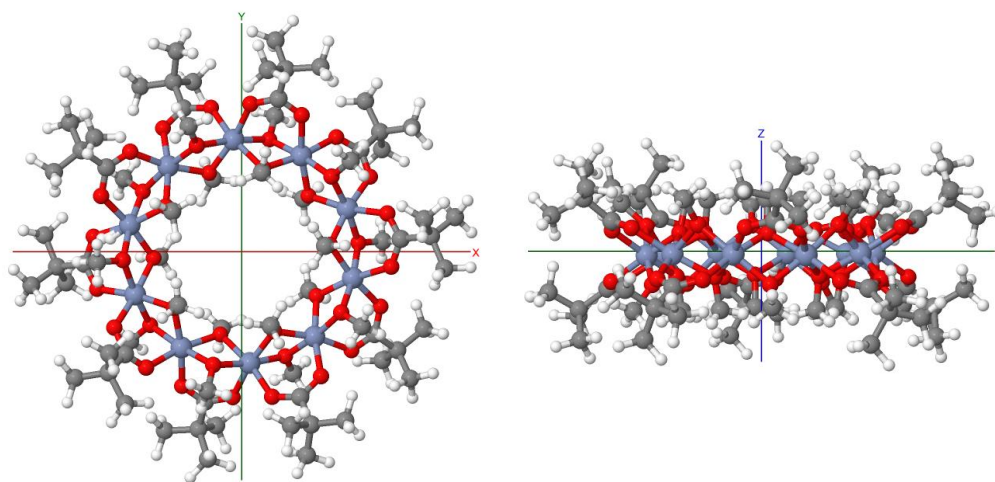


Figure 4.1: A visual representation of the $Cr_{10}$ molecular structure, with side-profile. Chromium, Carbon, Oxygen and Hydrogen are represented as the blue, grey, red and white spheres respectively.

Even with the significant advancements in computing, 270 ions are still too computationally exhaustive to perform straightforward *ab initio* calculations. This limit is due to the even larger number of electrons those 270 ions contribute to the calculation as DFT uses the electron density to find the ground state. Reducing the size of the molecule, and therefore the number of electrons is key to performing any calculations which can explore the magnetic character of $Cr_{10}$. The alterations ought to leave the exchange pathways unperturbed. It is clear from Figure 4.1 that only ions bonded to the core Cr-ring will be involved in magnetic exchanges. The extended methyl branches ($C$-$C$-$(CH_3)_3$ (referred to as pivalic groups) and an additional $CH_3$ (from the inner molecule) contain 180 ions and are not directly involved in magnetic exchanges. Therefore they would only add to the complexity of calculations while not providing any helpful insight into the magnetic workings of the molecule.

Furthermore, the methyl branches contain overlapping ions, which register as molecular disorder in the INS data. These methyl branches can be removed and replaced with single Hydrogens in a process called Hydrogen saturation.

A pruning process is applied, as shown in Figure 4.2. The interior methyl groups start from the middle panel (imaging the bond $O$-$CH_3$ instead of $O_2C$-$CH_3$), and the exterior methyl group follow the pruning as shown in Figure 4.2 without deviation. The final configuration of the $Cr_{10}$ molecule contains no methyl groups as they have been replaced with an isovalent Hydrogen ion.

The justification of this saturation comes from a valency argument; the number of bonds which the Carbon and Oxygen ions take part in has not changed. Therefore, the replacement will not change the valency of the Carbon or Oxygen ions as the number of electrons in the bonds is unchanged.

The reduced molecule now possesses the chemical formula,
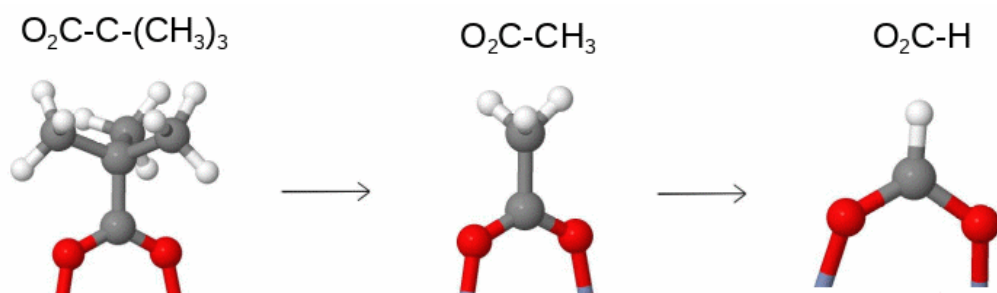
Figure 4.2: Illustrative representation of the pruning application adopted to approximate the $Cr_{10}$ molecule. Here, displaying the process on the outer branches.

$Cr_{10}(OH)_{20}(O_2CH)_{10}$, with a total number of ions at just 90, allowing for a considerable boost in computational speeds for first-principles calculations. Notably, the magnetic core of the molecule has been unaltered and remains close to the experimental structure, preserving the magnetic interactions and exchange pathways. From this reasoning, confidence can be given to accurately representing the full $Cr_{10}$ molecule in this saturated state.

### 4.2.2 The $Cr_8$ Structure

As with $Cr_{10}$, the molecule $Cr_8F_8(CO_2C(CH_3)_3)_{16}$ [119, 120] will be abbreviated to $Cr_8$. This ringed molecule, like $Cr_{10}$, consists of eight Cr ions as the core structure with Fluorine bridges. Methyl groups stem off the outer Carbon-Oxygen bridges, see Figure 4.3 where the methyl groups have been replaced with isovalent Hydrogen ions, forming a *de facto* formula of $Cr_8F_8(O_2CH)_{16}$.

The pruning and hydrogen saturation processes applied to the $Cr_{10}$ molecule, was also used on the $Cr_8$ molecule. For the $Cr_8$ molecule, this process is a standard computational method with precedence in previous *ab initio* calculations [119, 121].
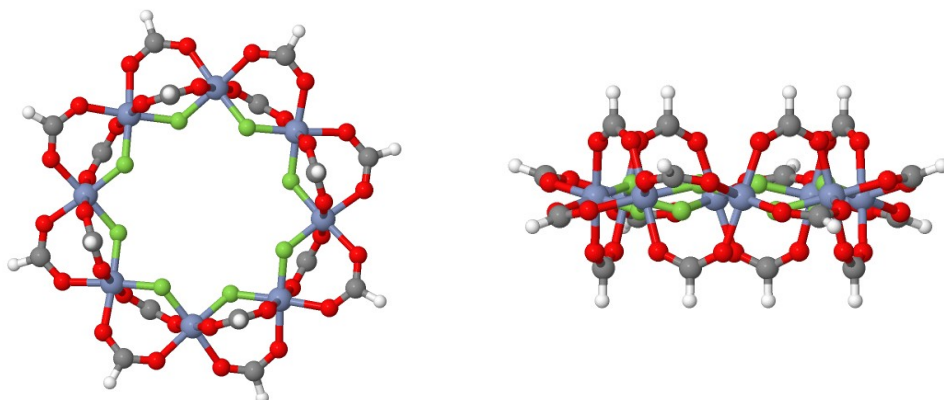
Figure 4.3: A visual representation of the Hydrogen saturated $Cr_8$ molecular structure. Chromium, Carbon, Oxygen, Hydrogen and Fluorine are represented as the blue, grey, red, white and green spheres respectively.

## 4.3 Symmetry of the Molecules

### 4.3.1 $Cr_8$ Symmetry

The synthesised structure of $Cr_8$ contains an asymmetric unit cell with two chromium and two fluorine atoms, bonded to four disordered methyl (pivalic) groups. The symmetry of the molecule is $D_4$, which can be represented through the crystal symmetry space group *P42₁2*. This involves treating the molecule as a crystal, relying on periodic boundaries to complete the ring. The full representation of this space group requires two formula units per unit cell to meet all the symmetry operations, see Figure 4.4.

In periodic DFT codes, such as CASTEP, crystal symmetry is very well represented [100]. Therefore, allowing the molecule to be expressed through crystal symmetry is preferred as it is well established and fully automated. The input in CASTEP to maintain the crystal symmetry of the ring during a geometry optimisation is a single line: *symmetry_generate* .
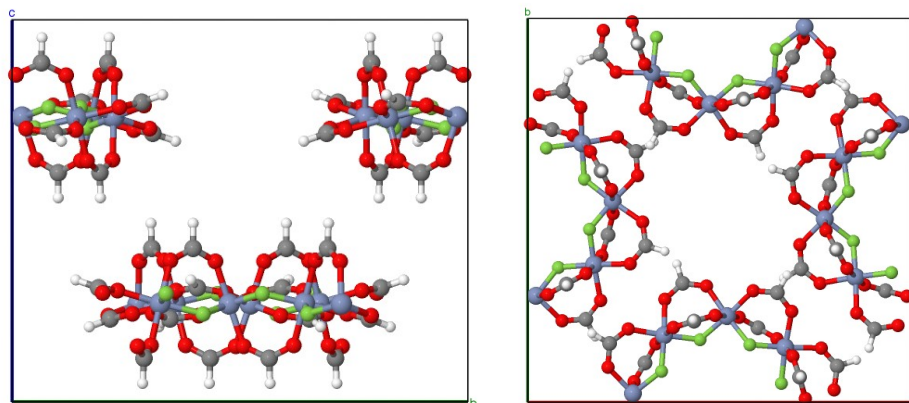
Figure 4.4: A visual representation of crystal symmetry representation of the $Cr_8$ molecular structure. The molecule is split in half at the unit cell boundary and utilises periodicity. Chromium, Carbon, Oxygen, Hydrogen and Fluorine are represented as the blue, grey, red, white and green spheres respectively.

### 4.3.2 Determining the $Cr_{10}$ Molecular Symmetry

The isolated $Cr_{10}$ molecule, however, cannot use crystal symmetry as it possesses a $\frac{2\pi}{5}$ rotational symmetry operation that is incompatible with any crystallographic space group (see Appendix A for further details on forbidden rotations in crystal symmetry). Therefore, any geometry optimisation in a periodic DFT code using the supercell approximation will break the molecular symmetry. The solution requires ionic constraints to maintain the integrity of the ring during relaxations (see Section 4.4). This section will show the justification of the $D_5$ symmetry we enforced in our calculations via ionic constraints.

Previous DFT investigations [106] have used the molecule with the methyl branches intact, as visualised in Figure 4.1. An issue with this representation is that it has no symmetry ($C_1$) resulting from the disordered methyl groups. Therefore, any optimisation will break the integrity of the molecular ring.

Removing the disordered methyl groups presented more structural sym-
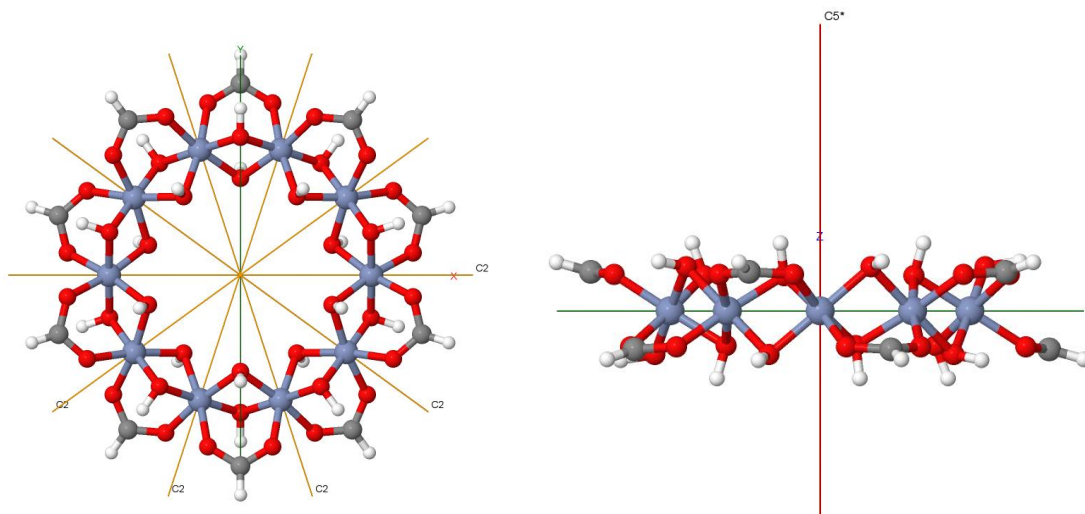
Figure 4.5: A visual representation of the $Cr_{10}$ molecular structure with $D_5$ symmetry imposed. Also displaying the five $C_2$ axes and the single $C_5$ rotation axes which form the $D_5$ point group. Chromium, Carbon, Oxygen and Hydrogen are represented as the blue, grey, red and white spheres respectively.

metry operations such as two rotation operators—one around the principal Z-axis, of $\frac{2\pi}{5}$ (the $C_5$ subgroup), and the other around the X-axis by $2\pi$ (the $C_2$ subgroup). Other valid symmetry operations are related to vertical mirror planes around the principal axis. The $C_5$ and $C_2$ subgroups belong to many different point groups, selecting which one best represents the molecule focused on two questions:

1. Is the movement of the ions relatively small to match the point group operations?

2. Is the point group compatible with the magnetic structure?

In answering the first of our questions, the root-mean-square displacement of ions, R-value, characterises how far the molecular structure has deviated to fit the point group. The smaller the R-value, the smaller the movement of the ions. There are many different ways of determining the R-value. In this instance, the R-value is determined by the graphical program, Chemcraft [122]. This software determines the R-value through the square root of the weighted average of the square of all atomic species

movements to produce a single value. The uncertainty associated with this operation for a system size of between 50-100 is $1 \times 10^{-14}$ Å.

The two point groups which possessed the smallest R-values were the $D_{5d}$ (R=0.00243) and the $D_5$ (R=0.00252) point groups. The difference between these point groups is in the five dihedral mirror planes in the $D_{5d}$ point group. As there is little difference between the R-values of these point groups, the second question helps determine which point group is most suitable. The $D_{5d}$ dihedral mirror planes break the antiferromagnetic structure, which the bistable $Cr_{10}$ molecule possesses. Therefore, the $D_5$ point group was chosen to be enforced in geometry optimisation (see Figure 4.5).

## 4.4   Ionic Constraints

As mentioned in the previous section, the $D_5$ point group is incompatible with crystal symmetry and cannot be used to optimise the molecule into bond equilibrium. However, optimisation under the $D_5$ molecular symmetry can be achieved through the use of linear ionic constraints.

A linear constraint describes a linear relationship between two variables, or in our case, ions. The linear constraint is a mathematical expression where linear terms, which are coefficients multiplied by a variable, are added or subtracted with the resulting expression forced to be greater-than-or-equal, less-than-or-equal, or exactly equal to the right-hand side value.

CASTEP [16] uses linear constraints to restrict the movement of ions in optimisations. The ionic constraints take the following linear form:

$$\sum_{k=1}^{N_s} \sum_{j=1}^{N_k} \sum_{i=1}^{3} a_{ijk}^n r_{ijk} = C_n \qquad (4.4.1)$$

where $a_{ijk}^n$ is the coefficient to the constraint for that ionic coordinate.

Equation 4.4.1 shows a linear constraint, as described above. The summations are for computational reasons and run over all the ion species ($N_s$), ions in that species ($N_k$) and all spatial coordinates of those ions (the index $i$). Each coordinate is given a coefficient, which are the respective individual elements of the rotation matrix.

For the $Cr_{10}$ molecule, implementing linear ionic constraints for the $D_5$ symmetry operations requires the rotation matrices of the $C_2$ and $C_5$ operations.

The $C_5$ and $C_2$ rotations apply to perpendicular axes, obeying the right-handed rule, the respective rotation matrices take the following form:

$$R_{C_5} = \begin{pmatrix} \cos\left(\frac{2\pi}{5}\right) & -\sin\left(\frac{2\pi}{5}\right) & 0 \\ \sin\left(\frac{2\pi}{5}\right) & \cos\left(\frac{2\pi}{5}\right) & 0 \\ 0 & 0 & 1 \end{pmatrix}$$

$$R_{C_2} = \begin{pmatrix} 1 & 0 & 0 \\ 0 & \cos(\pi) & -\sin(\pi) \\ 0 & \sin(\pi) & \cos(\pi) \end{pmatrix} \tag{4.4.2}$$

Applying the rotation matrices to an ion will rotate the ion into a new set of coordinates. For the $Cr_{10}$ molecule, each rotation maps an ion onto its rotation pair. The linear ionic constraint takes the form that the numerical difference in the coordinates of those two ions must be zero.

Implementing the ionic constraints comes with a limit to the number of constraints we can execute. That limit is the number of degrees of freedom, 3N; we want the molecule to be optimised and to do so, we must have fewer constraints than the number of degrees of freedom. Considering only the planar Cr ions, as seen in Figure 4.6, the limit for the number of

| Initial Ion's Number | Rotated Pair |
|:---:|:---:|
| 9 | 9 |
| 10 | 8 |
| 1 | 7 |
| 2 | 6 |
| 3 | 5 |
| 4 | 4 |

Table 4.1: The rotated pairs of Cr ions following the $C_2$ symmetry operation around the x-axis.

possible constraints is 3×10=30. However, there is the overall rotation of the molecule to consider, which requires three constraints to be removed from each species, resulting in a total number of constraints for the Cr ions as 27.
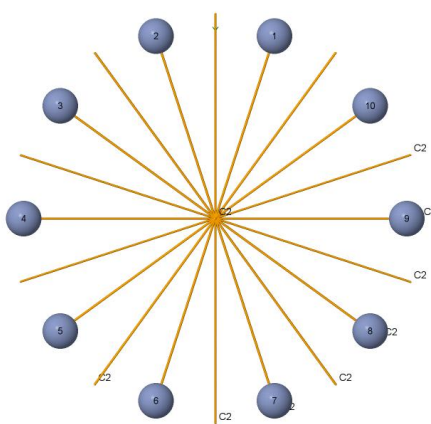


Figure 4.6: Illustration representing only the Cr ions within the central ring, exhibiting the five $C_2$ axes intersecting the Cr ions and the five $C_{2\theta}$ axes, bisecting the space between Cr ions.

In order to maintain the rotational symmetry of the molecule, only the generators are required in the constraints. The generators for the $D_5$ point group are the $C_2$ operation, laying on the x-axis and the $C_5$ operation, laying on the z-axis. The $C_2$ symmetry operation will map the Cr ions in a rotational pair as displayed in Table 4.1

The $C_2$ operation, therefore, includes four paired rotations and two rotations that map the ions onto themselves. These would generate $3{\times}6{=}18$ constraints, which is more than half of the total allowed constraints. Therefore, implementing both $C_2$ and $C_5$ rotations would create enough constraints to exceed the limit. Removing certain constraints will not affect the ring's integrity and reduce the number of constraints to below 27, thus overcoming this issue. For example, the $4^{th}$ and $9^{th}$ Cr ions are on the $C_2$ operation axis and and map onto themselves after the rotation, as seen in Table 4.1; thus, those operations can be represented through a reduced number of constraints. These ions only need to travel along the x-axis to allow the molecule to pucker. This is achieved by only applying the $C_2$ constraint on the y and z coordinates.

While this reduces the $C_2$ constraints down to 16, the contribution is still over half of the allowed constraints, requiring the removal of one further constraint. This process is then repeated for the $C_5$ constraints with the $C_5$ rotation matrix.

It is essential to consider under constraining and linear dependency. As its namesake suggests, the former is when there are too few constraints applied to the molecule, and the optimiser detects degrees of freedom that break the symmetry of the molecule. The latter is caused by the repetition of constraints. While reducing the number of constraints to below 27 satisfies the degrees of freedom limit, it does not ensure that the molecule is free from linear dependency or under constraining. Further, arbitrarily removing constraints might remove some necessary constraints and break the integrity of the ring through the optimisation.

Implementing the reduced $C_2$ and $C_5$ generator constraints introduces linear dependency due to an implicit constraint added from the ring's permutations. This implicit constraint requires the removal of the last set of constraints. For instance, with the $C_2$ constraints, the last set would be the ions intersected by the $C_2$ generator on the x-axis. For the $C_5$ constraints,

this would pertain to the fifth rotation. This, however, under constrains the system and breaks the circularity of molecule through optimisation.

Another form of constraining the molecule to maintain $D_5$ symmetry is the idea that using the successive application of rotations can be described by the multiplication of the rotation matrices. Therefore allowing the $C_5$ rotation to be described in the x-y plane:

$$R_{C2\theta} = R_{C5} \times R_{C2} \times R_{C5}^{\mathsf{T}} \qquad (4.4.3)$$

where $R_{C5}^{\mathsf{T}}$ is the transpose of the matrix and the multiplication is in reverse order (right to left) due to the non commutative nature of matrices and the formalism set out by the Euler treatment of angles. The full $D_5$ symmetry contains two sets of two fold axes as well as a $C_5$ axes. The two disjoint $C_2$ subgroups consists of axes which pass through the chromium ions and one which passes in between them. We chose to use a $C_{10}$ ($R_{C10}$) rotation matrix in Equation 4.4.3 to use the $C_2$ axes which passes in between the Chromium ions. The $C_{2\theta}$ rotation matrix ($R_{C2\theta}$) now has its rotation axes through the Cr ions, as seen in Figure 4.6, and implicitly applies the $C_5$ rotation while having its axes in the x-y plane. The generator axes for the $C_{2\theta}$ rotation no longer intersect Cr ions, therefore, the treatment for removing constraints to avoid linear dependency is different.
Removing a set of x,y,z constraints from both $C_2$ and $C_{2\theta}$ will leave the Cr ring under constrained. The solution is removing a single set of x,y,z constraints across both $C_2$ and $C_{2\theta}$, therefore not invoking linear dependency or under constraining; see Appendix B for further examples.

Finally, we have to implement these constraints in the CASTEP formalism outlined in Equation 4.4.1. The linear ionic constraints for the $C_2$ rotation ($R_{C2}$ in Equation 4.4.2), which maps the 10th Cr ion onto the 8th, takes the form:

| | | | | | |
|---|---|---|---|---|---|
| 1 | Cr | 10 | 1 | 0 | 0 |
| 1 | Cr | 8 | $-1$ | 0 | 0 |
| 2 | Cr | 10 | 0 | $-1$ | 0 |
| 2 | Cr | 8 | 0 | $-1$ | 0 |
| 3 | Cr | 10 | 0 | 0 | $-1$ |
| 3 | Cr | 8 | 0 | 0 | $-1$ |

The constraints are numbered to allow CASTEP to determine which ions are rotation pairs, and the elements of the rotation matrix are applied to the x,y,z coordinates of Cr ions 10 and 8. The linear constraint dictates that the difference in coordinate values between the original ion (8 from 10s perspective) and its rotation pair are zero, thus mapping those ions onto each other.

## 4.5 Results

### 4.5.1 The $Cr_8$ Molecule

#### 4.5.1.1 Magnetic Interactions

The $Cr_8$ molecule was optimised using the LDA, PBE and rSCAN XC functionals. All three functionals showed the antiferromagnetic arrangement to be the ground state of the molecule, which agrees with experiment and previous first-principles investigations [119]. Table 4.2 reveals the strength of the magnetic moments of the optimised $Cr_8$ structures. The magnetic moments in all three XC functionals orientate around $3\mu_B$, which are compatible with a spin $S_{\text{mag mo}}=\frac{3}{2}$, resulting from Hund's rule, with charge 3+ for each Cr ion. The total magnetism per formula unit vindicates this with a value of $24\mu_B$, corresponding to eight magnetic moments of $3\mu_B$. These values are in good agreement with previous DFT calculations performed using the PBE GGA and B3LYP hybrid XC functionals [119–121]. The

|  | Ion Species | AFM ($\mu_B$) | FM ($\mu_B$) |
|---|---|---|---|
| LDA | Cr | ± 2.83 | +2.98 |
| | O | ± 0.03 | -0.03 |
| PBE | Cr | ± 2.89 | +3.02 |
| | O | ± 0.03 | -0.02 |
| rSCAN | Cr | ± 2.94 | +3.05 |
| | O | ± 0.02 | -0.03 |

Table 4.2: The magnetic moments of the Cr ions and the residual magnetism on the O ions of the $Cr_8$ molecule in the antiferromagnetic and ferromagnetic states.

excellent agreement with previous, peer-reviewed magnetic moments is significant, as it provides confidence in the results.

Using the broken symmetry approach the effective exchange interaction parameter can be determined from the difference in final energies of the ferromagnetic and antiferromagnetic states. This method assumes the uniformity of interactions as it uses the isotropic Heisenberg model.

Considering only nearest neighbour Heisenberg exchange interactions between the Cr ions and in the absence of any anisotropy terms, the Hamiltonian is:

$$E^{\text{tot}} = J \sum_{i}^{7} S_i \cdot S_{i+1} + J S_8 \cdot S_1 \qquad (4.5.1)$$

where $S_i = S_{\text{mag mo}} = \frac{3}{2}$ for $i = 1, \cdots, 8$, which is the spin moment of the Cr atoms.

|  | Exchange Interaction Parameter (meV) |
|---|---|
| LDA | -6.4 |
| PBE | -5.2 |
| rSCAN | -4.7 |
| EXP. [123] | -1.5 |
| DFT (PBE) [119] | -5.8 |
| DFT (PBE) [120] | -6.3 |

Table 4.3: The exchange interaction parameters of the $Cr_8$ molecule, using the LDA, PBE and rSCAN XC functionals as well as comparison with experiment and other *ab-initio* calculations.

Therefore, the exchange interaction parameter is:

$$J = \frac{4}{9} \frac{E_{\text{FM}}^{\text{tot}} - E_{\text{AFM}}^{\text{tot}}}{16} \tag{4.5.2}$$

Whereby a negative exchange value indicates an antiferromagnetic interaction and a positive exchange value indicates a ferromagnetic interaction. Table 4.3 shows the exchange interaction parameters for the LDA, PBE and rSCAN XC functionals, using Equation 4.5.2. While there is a large discrepancy with experimental, by a factor of three and more, we observe good agreement with other DFT calculations, with a difference under 10%.

### 4.5.2 The $Cr_{10}$ Molecule

#### 4.5.2.1 Broken and Preserved Symmetry Optimisations

The highest symmetry of the $Cr_{10}$ molecule corresponds to the $D_5$ point group. However, this symmetry is not present in the experimental molecular structure, which is extracted from crystal structure data where the molecular symmetry is necessarily broken. Further, previous *ab-initio* works have not implemented $D_5$ symmetry but instead have used no symmetry within the molecule. Nevertheless, the justification for the $D_5$ point group is strong, so the absence of this symmetry within the molecule will be considered as breaking the symmetry of the molecule.

This section presents the results from a series of first-principle investigations pertaining to preserving and breaking the $D_5$ symmetry through geometry optimisations of the molecule to render information about the magnetic structure. The broken symmetry calculations implemented no ionic constraints, and so the optimisation was not constrained through symmetry enforcement. Not enforcing the same symmetry group within the optimisations will result in different molecular structures. So the comparison of these structures and magnetic information held within is not scientifically
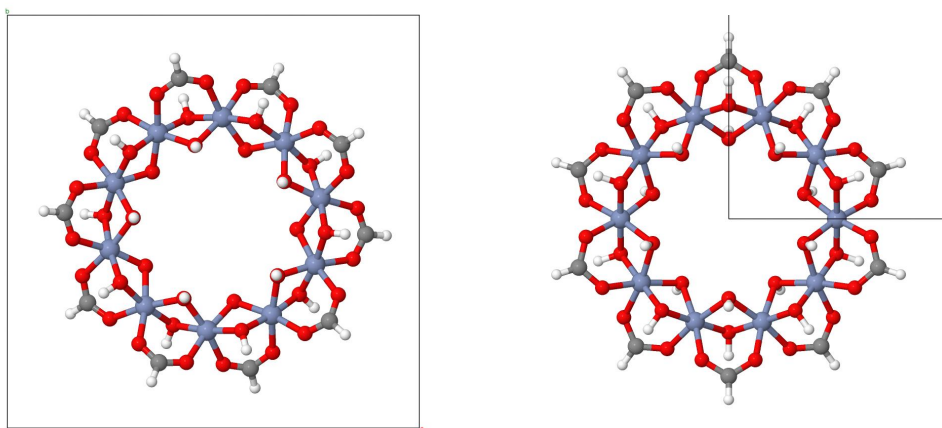
Figure 4.7: The $Cr_{10}$ molecule with $C_1$ symmetry aligned to the cubic cell (a) and the absolute position representation of the molecule with $D_5$ symmetry (b). Both (a) and (b) are cubic cells with a=21Å, b=21Å and c=21Å(10Å) (b).

sound, as this section will show.

While the optimisations preserved the $D_5$ symmetry through ionic constraints, different XC functionals will lead to slightly different structures due to different force representations. Therefore, comparing the ground state properties of these XC functionals is justifiable against experimental data but not against each other.

The optimisations used the LDA, PBE and rSCAN XC functionals to provide a comprehensive understanding of both the molecule and its representation provided by the XC functionals. The broken symmetry optimisations relate to the molecule aligned in a cubic unit cell, while the preserved symmetry optimisations existed fractionally within the unit cell to maintain the planar nature of the Cr ions, as seen in Figure 4.7. The molecular optimisations were performed for both the nearest neighbour antiferromagnetic and ferromagnetic co-linear configurations.

Of these two magnetic states, the ferromagnetic arrangement was the ground state of the molecule in all three XC functionals. The initial ferromagnetic and antiferromagnetic configurations were preserved throughout the geometry optimisations, which is essential for valid results.

(a)

| $D_5$ | AFM (eV) | FM (eV) | Difference (meV) |
|---|---|---|---|
| LDA | -44260.4484 | -44260.6208 | 172.4723 |
| PBE | -44302.3427 | -44302.5491 | 206.9976 |
| rSCAN | -44119.4785 | -44119.5945 | 116.0099 |

(b)

| $C_1$ | AFM (eV) | FM (eV) | Difference (meV) |
|---|---|---|---|
| LDA | -44267.4109 | -44267.4162 | 5.2405 |
| PBE | -44305.6979 | -44305.8038 | 109.9538 |
| rSCAN | -44125.6497 | -44125.7468 | 97.0907 |

Table 4.4: The ground state energies for the antiferromagnetic (AFM) and ferromagnetic (FM) arrangements. The energies are calculated from the separate optimisations of those two states with $D_5$ (a) and $C_1$(b) symmetry maintained through ionic constraints.

Tables 4.4a and 4.4b show that the ferromagnetic and antiferromagnetic states energetically differ by hundreds of meV. The difference between these states is typical of single molecular magnets, for instance, $Ni_4$, $Fe_6$ and Fi-binuclear [109]. However, the difference is significant enough to have comfortable assurance in the ferromagnetic ground state but small enough to understand the metastable antiferromagnetic configuration, experimentally perceived as a bistable state [106, 108].

Tables 4.4a and 4.4b show that the $C_1$ symmetry optimised to a lower ground state, which is expected as the optimisation process had more energetic pathways open to minimise the forces which the ionic constraints forbid. This is made clear in Tables 4.5a and 4.5b, where the $C_1$ optimisation broke the uniformity of the ring, with a substantial deviation from circularity. The unequal Cr-Cr distances within the molecule also compromise the integrity of the magnetic exchange pathways. By breaking the ring, the optimisation led to a lower energy ground state. We observe that with the linear constraints enforcing $D_5$ symmetry, the integrity of the ring is maintained as well as uniformity in the Cr-Cr distances. Tables 4.5a and 4.5b show that the two symmetry relaxations reached different bond

equilibriums and, therefore, different molecules.

(a)

| D$_5$ | Distance Measured | Minimum (Å) | Maximum (Å) |
|---|---|---|---|
| LDA | Cr-Cr | 3.279 | 3.279 |
| | Cr-O | 1.971 | 2.232 |
| | Centre dist. | 5.300 | 5.300 |
| PBE | Cr-Cr | 3.288 | 3.281 |
| | Cr-O | 2.011 | 2.233 |
| | Centre dist. | 5.305 | 5.305 |
| rSCAN | Cr-Cr | 3.281 | 3.281 |
| | Cr-O | 2.101 | 2.234 |
| | Centre dist. | 5.310 | 5.310 |

(b)

| C$_1$ | Distance Measured | Minimum (Å) | Maximum (Å) |
|---|---|---|---|
| LDA | Cr-Cr | 3.231 | 3.294 |
| | Cr-O | 1.794 | 1.945 |
| | Centre dist. | 5.191 | 5.233 |
| PBE | Cr-Cr | 3.211 | 3.251 |
| | Cr-O | 1.983 | 2.251 |
| | Centre dist. | 5.201 | 5.231 |
| rSCAN | Cr-Cr | 3.091 | 3.228 |
| | Cr-O | 1.891 | 2.223 |
| | Centre dist. | 5.165 | 5.291 |

Table 4.5: The minimum and maximum distances between the same Cr-Cr,  Cr-O ions as well as a measure of the circularity of the optimised D$_5$ (a) and C$_1$(b) Cr$_{10}$ molecule.

#### 4.5.2.2 Magnetic Interactions

The interactions between magnetic sites must obey the rules of super-exchange through the bridging oxygens, as seen in Figure 4.7. This assertion comes from no two magnetic sites possessing direct orbital overlap and is vindicated in the Mulliken analysis of both symmetries, see Tables 4.6a and 4.6b.

(a)

| $D_5$ | Ion Species | AFM ($\mu_B$) | FM ($\mu_B$) |
|---|---|---|---|
| LDA | Cr | ± 2.95 | +3.05 |
| | O | ± 0.04 | -0.03 |
| PBE | Cr | ± 3.05 | +3.08 |
| | O | ± 0.03 | -0.02 |
| rSCAN | Cr | ± 3.05 | +3.08 |
| | O | ± 0.03 | -0.02 |

(b)

| $C_1$ | Ion Species | AFM ($\mu_B$) | FM ($\mu_B$) |
|---|---|---|---|
| LDA | Cr | ± 2.81 | +2.87 |
| | O | ± 0.04 | -0.04 |
| PBE | Cr | ± 2.88 | +2.90 |
| | O | ± 0.04 | -0.02 |
| rSCAN | Cr | ± 2.93 | +3.01 |
| | O | ± 0.03 | -0.02 |

Table 4.6: The magnetic moments of the Cr magnetic sites and the bridging O ions for the antiferromagnetic (AFM) and ferromagnetic (FM) arrangements. The magnetic moments originate from the Mulliken analysis of the separate optimisations of those two states with $D_5$ (a) and $C_1$(b). Symmetry maintained through ionic constraints.

Both symmetry optimisations reveal similar magnetic site strength of around $3\mu_B$, with rSCAN producing the same or slightly stronger moments to PBE. From a spin-only view, the Cr (III) ions should possess a magnetic moment of $S_{\text{mag mo}} = \frac{3}{2}$, which is in line with Tables 4.6a and 4.6b. In the ferromagnetic arrangement, the spin-only representation correlates to a total magnetism of $S_{\text{tot}} = 15$, which is on-par with the $30\mu_B$ found for the total integrated spin density. This magnetic arrangement is concurrent with previous calculations [106], although it differs from experimental results

| XC-Functional | Symmetry | Exchange Interaction Parameter (meV) | McInnes *et al.*[108] (meV) | Sharmin *et al.*[106] (meV) |
|---|---|---|---|---|
| LDA | $C_1$ | 0.118 | | |
| | $D_5$ | 3.831 | | |
| PBE | $C_1$ | 2.353 | -0.5579 | 0.5084 |
| | $D_5$ | 4.587 | | |
| rSCAN | $C_1$ | 2.158 | | |
| | $D_5$ | 2.578 | | |

Table 4.7: The extracted exchange interaction parameter, determined from breaking the symmetry of the the optimised antiferromagnetic with a ferromagnetic arrangement. Here a negative value indicates an antiferromagnetic arrangement. Compared with the experimental result of McInnes [108] and a DFT result computed by McInnes for Sharmin [106].

determining $S_{\text{tot}}$=9, with two anti-parallel spins [106].

The ferromagnetic arrangement produces higher magnetic moments than the antiferromagnetic ones. This disparity is due to the larger residual magnetism on the Oxygen ions in the antiferromagnetic arrangement compared to the ferromagnetic.

Determination of the strength of these interaction comes from Equation 2.5.5. Only considering the nearest neighbour Heisenberg exchange interactions and no anisotropy, the Hamiltonian takes the form:

$$E^{\text{tot}} = J \sum_{i=1}^{9} S_i \cdot S_{i+1} + J S_{10} \cdot S_1 \qquad (4.5.3)$$

where $S_i = S_{\text{mag mo}} = \frac{3}{2}$ for $i = 1, \cdots, 9$, which is the spin moment of the Cr atoms, the exchange interaction parameter is :

$$J = \frac{4}{9} \frac{E^{\text{tot}}_{\text{FM}} - E^{\text{tot}}_{\text{AFM}}}{20} \qquad (4.5.4)$$

Table 4.7 shows positive exchange interaction parameters, indicating ferromagnetic exchange and a ferromagnetic arrangement. The broken symmetry exchange values are lower than the preserved symmetry and

closer to the experiment. However, little-to-no weight can be given to their meaning; as Table 4.5 shows, the uniformity of the ring is destroyed and therefore not an accurate representation of the $Cr_{10}$ molecule. The deviation between the broken and preserved symmetries are larger for the LDA and PBE functionals. From Table 4.5, we observe that these two XC functionals also have larger differences in structures. However, the preserved symmetry maintained the molecular ring and the uniformity of bond lengths for the exchange pathways, meaning more weight can be given to those exchange interaction values.

However, there is a large discrepancy compared to the experimental value obtained from susceptibility measurements [108], indicating weak antiferromagnetism. The difference highlights the sizeable final energy difference between the metastable antiferromagnetic state and the ferromagnetic ground state. The broken symmetry calculations had a significantly smaller final energy difference between the high symmetry and broken symmetry states, which is the reason for the small exchange interaction parameter.

DFT is known to overestimate the magnitude of the exchange interaction parameter. However, the size of the difference between the values is unlikely to be solely the result of the approximations within core DFT, suggesting that the molecule could be unsuitable for the Noodleman broken symmetry approach [46] , which relies upon the molecule conforming to the isotropic Heisenberg (Ising) model with "rigid" magnetic moments. Further reasons could be the level of approximation of the Noodleman approach; only nearest neighbour terms were considered, potentially indicating that next-nearest neighbours play a more vital role.

Addressing the significance of the difference between the exchange interaction parameter presented in this chapter and those of Sharmin *et al.* [106] comes to the point that the exchange interaction of Sharmin *et al.* originates from non-peer-reviewed DFT calculations performed by

McInnes; while useful for comparison, they are not necessarily more meaningful than the ones presented in this chapter.

The exchange interaction parameter presented by McInnes *et al.* [108] originates from the quantum chemistry approach using the diagonalisation of the Heisenberg Hamiltonian. The source of the discrepancy becomes clear upon consideration of the dimensionality of the diagonalisation. With ten magnetic sites, the number of magnetic interactions makes the dimensions of the Heisenberg model far too large to diagonalise (see Section 2.5.3.3 and Equation 4.5.5). Therefore, a reduced number of possible magnetic configurations were considered by McInnes *et al.*. Unfortunately, this reduction adds a level of discrepancy and uncertainty between their experimentally determined and our DFT determined exchange interaction parameters.

$$(2S_{\text{mag mo}} + 1)^N = (2 \times \frac{3}{2} + 1)^{10} = 1048576 \tag{4.5.5}$$

Where N is the number of coupled spins, and $S_{\text{mag mo}}$ the magnetic strength of the site.

Further differences between our DFT results and the experimental presented by Sharmin *et al.* [106] are found in the total ground state magnetism. The experimental value, determined by MPMS quantum design superconducting quantum interface device magnetometer, $S_{tot}$=18$\mu_B$ is significantly lower than our DFT value of $S_{tot}$=30$\mu_B$. Furthermore, Sharmin *et al.* indicate that their ground state arrangement has two anti-parallel spins to the other eight.

It could be the case that the $S_{tot}$=18$\mu_B$ and the $S_{tot}$=30$\mu_B$ states are energetically very close, meV in difference. This could explain the difficulty of the downhill solver in CASTEP to find the $S_{tot}$=18$\mu_B$, as the solver effectively sees a flat energy surface.

A method to converge various metastable spin configurations is to use

the fixed spin moments (FSM) [124] constraint on the DFT calculations. In the FSM scheme, the total number of electrons in the majority and minority spin channels are fixed. This essentially amounts to imposing an effective external magnetic field, which introduces a difference in the Fermi-energies for the majority and minority spin channels.

As a result of the inconsistencies brought forward by the optimisation of the $C_1$ broken symmetry, the rest of the sections will only pertain to the calculations for the $D_5$ symmetry enforcement.

The FSM scheme relates the total spin, $S_{tot}$, to the total energy, E, which can be plotted to show the effect changing the total magnetism of the system has on the final energy [109, 124, 125].

Figure 4.8 shows the converged energies for the ground state and meta-stable states corresponding to the total magnetism of $S_{tot}=0\mu_B$ ,$6\mu_B$ ,$18\mu_B$ ,$24\mu_B$, and $30\mu_B$, which relates to antiferromagnetic, four-spins anti-parallel, two spins anti-parallel, one spin anti-parallel and ferromagnetic arrangements.

Figure 4.8a shows that the LDA XC functional maps a linear relationship between the decreasing total magnetism and the increasing total energy. There is a difference between the $S_{tot}=30\mu_B$ and $S_{tot}=18\mu_B$ of around 50meV, with the $S_{tot}=30\mu_B$ state as the definitive ground state. The difference in energies of all the different magnetic states comes from the different orientations of the magnetic moments, and the linearity results from the direct effect it has on the energy.
With the removal of $S=6\mu_B$, this linear behaviour propagates through to the PBE functional, in Figure 4.8b. However, the $S=6\mu_B$ is more energetically unfavourable than the antiferromagnetic arrangement. An investigation into the HOMO-LUMO gap would indicate if it is necessary to include additional Zeeman energy to stabilise this artificial configuration. However, the PBE functional still confirms the $S_{tot}=30\mu_B$ ferromagnetic configuration as the ground state.
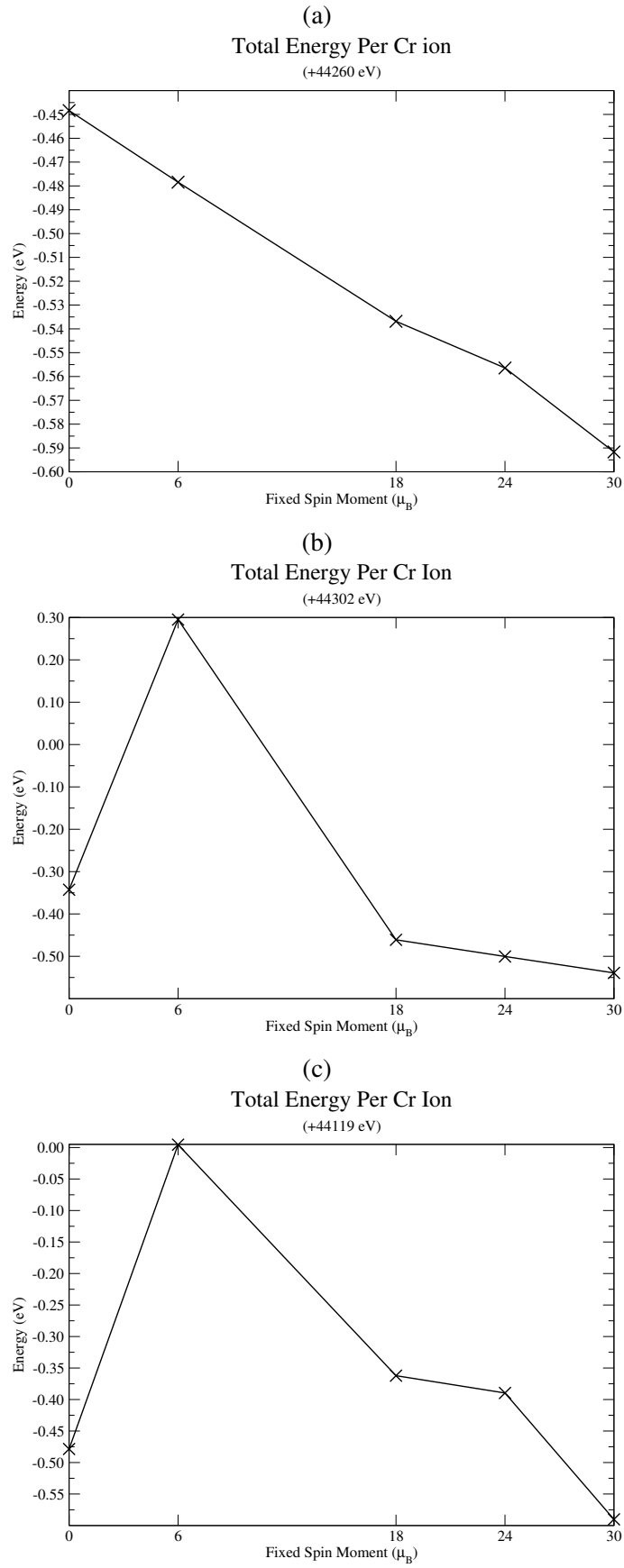
Figure 4.8: The Fixed Spin Moment energy difference between varying magnetic configurations for the LDA (a), PBE (b) and rSCAN (c) XC-functionals. Calculations performed within the imposed $D_5$ symmetry. The energy displayed is the difference in the total energy for the total spin and the FSM=$30\mu_B$.

The rSCAN functional shows no overall linearity between the different magnetic arrangements. Whereby the $S_{tot}=6\mu_B$, $18\mu_B$ and $24\mu_B$ is higher in total energies than the antiferromagnetic arrangement. This shows that there is no longer a direct relationship between changing the total spin and the final energy of the system. In addition to the implications mentioned for PBE, the breakdown in linearity indicates the potential for the frustrated next-nearest neighbours interaction as more influential in the molecule.

All three XC functionals, under the FSM constraint show that the $S_{tot}=30\mu_B$ ferromagnetic configuration is the ground state of the molecule, with meV differences between the experimental $S_{tot}=18\mu_B$ ground state.

In trying to understand the higher energy states exhibited by rSCAN in Figure 4.8, we observe that the $D_5$ symmetry has been imposed within the molecule through ionic constraints, and the magnetic arrangements with total magnetism of $S_{tot}=6\mu_B$, $18\mu_B$ and $24\mu_B$ break the imposed magnetic symmetry. The only surviving symmetry within the molecule is the $C_2$ symmetry. This is a lower symmetry and would be energetically more favourable than the $D_5$. Therefore, this reduced symmetry is not a direct cause of the higher energies of these unfavourable states.

The exchange interaction parameter can provide useful insights into the break from linearity using the PBE and rSCAN functionals. However, the overall numerical energy difference does not allow for a unique exchange interaction parameter. Thus, only an estimate of the order of magnitude for the exchange interaction parameter can be made through the nearest neighbour Heisenberg model.

Table 4.8 shows the exchange interaction parameters from varying the total magnetism within the FSM scheme. For the LDA functional, which exhibits a linear relationship between the total magnetism and the final energy, the order of magnitude for the exchange interaction parameter is around 0.7meV-3.8meV. These values vary in the same linear fashion as seen in Figure 4.8. The nearest neighbour Heisenberg exchange interac-

| XC functional | $S_{tot}=0\mu_B$ (meV) | $S_{tot}=24\mu_B$ (meV) | $S_{tot}=18\mu_B$ (meV) | $S_{tot}=6\mu_B$ (meV) |
|---|---|---|---|---|
| LDA | 3.831 | 0.677 | 1.189 | 2.516 |
| PBE | 4.587 | 0.863 | 1.736 | 18.540 |
| rSCAN | 2.578 | 4.451 | 5.068 | 13.236 |

Table 4.8: The extracted exchange interaction parameters for the variety of magnetic configurations for the fixed spin moment. These values pertain to the $D_5$ optimised molecule.

tion show a good agreement with the experimental value from Sharmin *et al.* [106]

For the PBE functional, with the $S_{tot}=6\mu_B$ excluded, the magnitude of the exchange interaction parameter is around 0.8meV-4.5meV. These values are also in agreement with the experimentally determined exchange values and exhibit the same linearity expressed in the LDA functional. However, the $S_{tot}=6\mu_B$ state does not conform to the linear relationship, and the reason for the increased final energy must come from the interactions within the molecule, indicating that the frustration of the next nearest neighbours is more significant in this state as there are more frustrated moments.

Figure 4.8c and Table 4.8 reveal the complete breakdown of the rigid Heisenberg model to describe the magnetic exchange interactions for the rSCAN functional. This meta-GGA XC functional describes the interaction between electrons more comprehensively than PBE by including the orbital kinetic energy and the isoorbital indicator [27, 28]. This greater representation highlights the two main limitations of the nearest neighbour Heisenberg model. The first is not including next-nearest neighbour interactions, which are frustrated as $\frac{10}{2} = 5$. The second is the Ising-like moments the model uses; as the molecule could have wave excitations that are commensurate with the length of the ring.

The disparity between the experiment and the DFT results in Table 4.7 can be related, in part, to the significance of optimisation, indicating that

the molecule possesses a complex energy surface, as partially observed in Figure 4.8. Magnetic properties are highly susceptible to slight differences in molecular structures. While the DFT result presented by McInnes in Sharmin *et al.* [106] shows weak ferromagnetism, the difference in magnitude between our results is visible. This can result from the next-nearest neighbour frustration, which we have not accommodated in the Heisenberg model. There could also be spin canting from wave excitations within the system, explaining the difficulty in mapping the Heisenberg exchange interactions to experiment.
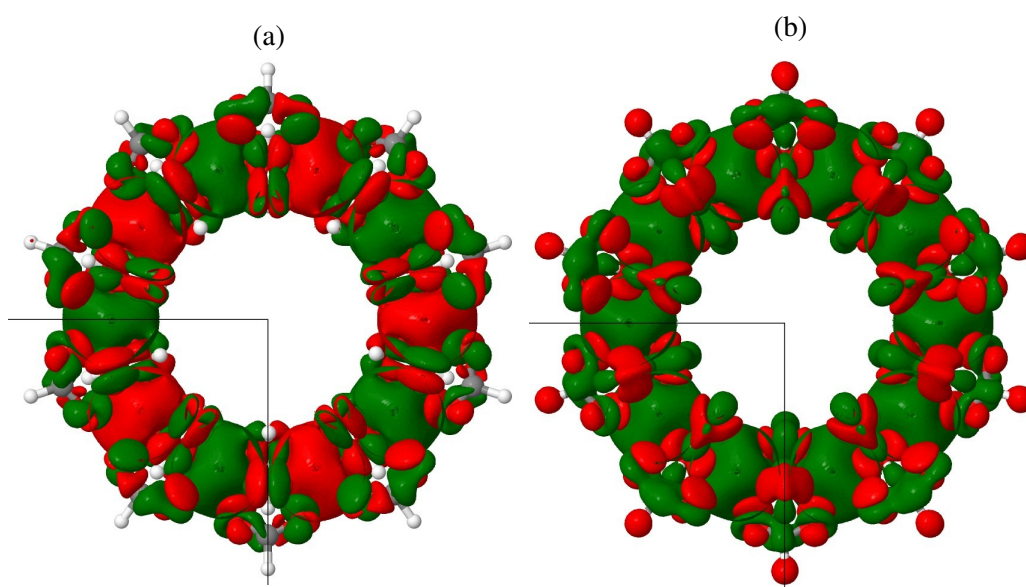


Figure 4.9: The Fixed Spin Moment spin density for the AFM (S=0$\mu_B$) (a) and FM (S=30$\mu_B$) (b) states for the rSCAN XC-functional. Whereby red isosurfaces represent spin down densities and green isosurfaces represent spin up densities.

The isosurfaces representing the spin density throughout the different magnetic states provide insights into the extent of the influence of the frustrated next-nearest neighbour interactions. Figure 4.9 reveals the spin density for the ferromagnetic (Figure 4.9b) and antiferromagnetic (Figure 4.9a) states for the rSCAN functional. There was no significant difference between spin densities of the LDA and PBE functionals for these states, so only rSCAN has been displayed (See Appendix C for the LDA and PBE XC
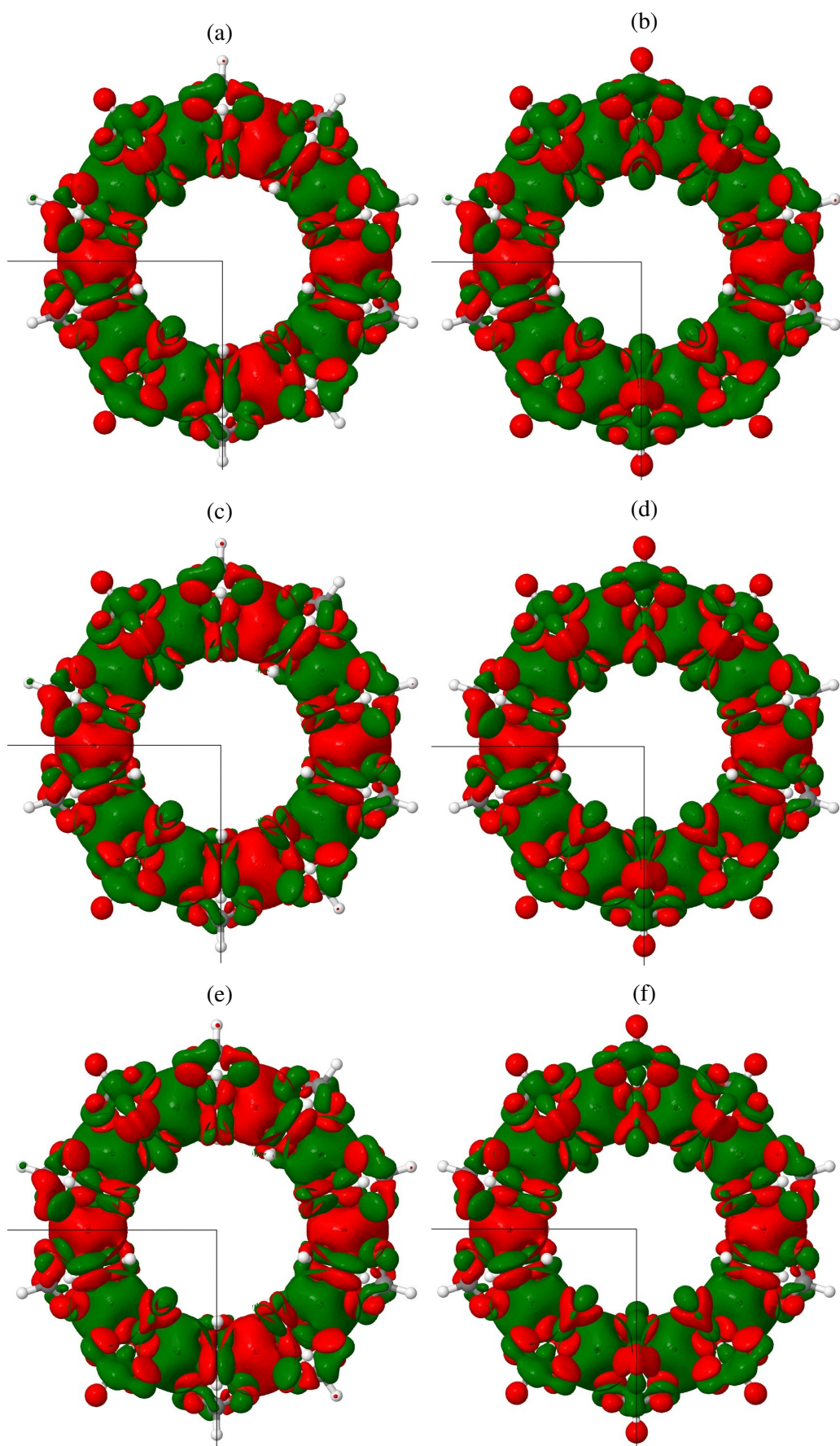
Figure 4.10: The Fixed Spin Moment spin density between the S=6$\mu_B$ (a, c and e) and S=18$\mu_B$ (b, d and f) states for the LDA (a,b), PBE (c,d) and rSCAN (e,f) XC-functionals. Whereby red isosurfaces represent spin down densities and green isosurfaces represent spin up densities.

(a)

(b)

(c)
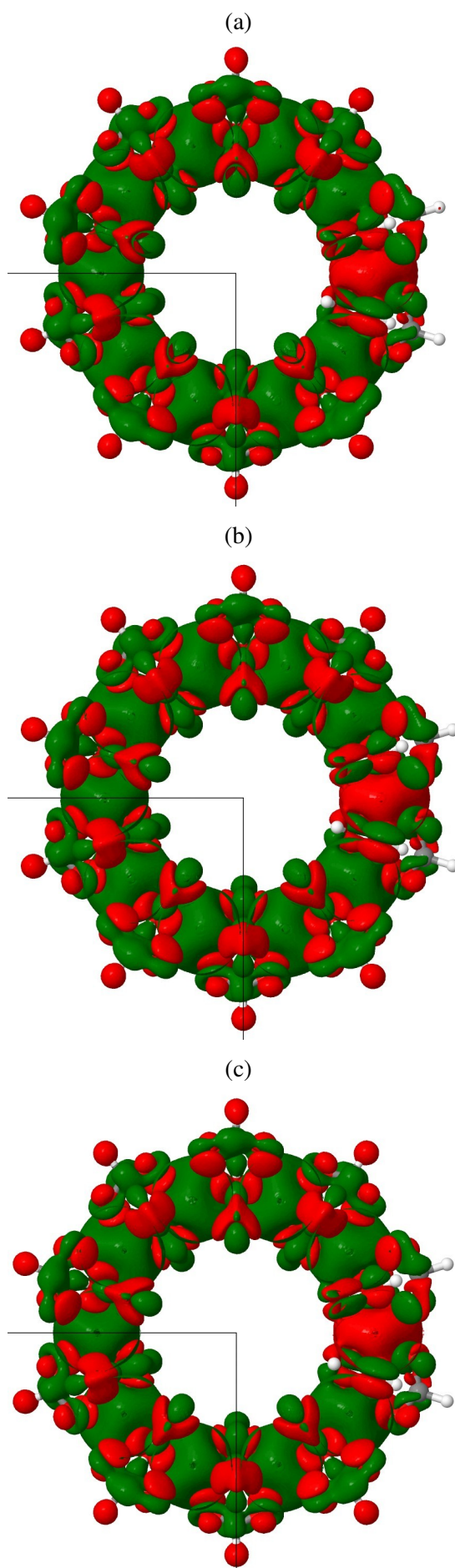
Figure 4.11: The Fixed Spin Moment spin density for the S=24$\mu_B$ state for the LDA (a), PBE (b) and rSCAN (c) XC-functionals. Whereby red isosurfaces represent spin down densities and green isosurfaces represent spin up densities.

functionals). From Figure 4.9, there is strict adherence to the $D_5$ symmetry throughout the magnetic exchanges within the molecule. In addition, the number of exchange pathways for each Cr ion is six, with three on either side, indicating that the exterior bond (O-CH-O) plays a more vital role in the magnetic interactions.

Further differences between these states are the magnetisation of the Hydrogens, which in the unsaturated molecule would be the methyl groups. This magnetisation is present in the ferromagnetic states but disappears in the antiferromagnetic states, except for a small spin density on the outer Hydrogen above the x-axis on the left-hand side. The magnitude of the spin density on the Hydrogen in the antiferromagnetic state is small enough not to appear on the Mulliken analysis. In comparison, the Hydrogens in the ferromagnetic state possessed a minute but notable magnitude of $0.01\mu_B$. This magnetisation value is comparable – and found to be exact in magnitude– to that on the inner Oxygens, which take part as one of the three exchange interactions between magnetic sites.

Figure 4.8 indicated that the LDA XC functional would adhere to the dominance of the nearest neighbour interactions, Figures 4.10a, 4.10b and 4.11a show this through the uniformity of the exchange pathways in the spin density isosurfaces. There are no distinguishable differences between comparable exchange interactions through $S_{tot}=6\mu_B$-$24\mu_B$. For instance, the antiferromagnetic exchanges that intersect the x-axis are comparable and show no differences. Figures 4.10c, 4.10d and 4.11b show the PBE XC functionals spin density and reveal minor differences in the exchanges between S=$6\mu_B$ and $18\mu_B$/$24\mu_B$. The most conspicuous is the minor magnetisation of the Hydrogen located above the x-axis on the left-hand side of Figure 4.10c. While this magnetisation is small at $0.008\mu_B$, it accentuates the differences in spin-down density on the Oxygen atom, appearing to be not as dominant in the bond (immediately below the Hydrogen (Figures 4.10c and 4.10d)).

Further, the elliptical-shaped spin densities (both spin channels) around the inner Oxygens (underneath the visible Hydrogen) are not as pronounced in Figure 4.10c as in Figure 4.10d, indicating fewer spin carriers in this region. The elliptical-shaped spin-up density differences do not occur in the LDA XC functional and signify that the semi-local exchange in PBE for the $S_{\text{tot}}=6\mu_B$ state potentially detects the effects of the next-nearest neighbour frustration and spin canting causing a reduction in the spin density of that exchange pathway. In Figure 4.10d, the two ferromagnetic sites encapsulated by the unit cell (bottom left) show slight exchange differences on the inner Oxygens and Hydrogens when compared with Figure 4.10c. This is a slight reduction in the dominance of spin-down carriers in the region; the only difference is the next-nearest neighbour, providing further weight that these interactions are significant within the molecule.

Figure 4.8 shows that the rSCAN XC functional detects the effects of the frustrated next-nearest neighbour for each magnetic state as there are changes in the spin density isosurfaces. However, there are little differences between the $S_{\text{tot}}=18\mu_B$ and $S_{\text{tot}}=24\mu_B$ states as the final energy difference between these states is significantly small. Therefore, we expect to see the same or qualitatively indistinguishable level of spin canting and deviation of spin-densities within the exchange pathways. Figures 4.10e, 4.10f and 4.11 reveal the same but more pronounced differences in exchange pathways observed in the PBE XC functional. This is expected as both functionals predict $S=6\mu_B$ at a higher final energy in Figure 4.8, so similar spin-densities are expected.

Comparing Figure 4.10e and 4.10f with 4.10c and 4.10d, we observe a more substantial presence of spin-down carriers on the top left, outer, Oxygen-Carbon bond above the x-axis. This characteristic is repeated, on the same bond, throughout the molecule. Comparing the inner Oxygen ion to the right of the visible y-axis between Figure 4.10e and 4.10c, we observe a subtle increase in the spin-down channel with rSCAN.

105

Equation 2.2.16 shows the contributing factors to the Kohn-Sham total energy. Out of those contributors, the XC energy adds a few per cent to the total energy, so the changes to the spin densities should be small to demonstrate the effects of the next-nearest neighbour frustration on the exchange pathways and spin moments.

### 4.5.2.3 Magnetostriction

Using different synthesis methods, McInnes *et al.* [108] showed that a difference in distance of 7mÅ between the Cr ions was enough to go from weak antiferromagnetism to weak ferromagnetism. This magnetic sensitivity to bond-length [108] suggests an intrinsic relationship between magnetic energy and mechanical energy: magnetostriction.

With the molecule starting in the antiferromagnetic configuration, which is not unrealistic as experimentally demonstrated by McInnes [108] and shown as a legitimate potential-well through the FSM calculations of Figure 4.8, an external magnetic field, through reaching a suitable strength, would force the magnetic moments to align parallel to it. When the external magnetic field is aligned along the z-xis, all magnetic moments are either parallel or anti-parallel and, through increasing the strength of the external field, all moments are parallel. This final magnetic configuration is ferromagnetic.

Through two separate relaxations of the molecule in both the ferromagnetic and antiferromagnetic arrangements, the difference in those relaxed $Cr_{10}$ molecules can be, to an introductory level, categorised through magnetostriction. The model employed by the first-principles calculations was the co-linear spin DFT, whereby the magnetic moments behave like the Ising model. This, therefore, means that no anisotropy is considered as no spin-orbit coupling was included in the calculations. A complete picture of magnetostriction depends upon the magnetocrystalline anisotropy energy (MAE) [109, 126–128], which is not compatible with the imposed model.

| XC-functional | Magnetostrictive force (meV/Å) |
|---|---|
| LDA | 2.015 |
| PBE | 2.331 |
| rSCAN | 1.315 |

Table 4.9: The magnetostrictive forces for the different XC-functionals between two Cr ions.

Only a rudimentary indication of magnetostriction can be granted through a magnetostrictive force.

Magnetostriction, typically, is documented through the magnetostriction coefficient, which is defined through directions concerning the unit cell [109, 126–130]. This format depends on the use of relativistic spin-orbit coupling. A more fundamental way to measure magnetostriction within molecules is the differences in molecular structure through bond-lengths and atomic distances by applying an external magnetic field. In addition, a magnetostrictive force provides insight into potential magnetostrictive changes.

Table 4.9 reveals the magnetostrictive force present in the LDA, PBE and rSCAN XC functionals. The magnitude of these forces is relatively small compared to atomic force tolerance in geometry optimisation. The PBE functional exhibits the most significant magnetostrictive force, with rSCAN producing the least. This difference is most likely a consequence of the previously mentioned functionals ability to represent the magnetic exchange interactions. However, it is not certain that this is the definitive source, and further investigations into magnetic anisotropy are required.

## 4.6 Discussion

The purpose of the investigation into the $Cr_8$ molecule was not to provide new insights but to use it as a benchmark for the $Cr_{10}$ investigation. Thus, the comparison with $Cr_{10}$ begins with the use of crystal symmetry to maintain the ring, highlighting the necessity of ionic constraints. The further comparison comes from the exchange interaction parameter, which is closer to the experiment for $Cr_8$ than $Cr_{10}$. The extent of the overestimation of the exchange interaction parameter between the two comes from what is different about the molecules. The main difference originates from the number of magnetic ions in each ring, which changes the number of next-nearest neighbour interactions. Fundamentally the $Cr_8$ molecule does not experience frustration through these interactions as $\frac{8}{2} = 4$. However, the $Cr_{10}$ molecule does experience a frustrated next-nearest neighbour interaction as $\frac{10}{2} = 5$. This frustration plays an influencing factor in the difference between the exchange interaction parameters and the magnetic moments.

Further, there are key magnetic differences between the $Cr_{10}$ and $Cr_8$ ground states. For example, the $Cr_8$ ring converges into an antiferromagnetic ground state, while the $Cr_{10}$ ring has a ferromagnetic ground state. The exchange interaction parameters are larger than experiment. However, even if they were closer to experiment, it would be surprising if the super-exchange interaction was due to tail overlap integrals. It is possible the length of the ring could have an impact on the super-exchange as there are differences between the optimised bonds of $Cr_8$ and $Cr_{10}$. Also, the exchange paths between the molecules are different, $Cr_{10}$ just has O ($2s^2\ 2p^4$) and C ($2s^2\ 2p^2$) ions , while $Cr_8$ also contains F ($2s^2\ 2p^5$) ions. Therefore further calculations would be needed to understand their full implications and to provide a definitive answer.

The first-principles investigation into the unusual molecular magnetic, $Cr_{10}$, has revealed confidence with implementing ionic constraints to en-

force a higher symmetry. In combination with Hydrogen saturation, this symmetry significantly reduced the computational cost of the calculations and stabilised the molecule in the relaxation process, made visible through a reduced number of iterations. Furthermore, enforcing the higher symmetry allowed for the continuity of the relaxed structure for each respective XC functional, which was essential for more detailed insights into the magnetic interactions within the molecule. The deviation of the magnetic moments from $3\mu_B$ within the broken symmetry calculations highlight this point (see Table 4.6b).

The effective exchange interaction parameter was extracted using the isotropic nearest-neighbour Heisenberg model. Unfortunately, this model used was insufficient to comprehensively capture the magnetic behaviour in the molecule based on the discrepancy between our DFT results, the experimental and previous DFT results. For instance, we did not include the frustrated next-nearest neighbour interaction, which affected the magnetic exchange pathways as seen in the spin density isosurfaces. Further, we did not include relativistic terms to the Hamiltonian to investigating any wave excitations through non-co-linear DFT calculations. Due to the limited number of terms included in the Heisenberg model, only the magnitude of the exchange interaction parameter can be used, which correctly predicted ferromagnetism.
However, when comparing with the experimentally extracted values of the exchange interaction parameter, it is essential to note that it is not a physical observable; therefore, approximations will be introduced. The method employed by McInnes [108] was to compute the exchange interaction using a small subset of the larger possible magnetic interactions. While this method is computationally more straightforward, it becomes unclear which interactions are chosen. This adds an additional element of uncertainty to the result and, in part, aids the explanation behind the discrepancy.

In combination with the spin density isosurfaces, the FSM scheme re-

veals the significant influence of the frustrated next-nearest neighbour interactions on the exchange pathways. The LDA XC functional does not detect the frustrated next-nearest neighbours. The reasoning behind this is due to the LDA XC hole. The XC hole is how the electron density within a region reacts to another electron placed anywhere in space [131]. The LDA XC hole is spherical and does not react to densities that are fast changing as it is only local. The spherical nature of the LDA XC hole would prevent it from modelling the subtle differences in the spin density isosurfaces, which requires an inhomogeneous XC hole [132]. Further, the local nature of the exchange would prevent any detection of the influence of the frustrated next-nearest neighbour interactions.

The XC hole reasoning can extend to the GGAs, specifically the numerical GGA hole created by Perdew *et al.* [22], which produced the analytic PBE XC functional. It has been shown that for the GGA in the local density environment, exchange dominates correlation [132]. This is because the cutoff radius for the exchange hole becomes smaller when the change in density gradient tends to infinity—in turn, forcing the exchange hole to become deeper and more localised [22]. The contribution from correlation, however, slowly goes to zero. The GGA exchange energy is more negative, leading to lower energies than LDA [132], as seen in Tables 4.4a and 4.4b. The meta-GGA, rSCAN, detected the differences in the exchange pathways caused by the frustrated next-nearest neighbour interactions because of the increased ability to model types of bonds through the isoorbital indicator, which can switch to various local approximations of exchange and correlation energies for the appropriate bonding type [27, 28]; providing a more complete picture of the bonds.

The frustration of the next-nearest neighbour interaction within the molecule indicates unsuitability for the employed Heisenberg model, which only concerned nearest neighbour interactions. More terms can be added to the Heisenberg Hamiltonian to include the next-nearest neighbour interactions. However, further investigations would be needed so that an accurate char-

acterisation of the impact of the frustrated nearest-neighbours can be made.

The magnetostrictive force present in the molecule can only be used as a rough indication of magnetostriction within the molecule. Magnetostriction depends upon models to include anisotropy, not exchange anisotropy but relating spin to the crystal structure: spin-orbit coupling. However, this force is likely to become larger upon the inclusion of relativistic effects. Further investigations would be needed to determine the extent of magnetostriction within the molecule.

One further aspect of the $C_{10}$ ring to consider when understanding the differences between the work presented in this chapter and experiment is the potential for non-co-linear wave excitations whose wavelength is commensurate with the ring. Our calculations used co-linear spin-polarised DFT, which cannot account for wave excitations, therefore to fully understand the magnetic characteristics of $Cr_{10}$, non-co-linear magnetism and the use of wave excitations software would be needed.

Within this chapter we have compared the rSCAN XC functional to other XC functionals and found further insights into the $Cr_{10}$ SMM. However, there have been similarities, such as the ground state total magnetism of the molecule. This consistency is not unique to the chromium based molecular magnets as researched by Yamamoto *et al.* [133] who found that SCAN and rSCAN reached the same ground state total magnetism in $Mn_{12}$, $Fe_4$, $Ni_4$ and $Co_4$ as with the respective literature [133–137].

## 4.7   Conclusion

In conclusion, the complex magnetic phenomena exhibited by the single molecular magnet, $Cr_{10}$, requires further investigation to attribute the actual cause of the bistable phenomena. Initial ab-initio results reveal that the molecule possesses a complex energy landscape with two potential wells

competing for the ground state. While the ferromagnetic state is lower in ground state energy, the antiferromagnetic arrangement is still a stable convergence. The magnetic moments on the Chromium ions orientates around $3\mu_B$, with the PBE and rSCAN functionals converging on the same values.

The ionic constraints enforced the $D_5$ symmetry, which assisted with stabilising the convergence for the geometry optimisations and allowed for the integrity of the ring to be maintained. The higher symmetry played a crucial role in determining the finer detailed magnetism, which $C_1$ failed to exhibit. In addition, the Hydrogen saturation significantly reduced the computational cost of the first-principle calculations and allowed for a wide variety of previously inaccessible magnetic configurations.

The exchange interaction parameters for the LDA, PBE and rSCAN XC functionals overestimated the strength of ferromagnetism compared to the experiment. We attribute this to an insufficient number of terms included in the Heisenberg model, nearest neighbour interactions and Ising spin moments, which fail to capture of the affects of the frustrated next-nearest neighbour interactions. In addition, through the fixed spin moment DFT constraint, in conjunction with the spin-density isosurfaces, the molecule displays significant next-nearest neighbour interactions.

The effect of the frustrated next-nearest neighbour interaction is only fully present in the rSCAN functional; we believe this to be, in part, the shape of the XC holes of LDA and PBE. However, further investigation would be required to have complete confidence in this hypothesis.

A rudimentary approximation of magnetostriction inside the molecule is provided through a magnetostrictive force. However, this is only an estimation as anisotropy through spin-orbit coupling is required to gain a complete picture of magnetostriction.

The $Cr_8$ molecule successfully supported the $Cr_{10}$ investigation by pro-

viding insight into the frustrated next-nearest neighbour interaction of $Cr_{10}$ and applying confidence to the methodology of extracting the exchange interaction parameter.

## 4.8   Future Works

Fully understanding the authenticity and source of magnetic properties initially shown in these first-principle calculations would require a more thorough investigation into the Heisenberg model. These future investigations should include non-co-linear spin polarised DFT calculations to model and detect any spin canting or wave excitations commensurate with the length of the ring. Further, the addition of the next-nearest neighbour term into the Heisenberg Hamiltonian will increase agreement with experiment and should be investigated.

The magnetostriction force requires further calculations, involving finely converged calculations involving spin-orbit coupling, to include the magnetic anisotropy. This would better grasp the extent of magnetostriction within the molecule, as indicated by the magnetostriction force.

# Chapter 5

# The Iron Pnictide Superconductors

## 5.1 Introduction

The new class of high-temperature superconductors first discovered in LaOFeAs sparked a great deal of interest in the Fe-based pnictides [138–141]. Experiments have revealed crucial differences in the underlying mechanism from the earlier cuprate superconductors. The superconductivity of the cuprates originates from Mott insulator physics; however, the superconductivity of the iron-based pnictides come from an instability of the Fe d-band electrons, producing a spin density wave [139, 142–145]. These superconductors share a common motif of a Fe-pnictogen in the middle, with two layers acting as either spacers or charge donors/ acceptors [146]. The experimental and theoretical research conducted over the years indicates that the FeAs layers are the focal point for understanding their superconductivity. [143, 147–149].

The magnetic ground state of iron arsenide is unquestionably antiferromagnetic. However, the magnetic properties of the metallic antiferromagnet are not fully understood. The initial magnetic investigation using powder neutron diffraction in 1972 showed that the material contained a simple incommensurate spin spiral with a wave-vector of $q_s$=0.375 and with the moments laying in the ab-plane [150]. However, this result was disputed through transport experiments, revealing highly anisotropic magnetic properties, whereby susceptibility differed significantly between the a and b planes [151]. Mössbauer measurements [152] combined with single-crystal neutron diffraction [153] confirmed this anisotropy.

Of the iron pnictides, the PbO-type FeSe is superconductive below $T_c$=8K, making it an area of intense research [154–158]. The superconductivity within this material is highly tunable; for instance, under 8.9GPa of applied pressure, $T_c$ increases to a maximum value of 36.7K [159]. Furthermore, FeSe has a complex structure profile, with a structural transition between a tetragonal *P4/nmm* and an orthorhombic *Cmma* crystal structure [160]. This transition is shown in pressure and resistivity against temperature experiments by Sun *et al.* [161] and Kasahara *et al.* [162], respectively. Further, X-ray diffraction performed by Margadonna *et al.* [160] demonstrates this transition through lattice constant. Unlike other iron-based superconductors, the structural transition in FeSe is not accompanied by long-range striped antiferromagnetic ordering [163]. However, magnetism still plays a vital role in iron selenide. Wang *et al.* [164, 165] used neutron scattering experiments and revealed the presence of local spin fluctuations in the tetragonal and orthorhombic states, suggesting a close-lying magnetic phase.

The first-principles investigation into FeAs by Parker and Mazin [145] cemented the antiferromagnetic ground state magnetic ordering and revealed that, unlike other Fe-based superconductors, it could not be explained by Fermi surface nesting. They, however, found that the three-dimensional Fermi surface was consistent with the experimentally reported anisotropic magnetic behaviour. Later, Griffin and Spaldin [146] investigated the effect of the exchange-correlation functional on the calculated structure and magnetic properties of the MnP-type structure. They concluded that the LDA performs poorly with the structural calculations and all functionals overestimate the Fe magnetic moments by a factor of 2. They further concluded that only the hybrid GGA provides structural values closest to the experiment. However, a negative Hubbard-U calculation would most likely reproduce the spin spiral as it would increase competition between the ferromagnetic and antiferromagnetic states. Next, Frawley *et al.* [166] performed DFT calculations, combined with experiment, on a vari-

ety of antiferromagnetic configurations to quantify the relative energies of different antiferromagnetic states and showed that the origin of the spin canting effect could be accounted for by spin-orbit coupling.

The shape of the Fermi surface and the electronic structure of tetragonal phase FeSe has been the focal points of many *ab initio* investigations. For instance, the investigations by Ma *et al.* [167] and Subedi *et al.* [168] have accurately captured the band dispersions above 90K, allowing for a good description of the localised electron and hole pockets forming the Fermi surface. However, comparing with ARPES measurements [169], the DFT calculations overestimate the energy scale of the band dispersions. The maxima of the hole pockets and minima of the electron pockets are hundreds of meV from the Fermi level [170], leaving a rough discrepancy of $\pm50$meV with experiment [171]. This difference is partly responsible for DFT calculations predicting a Fermi surface with three hole pockets at the centre of the Brillouin zone instead of the two experimentally observed [171].

In this chapter, our investigation centres on the ambition to employ the XC functional rSCAN, with its regularised isoorbital indicator [27, 28], to try and gain further insight into the complex bond-dependant magnetism [166] of FeAs. Further ambitions relate to determining if a difference can be observed in the intricate band structure around the Fermi level. Finally, we also investigate the Fermi surface in FeSe with the rSCAN functional to see if there are any improvements to the number of hole pockets and the distance of their maxima with respect to the Fermi level [167–171].

## 5.2 Crystal Structure

### 5.2.1 FeAs

Bulk FeAs crystalises into the orthorhombic MnP-type structure, as seen in Figure 5.1. The primitive unit cell consists of eight atoms with distorted $FeAs_6$ octahedra, face-sharing along the a-axis and edge-sharing along the b- and c-axes. The empirically determined space group is a disputed point. In 1969, Selte *et al.* [150, 172] using X-ray diffraction (and later neutron diffraction), performed the first experimental characterisation of the structure and magnetic properties reporting *Pnma* symmetry with the MnP structure. However, Lyman and Prewitt [173] proposed, through comparison of both symmetries via X-ray diffraction, that the structure belongs to the space group $Pna2_1$. The next addition came from Rodriguez *et al.* [153], who performed powder and single-crystal neutron diffraction experiments and favoured the *Pnma* symmetry.

Iron arsenide has similar Fe-Fe affinities found in the layered Fe-based superconductors; LaFeAsO, $BeFe_2As_2$ and NaFeAs [166]. However, the critical difference is in the six octahedra As ions surrounding the Fe ions
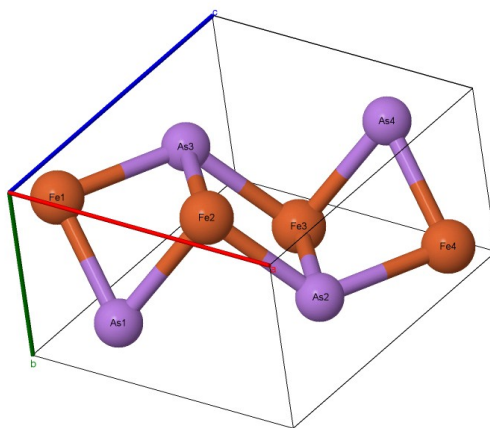


Figure 5.1: A visual representation of the FeAs crystal structure contained within the unit cell. The atoms are labelled and the a, b, c axes follow red, green, blue colouring respectively.

instead of the four tetrahedral As ions. The Fe ions are positioned at the *4c* Wyckoff sites, producing the following four locations in the unit cell, Fe1 at $(x, \frac{1}{4}, z)$, Fe2 at $(\bar{x} + \frac{1}{2}, \frac{3}{4}, z + \frac{1}{2})$, Fe3 at $(\bar{x}, \frac{3}{4}, \bar{z})$ and Fe4 at $(x + \frac{1}{4}, \frac{1}{4}, \bar{z} + \frac{1}{2})$ [153] where x = 0.004 and z=0.199 [166].

First principles calculations in 2017 by Griffin and Spaldin [146] revealed a *Pnma* crystal symmetry as the ground state structure through the relaxation of the crystal. This symmetry was quickly confirmed in the same year by first-principles and experimental results from Frawley *et al.* [166].

Due to the consistency in the determined symmetry of experimental and *ab initio* results, the *Pnma* symmetry with MnP-type structure was selected as the starting ionic configuration, as seen in Figure 5.1.

### 5.2.2 FeSe

The bulk tetragonal phase of FeSe consists of a 2-D Fe ion plane, bonded to Se ions and forming a quasi 2-D layer crystal structure (see Figure 5.2). The Se ions are above and below the Fe planes, and a single unit cell consists of two Fe ions and two Se ions. The stacks contain edge-sharing $FeSe_4$ tetrahedral with a packing motif almost identical to the FeAs layers. Our first-principles investigation will use the supercell approximation with a size of $\sqrt{2}$ a $\times$ $\sqrt{2}$ a $\times$ c. This size will allow us to model the antiferromagnetic planes effectively.
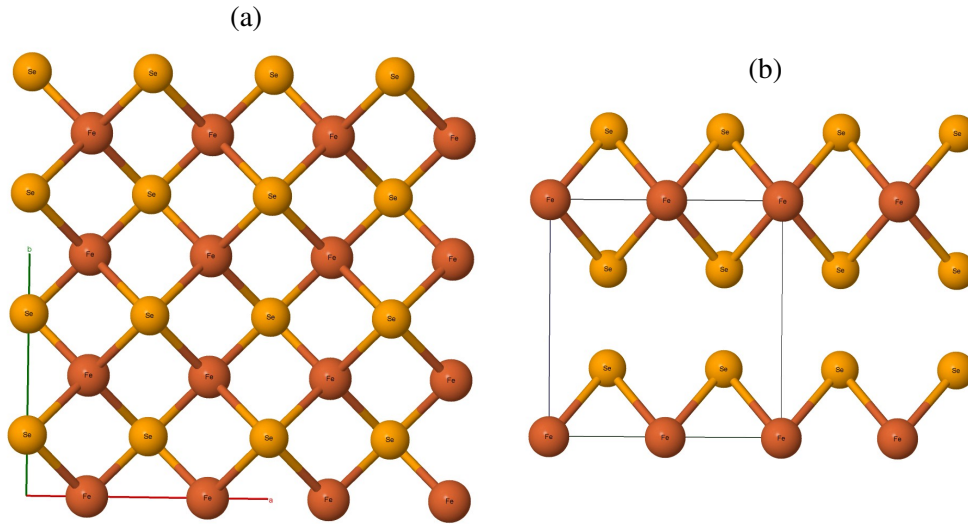
Figure 5.2: A visual representation of the FeSe tetragonal phase structure with *P4/nmm* symmetry. With the top view (a) and a side view (b) demonstrating the 2-D planes. Whereby the a, b, c axes are represented by red, green, blue respectively.

## 5.3 Magnetic Structure

### 5.3.1 FeAs

As previously mentioned, the magnetic ground state of iron arsenide is antiferromagnetic. However, there is a complexity associated with the magnetic configurations; many different meta-stable magnetic states exist. These meta-stable states are energetically close enough for excitations to reach, resulting in spin density waves. The spin density wave produced by the material is a subject of intense research, as its characteristics are highly debated [150–153]. This investigation will not focus on the spin density wave but observe the different antiferromagnetic arrangements within the unit cell. These configurations are outlined and investigated by Frawley *et al.* [166] and concern the iron sites which have parallel spins: Fe1 || Fe3 (AFM1), Fe1 || Fe4 (AFM2) and Fe1 || Fe2 (AFM3), as seen in Figure 5.3. The calculations performed centred on co-linear AFM ordering, with nearest neighbours antiferromagnetically coupled and next-nearest neighbours

ferromagnetically coupled.



(a)

(b)

(c)
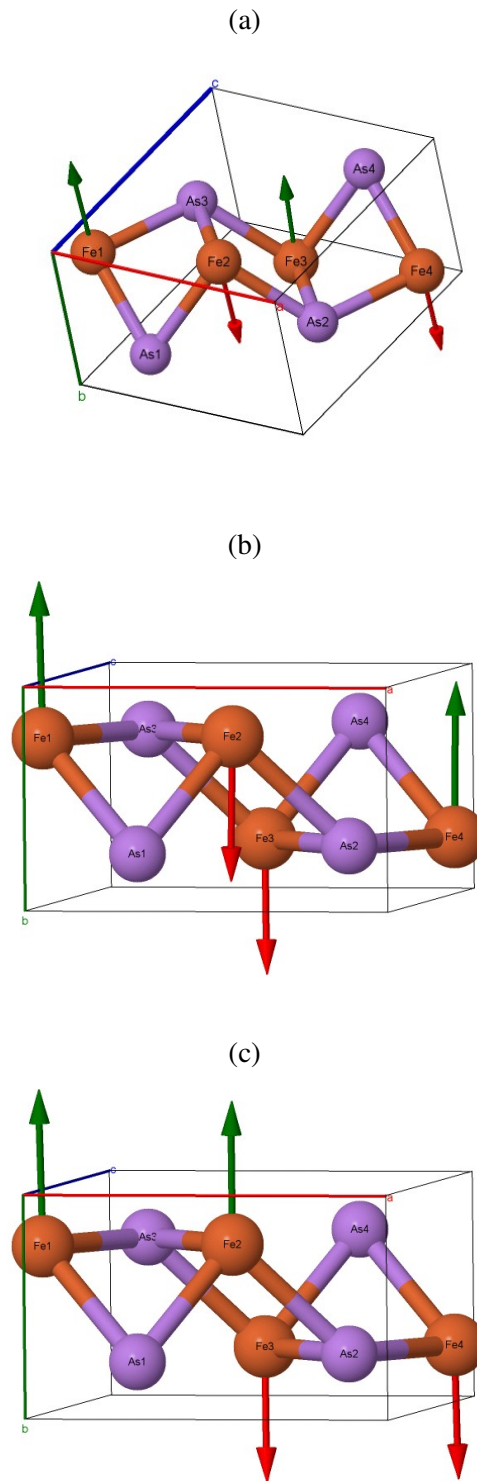
Figure 5.3: A visual representation of the magnetic configurations, AFM1 (a), AFM2 (b) and AFM3 (c). Whereby the a, b, c axes are represented by red, green, blue respectively. The size and direction of the moments are for visualisation only and are not to scale.

### 5.3.2 FeSe

The magnetic ground state for FeSe is significantly more debated than FeAs. Wang *et al.* [165] showed, through inelastic neutron scattering, that there is no long-range magnetic ordering. They further show that FeSe is an $S_{tot}=1$ nematic quantum-disordered paramagnet between the Néel and stripe magnetic instabilities. Baum *et al.* [174] showed, through Raman scattering (as a function of temperature and polarisation), that FeSe exhibits stripe-like antiferromagnetism; they further suggest that this ordering will be frustrated. Our first-principles investigation will use spin polarised co-linear DFT for the antiferromagnetic tetragonal phase of FeSe. The antiferromagnetic arrangement is such that each 2-D plane is antiferromagnetic (along the a-axis in Figure 5.2).

## 5.4 Results

### 5.4.1 Geometric Optimisations

#### 5.4.1.1 FeAs

For investigating the most appropriate symmetry of the material, a series of geometry optimisations used the LDA, PBE and rSCAN XC functionals with the *Pnma* symmetry imposed and symmetry switched off, with no enforced symmetry constraints. The *Pnma* symmetry with MnP-type structure propagates through all three XC functionals, including the relaxations for the different antiferromagnetic configurations (AFM1, AFM2 and AFM3), ferromagnetic and the zero spin configuration. This result is consistent with both experiments and other *ab initio* geometric optimisations. [146, 166, 172].

Table 5.1a shows a comparison of our results with experimental and

(a)

|  | Vol. (Å$^3$) | a (Å) | b (Å) | c (Å) |
|---|---|---|---|---|
| LDA | 100.63 | 5.203 | 3.318 | 5.828 |
| PBE | 108.36 | 5.450 | 3.290 | 6.042 |
| rSCAN | 112.45 | 5.521 | 3.345 | 6.089 |
| X-ray [172] | 110.64 | 5.442 | 3.373 | 6.028 |
| ND [150] | 110.37 | 5.437 | 3.370 | 6.023 |
| PND [153] | 109.52 | 5.456 | 3.323 | 6.031 |
| LDA [146] | 100.33 | 5.313 | 3.194 | 5.912 |
| GGA [146] | 108.45 | 5.469 | 3.277 | 6.051 |
| HSE [146] | 108.41 | 5.470 | 3.276 | 6.050 |

(b)

|  | Fe ($x$) | Fe ($z$) | As ($x$) | As($z$) |
|---|---|---|---|---|
| LDA | 0.0028 | 0.2017 | 0.1990 | 0.5801 |
| PBE | 0.0012 | 0.2013 | 0.2002 | 0.5736 |
| rSCAN | 0.0046 | 0.2033 | 0.2068 | 0.5746 |
| X-ray [172] | 0.0027 | 0.1994 | 0.1992 | 0.5773 |
| ND [150] | 0.0063 | 0.1975 | 0.2018 | 0.5789 |
| LDA [146] | 0.0020 | 0.2020 | 0.2000 | 0.5730 |
| GGA [146] | 0.0020 | 0.2020 | 0.2010 | 0.5730 |
| HSE [146] | 0.0020 | 0.2020 | 0.2010 | 0.5730 |

(c)

|  | Fe-Fe (a) (Å) | Fe-Fe (b) (Å) | Fe-As (1) (Å) | Fe-As (2) (Å) |
|---|---|---|---|---|
| LDA | 2.662 | 2.877 | 2.280 | 2.431 |
| PBE | 2.788 | 2.937 | 2.334 | 2.497 |
| rSCAN | 2.818 | 2.988 | 2.359 | 2.520 |
| X-ray [172] | 2.789 | 2.937 | 2.347 | 2.517 |
| LDA [146] | 2.725 | 2.867 | 2.281 | 2.428 |
| GGA [146] | 2.796 | 2.941 | 2.338 | 2.496 |
| HSE [146] | 2.797 | 2.938 | 2.358 | 2.519 |

Table 5.1: Lattice parameters (a) , atomic fractional coordinates (b) and bond-lengths (c) obtained from relaxations in the LDA, PBE and rSCAN XC functionals. Compared to experimental X-ray [172], neutron diffraction (ND) [150] and powdered neutron diffraction (PND) [153] data and to the DFT data determined by Griffin *et al.*[146]. Where the (a) and (b) bonds are the shortest bonds (Figure 5.3) between the Fe ions in the a-direction and the b-direction, likewise with the Fe-As columns.

DFT calculations performed by Griffin *et al.* [146]. The comparison reveals that LDA optimisation underestimates the experimental volumes by around 9%. This difference is larger than the standard LDA underestimation but appears to align with previous DFT calculations [146]. The PBE functional agrees better with experiments by underestimating the unit cell volume roughly between 0.8%(PND)-2%(X-ray). It is usual for PBE to overestimate lattice parameters; however, it has underestimated them with iron arsenide. This divergence from expectation of the PBE functional for iron arsenide is documented through other DFT calculations [146], and our underestimation is on par with those values .

The rSCAN functional was the only functional we used which overestimated the volume of the unit cell. Compared to all experimental data in Table 5.1a, it overestimates both the a and c lattice parameters; however, it slightly underestimates the b lattice parameter. The PBE functional also shares a slight underestimation of this lattice parameter. This two-out-of-three overestimation leads to an rSCAN global volume overestimation between 1.64%(X-ray)-2.68%(PND).

We have determined the shortest and longest distances between the Fe ions in the a lattice parameter direction and the b lattice parameter direction. These values correspond to the Fe1-Fe2 and Fe2-Fe3 distances, see Table 5.1c. The LDA functional vastly underestimates the experimental distances but overall agrees with the DFT determined lengths [146]. On the other hand, the GGA, PBE, strongly agrees with the experimentally determined values with a discrepancy of 0.001 Å and coincides with previous DFT findings [146]. Comparing with experimental values, the rSCAN functional overestimates these distances by around 1%. The overestimation of these distances is expected as the a and b lattice parameters are also overestimated.

### 5.4.1.2 FeSe

Table 5.2 compares the lattice parameters for the optimised tetragonal phase FeSe with X-ray scattering and other DFT calculations using GGA. The LDA functional underestimates the a and c lattice parameters by over 10%, which is a similar result to other iron pnictides (see Section 5.4.1.1). This performance continues to the positioning of the Se ions z-coordinate, which disagrees with experiment by around 22%.

The PBE functional agrees well with experiment and other GGA calculations, underestimating the lattice parameter a by less than 1%. The functional overestimates the lattice parameter, c, by around 0.5% which is a larger discrepancy than the a parameter but still excellent agreement. The fractional coordinate of the Se ion differs by around 6.5% with both the experimental positioning and other GGA calculations.

The optimised lattice parameters from using the rSCAN functional are in good agreement with experimental values. The lattice parameter, a, is closer to experiment than the PBE functional, with an underestimation of around 0.05%. For the c lattice parameter, the rSCAN functional underestimates the experimental length by around 1.5%, which is more than the PBE functional. The z coordinate of the Se ions are very close to experiment with a difference of around 1%. This is a 5% improvement over PBE.

| | a (Å) | c (Å) | $z_{Se}$ |
|---|---|---|---|
| LDA | 3.372 | 5.356 | 0.214 |
| PBE | 3.766 | 5.551 | 0.250 |
| rSCAN | 3.769 | 5.436 | 0.270 |
| X-ray [163] | 3.771 | 5.521 | 0.267 |
| Synchrotron X-ray [160] | 3.774 | 5.525 | - |
| DFT (GGA) [171] | 3.765 | 5.518 | 0.241 |

Table 5.2: A comparison of the lattice parameters and atomic z- fractional coordinates of Se for the FeSe tetragonal structure. Values obtained from relaxations in the PBE and rSCAN XC functionals. Compared to experimental X-ray [160, 163] data and to the DFT data determined by Watson *et al.* [171].

### 5.4.2 Magnetic properties

#### 5.4.2.1 FeAs

We used spin-polarised co-linear DFT, as this investigation did not progress to include the spin density wave. As a result, the exchange interactions were not determined due to a large amount of magnetic anisotropy within the system. Furthermore, previous DFT calculations have revealed a linear energy dependence on the spin magnitude, which is incompatible with the Heisenberg and Ising models [166]. Therefore, this section highlights the fundamental magnetic properties available through non-relativistic co-linear spin-polarised calculations.

Table 5.4 reveals the magnetic moments located on the iron ions and any residual magnetism on the arsenide ions. The magnetic moments show that the magnetism within iron arsenide depends heavily on the choice of XC functional. For instance, LDA converges to a non-magnetic configuration for all three antiferromagnetic states, revealing the unsuitability of this XC functional to represent this material accurately. This behaviour propagates to the PBE functional, which exhibits significantly reduced magnetic moments on the Fe ions and predicting localised moments instead of the experimentally determined itinerancy [151].

| XC-Functional | Ion Species | AFM1 ($\mu_B$) | AFM2 ($\mu_B$) | AFM3 ($\mu_B$) |
|---|---|---|---|---|
| LDA | Fe | $\pm 0.00$ | $\pm 0.00$ | $\pm 0.00$ |
| | As | $\pm 0.00$ | $\pm 0.00$ | $\pm 0.00$ |
| PBE | Fe | $\pm 1.20$ | $\pm 0.63$ | $\pm 0.93$ |
| | As | $\pm 0.00$ | $\pm 0.00$ | $\pm 0.00$ |
| rSCAN | Fe | $\pm 2.30$ | $\pm 2.43$ | $\pm 2.27$ |
| | As | $\pm 0.03$ | $\pm 0.06$ | $\pm 0.00$ |

Table 5.3: The magnetic moments of the Fe magnetic sites and the As exchange ions for the antiferromagnetic states, AFM1, AFM2 and AFM3. The magnetic moments originate from the Mulliken analysis of the separate optimisations.

However, the magnetic moments of the PBE functional on the Fe ions appear to be in agreement with the DFT calculations performed by Frawley *et al.* [166], acknowledging minor differences most likely due to the geometric optimisation.

The rSCAN functional provides a larger magnetic moment on the iron ions and predicts itinerancy with residual magnetism on the arsenide ions. rSCAN only predicts itinerancy for the AFM1 and AFM2 states, indicating that the number of antiferromagnetic aligned spins plays a role in the spin density around the arsenide ions.

### 5.4.2.2 FeSe

This investigation did not focus on the highly debated spin density wave; therefore, we did not include anisotropy terms through non-co-linear magnetism. For that reason, we have not determined exchange interaction parameters for the FeSe 2D planes.

The LDA functional shows a larger magnetic moment than other LDA *ab initio* calculations with a difference of $0.6\mu_B$. There is also a residual magnetic moment on the Se ions of $0.06\mu_B$; while this is a small magnetic moment, it is noticeable. The strength of the residual magnetic moment on the Se ions is identical for PBE and rSCAN functionals. The PBE and

| XC-Functional | Ion Species | Magnetic Moment ($\mu_B$) |
|:---:|:---:|:---:|
| LDA | Fe | $\pm 1.83$ |
| | Se | $\pm 0.06$ |
| PBE | Fe | $\pm 2.29$ |
| | Se | $\pm 0.06$ |
| rSCAN | Fe | $\pm 2.36$ |
| | Se | $\pm 0.06$ |
| DFT (LDA) [168] | Fe | $\pm 1.20$ |
| | Se | - |

Table 5.4: The magnetic moments of the Fe magnetic sites and the Se exchange ions for the antiferromagnetic state. The magnetic moments originate from the Mulliken analysis of the separate optimisations.

rSCAN functionals have a larger magnetic moment on the Fe ions, with a bigger moment from the meta-GGA. The difference in the size of the magnetic moment between functionals indicates the strong dependence of the magnetic properties with the functional used. This feature is expected among the mono iron pnictides [146].

### 5.4.3   Electronic Band Structure

#### 5.4.3.1   FeAs

This section explores the electronic band structure for the AFM1 state rendered through the different XC functionals; as shown in the previous section, LDA converges to a non-magnetic state and will, therefore, not be included.

We investigated two paths through the Brillouin zone; these relate to the paths taken by previous DFT calculations [146] and the path suggested by the python module SeeK-path [98, 99], which obtains and visualises band-paths through the Brillouin zone. The two paths through the Brillouin zone are; $\Gamma - X - S - \Gamma - \Delta - D - \Gamma$ and $\Gamma - X - S - Y - \Gamma - Z - U - R - T - Z$ , respectively. The AFM1 magnetic configuration will be shown in this section because it is the ground state magnetic arrangement and appears most frequently in literature [145, 146, 166].Therefore, offering more comparisons to evaluate the results of this investigation.

The electronic band structure of iron arsenide is of particular importance as there have been many hypotheses relating the bands around the Fermi-level to the observed spin density wave. Such hypotheses include Fermi pockets and Fermi surface nesting [145, 146]; both, of which are determinable through the electronic band structure and are subject to heated debate.

Figure 5.4 reveals the PBE XC functionals rendered band structure

127
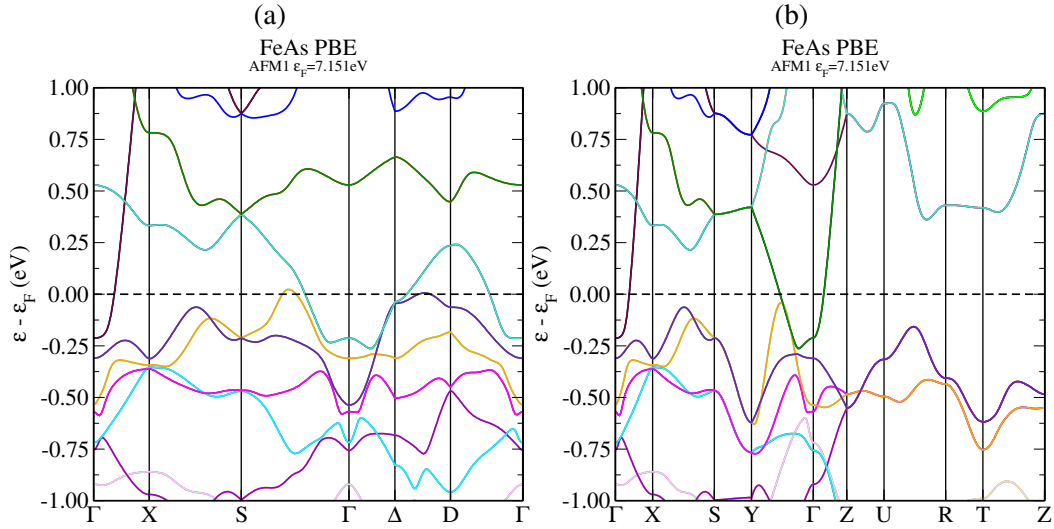
Figure 5.4: The Band structure of FeAs with the PBE functional and Gaussian smearing with default width 0.2eV.The difference between (a) and (b) are the different paths through the Brillouin zone.

through different Brillouin zone paths. A band structure to compare with literature [146] (Figure 5.4a ) and one recommended by SeeK-Path (Figure 5.4b) [98, 99].

The band structure in Figure 5.4a shows good agreement with Griffin *et al.* [146], with respect to the position of the band maxima and minima around the Fermi-level. However, the magnitude of those extrema possesses a significant discrepancy of approximately 25%. Understanding the source of this discrepancy is essential as it questions the legitimacy of the other path through the Brillouin zone. The difference is not significant enough to be accounted for in the minor positional differences. If it were a matter caused by the positions of the ions, we would expect the band structure to look significantly different. Therefore, the source of the difference does not exist in structural variations but the computation of the band structure.

The shape of first-principle band structure calculations rely on how well converged the k-point sampling grids are, and the orbital occupations used to determine the Fermi-level [175, 176]. Unfortunately, this aspect be-

comes evident in the iron arsenide band structure, which is extremely sensitive to the smearing scheme and broadening.

Figures 5.5a-5.5b show the difference in reducing the density of the k-point grid on the band structure; particular attention goes to the bands crossing the Fermi-level as they correspond to the higher-order Fourier components and are most susceptible to sampling. Reducing the density of the MP k-point grid from 25×27×21 to 10×10×10 did not appear to have any significant, if any difference, on the electronic band structure of the material.
The lack of change in the bands suggests that the k-point are efficiently converged enough to represent the wave functions and occupations accurately. The immutability between k-point grids is most likely a direct cause of the high smearing width of 0.2eV used in the Gaussian smearing scheme, allowing for a smaller k-point grid to converge: see Section 2.3.3.2 for more information. This hypothesis is confirmed upon reducing the smearing width from 0.2eV to 0.05eV, in Figure 5.5c.

We observe a significant reduction in the Fermi-energy of 51meV, which highlights the importance the smearing width plays in the occupation of states and, subsequently, the iterative determination of the Fermi-energy. We see a similar size shift in the conduction and valance bands up, which is expected from reducing the smearing width and lowering the Fermi-energy. The significant impact which the smearing scheme has on the band structures indicates that a different scheme is required. The Gaussian scheme suffers from the unphysical nature of its smearing width; however, the cold smearing scheme does not.

Figures 5.6a and 5.6b show the band structure through the cold smearing scheme with a sufficiently dense MP k-point grid of 33×35×31, with a spacing of 0.001 Å$^{-1}$, providing confidence in the sampling accuracy without oversampling creating step-like bands. We observe a reduction in the Fermi-energy, which is expected through the cold smearing scheme [34];
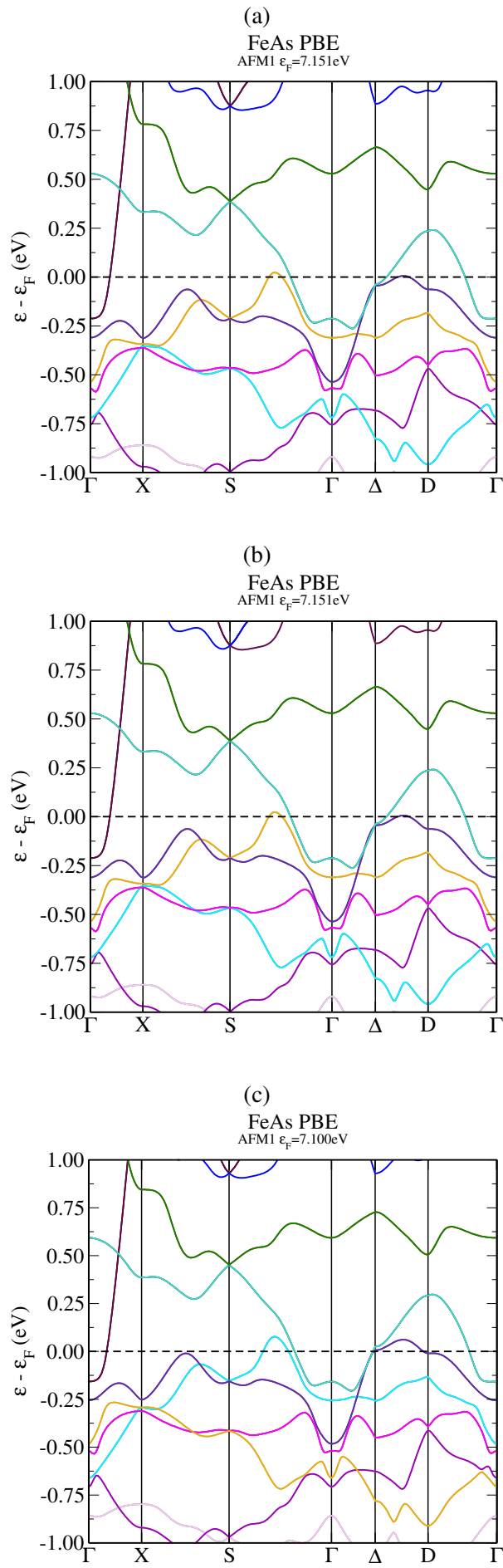
Figure 5.5: The PBE functional BS using Gaussian smearing, width 0.2eV for (a), (b) and 0.05eV for (c). A 25×27×21 k-point grid used in (a) and a 10×10×10 grid used for (b) and (c).
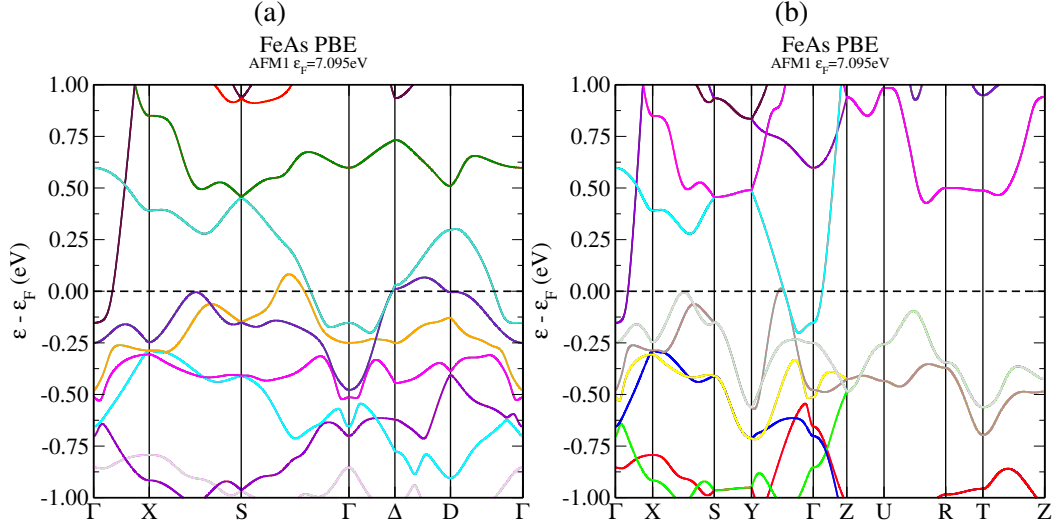
Figure 5.6: The Band structure of FeAs with the PBE functional using the cold smearing scheme with smearing width 0.02525eV. The MP k-point grid was $33\times35\times31$ with a path spacing of $0.001\text{Å}^{-1}$. The differences between (a) and (b) are different paths through the Brillouin zone.

Figure 5.6a shows excellent agreement with Griffin *et al.* [146], the Fermi pockets are easily seen, and the positions and magnitudes of the band maxima and minima align. There are minor band changes between the cold smearing and the Gaussian (Figure 5.5c), such as the bands around the Fermi-energy in the direction of $\Delta$ to D, whereby the valance bands have shifted up. This slight change results from the shift in Fermi-energies between the Gaussian and cold smearing schemes, which is ultimately affected by the occupation of states.

Figure 5.6a reveals a large electron pocket and two smaller hole pockets in the direction S-$\Gamma$-$\Delta$-D. The larger size of the electron pocket at the $\Gamma$ point compared to the two hole pockets in the S-$\Gamma$ and $\Delta$-D directions indicate that electrons are the main carriers with fewer hole carriers.

The band structure in Figure 5.6a overal agrees with the experimental Fermi surface from Campbell *et al.* [177], who used de Haas Van Alphen oscillations to determine the extreme regions of the Fermi surface. The de Haas Fermi surface consists of an electron pocket at the $\Gamma$ point and

four identical, symmetrically orientated hole pockets. The PBE functional describes the main edifice of this Fermi surface; the electron pocket at the $\Gamma$ point and the hole pockets around it (S-$\Gamma$ and $\Delta$-D directions), of course, a 2-D representation of the 3-D reciprocal space cannot determine if it is two hole pockets or four (two sets of two identical) hole pockets made to look like two due to the 2-D representation. The PBE functional does fail to get the shape of the hole pockets, which are described as roughly ellipsoidal. Specifically, the hole pocket in the $\Delta$-D direction is not ellipsoidal and breaks the identical nature of the hole pockets. Further, the size of the pockets agrees with Griffin *et al.* [146], which Campbell *et al.* [177] remark as larger than their de Haas pockets.

Figure 5.6b shows the path suggested by Seek-Path [98, 99], and in the direction of $\Gamma$-X-S, we observe the same bands as in Figure 5.6a, which is a mark of confidence that two independent calculations converge to the exact occupancies in the same directions. In the direction Y-$\Gamma$, there is a slight band crossing the Fermi-level from the valance bands. Assurance of this crossing comes from analysing the number of k-points that form the band above the Fermi-level. The k-point spacing is set to 0.001 Å$^{-1}$, which provides 60 k-points to form that band above the Fermi-energy. Upon comparison to a slightly less dense spacing of 0.02 Å$^{-1}$ (denser than the CASTEP default 0.1 Å$^{-1}$), which provides only five k-points above the Fermi-level, we see the conviction of the accuracy in the band crossing. The number of bands crossing the Fermi-level orientates around the $\Gamma$ point in the Brillouin zone, indicating localised metallic properties and the ability for the electrons to become excited and take part in conduction and spin density waves in the Y-$\Gamma$ and S-$\Gamma$-$\Delta$-D directions.

Comparing Figure 5.6b with the de Haas Fermi surface from Campbell *et al.* [177], the electron pocket is still present at the $\Gamma$ point with the same conduction band forming the pocket (the $\Delta$-$\Gamma$ direction in Figure 5.6a), made clear from the same characteristics of the conduction band in

Figure 5.6a in the direction Γ-X-S. However, the valance band is not the same, made clear from the difference in the characteristics of the bands in the Γ-X-S direction.

Figures 5.7a and 5.7b reveals the electronic band structure generated through the rSCAN XC functional in the cold smearing scheme with a broadening of 0.02525eV (293K).

The central aspect of Figures 5.7a and 5.7b is the change in how far the valance and conduction bands cross the Fermi-level, by only slightly crossing, it raises questions as to the legitimacy of the occupation of the conduction bands. Further doubts come from Figure 5.7b, which shows a band gap below the Fermi-level, adding to the concerns about the positioning of the Fermi-level itself. As with the PBE functional, the k-point grid is sufficiently dense to allow for adequate sampling, with a spacing of 0.001 $Å^{-1}$ between k-points and a 33×35×31 MP grid. Therefore, the investigation turned to determine the reliability of the positioning of the Fermi-level; see Section 2.3.3.1 for more detail on how CASTEP iteratively finds the Fermi-energy.

In order to test the actual value of the Fermi-energy, the electronic density of states code, OPTADOS [95, 96], was used as it interacted with CASTEP output files. OPTADOS focuses on the density of states, requiring a denser sampling of the Brillouin zone. This sampling is, therefore, better than CASTEP's band structure sampling as it would be denser. Further, to test the location of the Fermi-level, OPTADOS used both a grid and path sampling of the Brillouin zone in an independent Fermi-energy calculation. In both DOS calculations, OPTADOS determined the Fermi-energy 55meV lower than CASTEP, at 6.189eV. Thus, the accuracy of this value comes from both sampling types providing the same Fermi-energy. Applying the new Fermi-energy to Figure 5.7b moved the Fermi-level into the band gap. This positioning was confirmed through a higher verbosity output in CASTEP which revealed the conduction band occupan-
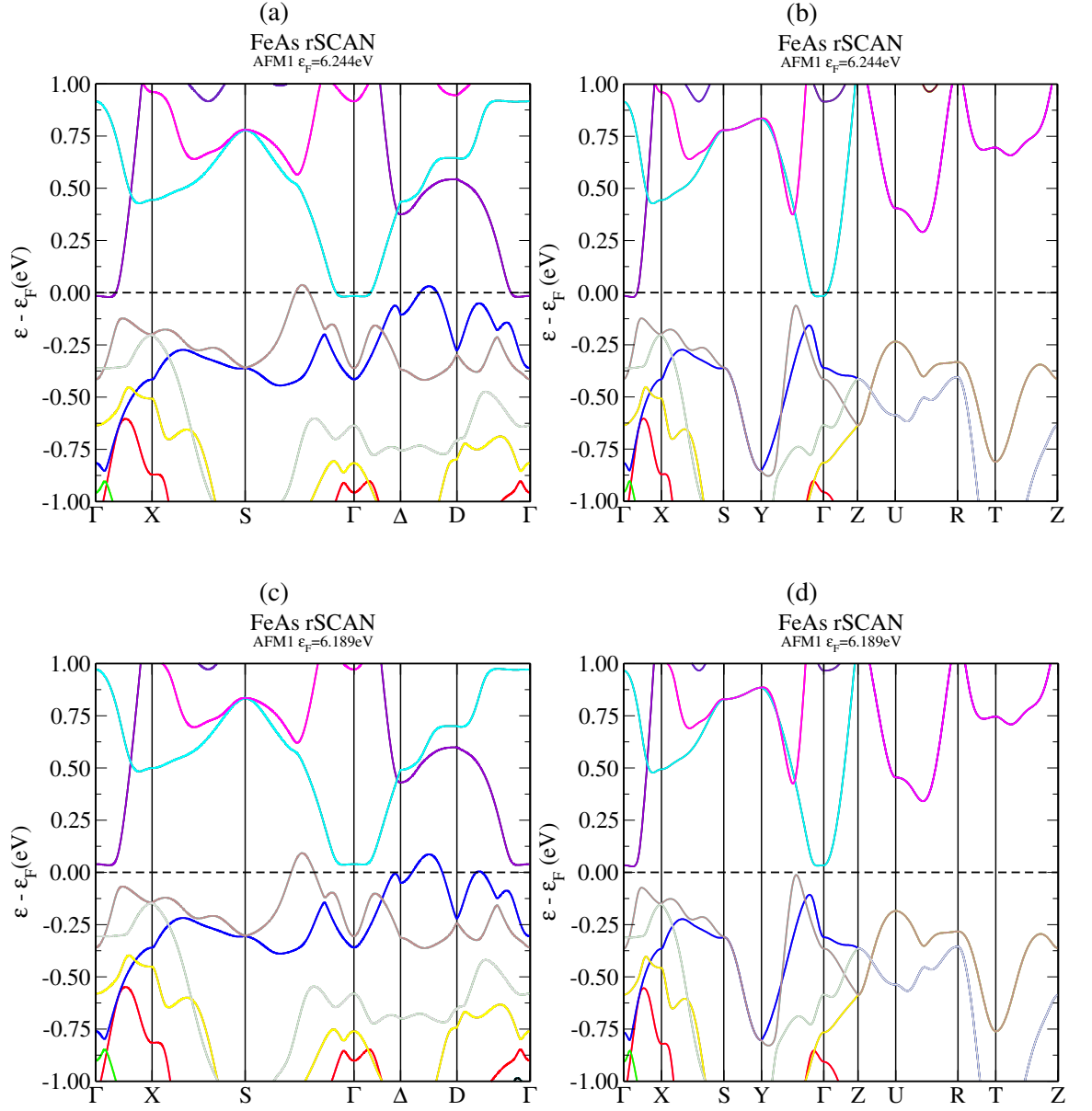
Figure 5.7: A comparison of Band structure for FeAs with the rSCAN functional, show-
ing the difference between CASTEP [16] and OPTADOS [95, 96] Fermi-
energies. The electronic band structure calculations used the cold smear-
ing scheme with smearing width 0.02525eV. The MP k-point grid was
$33\times35\times31$ with a path spacing of $0.001\text{Å}^{-1}$.

cies around the Fermi-level were unoccupied and could not be under the Fermi-level. Figures 5.7c and 5.7d show the OPTADOS determined Fermi-level in the band structure. We observe a decrease in occupation in the direction of Y-$\Gamma$ and an increase in the direction S-$\Gamma$-$\Delta$-D-$\Gamma$. The uniformity in decrease and increase in occupancies suggest they are related.

The difference in occupancies around the Fermi-level in Figures 5.7c and 5.7d show that the transport properties are directional. Conduction of FeAs will, therefore, be easier in the S-$\Gamma$ direction than the R-T direction. This anisotropic nature also relates to the spin density wave; the S-$\Gamma$-$\Delta$-D direction is also the direction in which the wave propagates, which agrees with Griffin *et al.* [146]. Furthermore, the broadness of the bands crossing the Fermi-level indicates delocalisation of the d-state electrons and explains the lower Fe d magnetic moments [139, 142–145].

Figure 5.7a agrees reasonably well with the experimental Fermi surface from Campbell *et al.* [177], there is a small electron pocket at the $\Gamma$ point and small hole pockets in the S-$\Gamma$ and $\Delta$-D directions. The size of the pockets are significantly smaller than those presented by Griffin *et al.* [146]; however, the size of the pockets was the main critique of Campbell *et al.* about Fermi surface shown by Griffin *et al.*. Further, the shape of the two hole pockets are similar due to the parabolic nature of the bands near the maximum. However, Campbell *et al.* describe identical hole pockets, and the hole pockets in Figure 5.7a are similar but not identical. The small size of the pockets indicates that there would be few electron and hole carriers, from a rough integration of the volume of the pockets.

The OPTADOS determined Fermi level, Figure 5.7c, reveals the disappearance of the electron pocket at the $\Gamma$ point, which disagrees with the de Haas Fermi surface from Campbell *et al.* [177]. In addition, the hole pockets in the S-$\Gamma$ and $\Delta$-D directions are larger, indicating a bigger Fermi surface than with the CASTEP Fermi-level. They also reveal that holes are the main carriers in the crystal, with the potential for more holes than

Figure 5.7a as the volume of the pocket is larger.

### 5.4.3.2 FeSe

This section will investigate the antiferromagnetic band structure for FeSe. The purpose is to compare with FeAs and determine if rSCAN can improve upon the theoretical description of the band structure, which is in disagreement with ARPES measurements [178]. The path through the Brillouin zone is taken from Ma *et al.* [167] as it encompasses most paths found in the literature. The path is: $M$ - $X$ - $\Gamma$ - $\bar{X}$ - $M$ - $\Gamma$ - $Z$ - $R$ - $A$ - $Z$ - $\bar{R}$ - $A$ - $M$. The electronic band structure is the folded band structure for the supercell $\sqrt{2}$a $\times$ $\sqrt{2}$a $\times$c. We used the cold smearing scheme with a smearing width of 0.02525eV (293K), which is higher than the temperature where the material is superconducting.
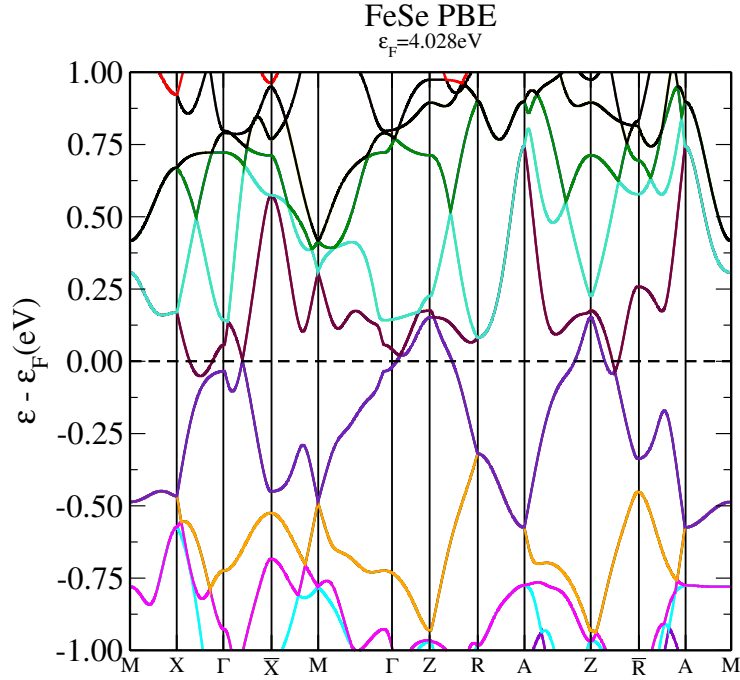


Figure 5.8: The folded band structure for FeSe with the PBE functional. The electronic band structure calculations used the cold smearing scheme with smearing width 0.02525eV. The MP k-point grid was $33\times33\times30$ with a path spacing of $0.001\text{Å}^{-1}$.

Figure 5.8 shows the folded band structure for FeSe using the PBE functional under the cold smearing scheme. There is good agreement with

the shape and positioning of the bands compared with Ma *et al.* [167]. The location and size of the hole pockets at the Z point also agree with Ma *et al.* and ARPES measurements from Waston *et al.* [171]. Further, the number of hole pockets agree with ARPES measurements by Maletz *et al.* [169] . However, the appearance of the electron pocket, with a minimum of -0.051eV, in the X-$\Gamma$ direction does not. While the electron pocket is small, it does not exist in other DFT calculations and ARPES experiments [167, 169] and is still larger than ARPES electron pockets [169]. There is a further electron pocket in the Z-$\bar{R}$ direction, which has decreased in size compared to Ma *et al.*. The higher verbosity output from CASTEP show the occupations of the bands closest the Fermi-level and confirm the electron pockets as occupied. In the direction $\Gamma$-$\bar{X}$ the electron pocket in Ma *et al.* is a hole pocket in Figure 5.8, with a maximum of 0.020eV. However, the number of k-points forming this hole pocket are just five and so a denser k-point sampling would be needed to have confidence in claiming the existence of this hole pocket.
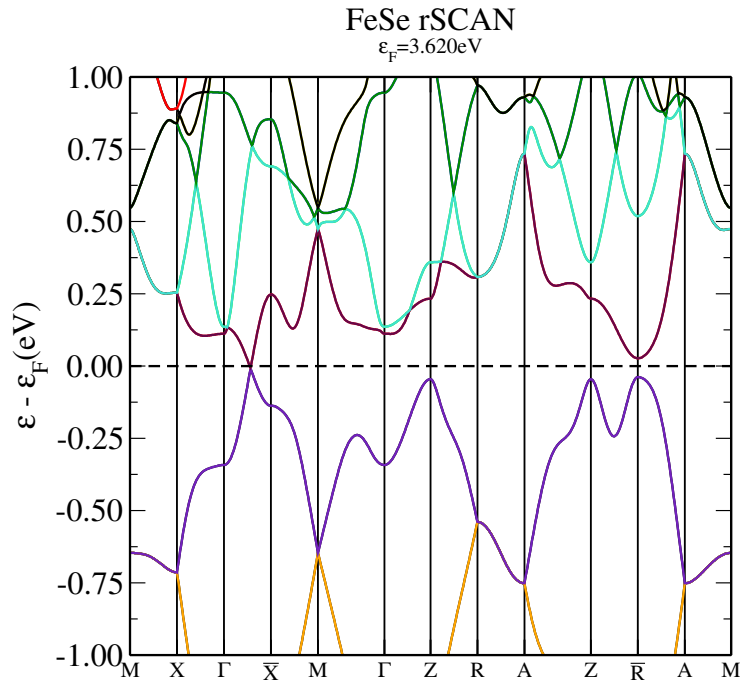


Figure 5.9: The folded band structure for FeSe with the rSCAN functional. The electronic band structure calculations used the cold smearing scheme with smearing width 0.02525eV. The MP k-point grid was $33\times33\times30$ with a path spacing of $0.001\text{Å}^{-1}$.

Figure 5.9 reveals the folded electronic band structure generated using the rSCAN functional with the cold smearing scheme and a broadening of 0.02525eV (293K). The most striking feature of the band structure is the absence of the hole pockets, particularly at symmetry points reported to have them through ARPES measurements (Z, above $T_s$) [171]. Further, there is an increase in the distance between the conduction bands and the valance bands, even in the $\Gamma$-$\bar{X}$ direction; despite the qualitative appearance of conduction and valance bands meetings, there is a small band gap of 8meV. Moreover, the direction $\Gamma$-$\bar{X}$ contains a very small electron pocket, with a minimum of -5.39meV. The number of k-points that form this pocket is small at just three. Therefore, further calculations on smaller paths are required to have confidence in this electron pocket. While the band gap is tiny, the confidence in the conduction band creating the electron pocket is questioned for the same reasoning with FeAs: the iterative nature of how CASTEP determines the Fermi-level.

## 5.5 Discussion

### 5.5.1 FeAs

The LDA functional compared poorly with experimental results and with the other XC functionals, underestimating the structural parameters by around 9% and converging to an unrealistic non-magnetic ground state. The failing of the LDA functional could originate from the homogeneous approximation of the exchange and correlation [20], failing to model the quickly changing nature of the spin density. Another possibility for the LDA failure comes from the determining cause of magnetism within FeAs: instability of the delocalised Fe d-band electron [139, 142–145]. The delocalisation is difficult for the strictly local exchange, such as that in LDA, to model. However, the true nature of this underestimation and poor magnetic representation

would require further investigation to determine if it is a failure of LDA or the level of theory used.

The PBE functional produced structural parameters much closer to the experimental results, underestimating the lattice parameters by a maximum of 2%, a trait which has become unique of iron arsenide. Furthermore, the magnetic properties exhibited through the PBE functional showed a localised moment picture, which contradicted current experimental understanding. A competition between localised and delocalised magnetism within DFT and experiment is well documented [145, 146, 166, 179]. The discrepancy arises from the material resting between the weakly and strongly correlated limits.

The differences between LDA and PBE magnetism within iron arsenide indicates that the XC functional plays a significant role in accurately modelling this system. Therefore, the most likely source of the difference stems from the variations between those functionals. The magnetism within the system is known to be quickly varying through spin density waves and anisotropy [145, 146, 150, 153, 166, 172]. While PBE has a semi-local exchange, it is still restricted by the slow-varying limit [22], which could be why it fails to detect itinerancy.

Another reason could be, again, the simplicity of the model employed. The lack of spin-orbit coupling and non-co-linear magnetism could be enough of a handicap as not to distinguish between local moments and itinerancy. Typically spin-orbit coupling energy is of meV in magnitude, which is enough to change the magnetic interactions within the system. As other DFT calculations have had success with PBE in modelling co-linear magnetism within iron arsenide from the inclusion of spin-orbit coupling [145, 146, 166], it becomes apparent that the model employed in this investigation was likely too unsophisticated.

The rSCAN functional relaxed the material into a structure with a volume that was in excellent agreement with experiment. The most significant

discrepancy comes at 2.68%, which is in line with other XC functionals. Furthermore, through the increased broadness of the d-bands crossing the Fermi-level in the directions S-$\Gamma$ and $\Delta$-D, the functional predicts itinerancy for the AFM1 state, which is the ground state magnetism of iron arsenide. Only the carriers in the pockets can contribute to itinerancy as they form the Fermi surface.

The itinerancy is significantly different to the GGA, which predicts localised moments. The ability for rSCAN to detect the experimentally verified itinerancy within the system stems from three sources, the inclusion of the orbital kinetic energy density, the improvement on the PBE-like semi-local exchange and the isoorbital indicator [27, 28]. These developments allow for the functional to handle the faster-varying density better and subsequently increases the magnetic moments.

The band structures of iron arsenide reveal that the electronic and magnetic structures are highly susceptible to the XC functional used. For instance, the PBE functional predicts metallic behaviour via Fermi-pockets, whereas rSCAN predicted weak metallic behaviour in the S-$\Gamma$ direction and semi-metallic behaviour in the S-Y-$\Gamma$ direction. In verifying this result, the Gaussian smearing scheme with its unphysical broadening parameter was abandoned as it failed to reproduce the PBE band structure from Griffin *et al.* [146].

These shortcomings highlighted a fundamental issue with Gaussian smearing: the addition to the total energy and forces, making them higher than at the real T=0K. The total energy is corrected for post hoc; however, the forces and stresses cannot be. As a result, the contribution does play a significant role, as the occupation depends on the smearing scheme used, which affects the positioning of the Fermi-energy, and the Gaussian smearing can cause very high and unrealistic occupations. Therefore the justification for changing smearing schemes is self-evident.

Out of the smearing schemes available, the Methfessel-Paxon [35] scheme

is a good choice; however, creating unrealistic negative occupancies is complex to handle, especially as the smearing is closer to 0K, which is the region negative occupancies typically arise. Thus, the negative occupancies would be even more impactful on the Fermi-level, of which much of this investigation focused. For those reasons, the cold smearing scheme [34] is a good choice as it never deviates far from 0K, even with large smearing widths and has physical occupancies.

The PBE functional shows good agreement with previous DFT electronic band structure calculations, Griffin *et al.* [146], achieved by changing the smearing scheme, reducing the smearing width and increasing the number of k-points sampling the Brillouin zone. The band structure produced with the PBE functional reveals delocalised bands around the Fermi-level, as expected by the low magnetic moment on the Fe ions.

The rSCAN XC functional shows a more complex picture for the band structure as, depending on the direction of travel, the Fe d-states are either somewhat delocalised or localised, made clear from the difference in broadness of the bands closest the Fermi-level in those directions. For instance, the delocalised d-bands observed in the direction S-$\Gamma$ and $\Delta$-D in Figure 5.7c and localised bands in the Y-$\Gamma$ direction in Figure 5.7d. Compared to the band structure produced by PBE in Figures 5.6a and 5.6b, the overall trend with rSCAN is more localised bands, which is consistent with the higher Fe d magnetic moments

Comparing the Fermi surfaces of the two XC functionals with the experimentally determined de Haas Fermi surface reveals that overall the PBE functional better produces key characteristics of the de Haas Fermi surface from Campbell *et al.* (see Figure 5.6a). For instance, the location and general appearance of the electron and hole pockets. However, the PBE functional overestimates the size of the pockets. The rSCAN functional with the CASTEP Fermi-level agrees with experimental Fermi surface and there is similarity with the PBE Fermi surface in relation to the location of

the pockets, however the shape of the electron pocket differs greatly. The rSCAN electron pocket is flatter at the minimum with PBE containing two local minimas. The experimental electron pocket shape most closely resembles the rSCAN electron pocket. With the OPTADOS Fermi-level, the electron pocket at the $\Gamma$ point disappears which is not in agreement with the Fermi surface from Campbell *et al.*, for this Fermi-level the PBE functional is in better agreement with experiment.

Our results focused on two paths through the Brillouin zone, one with precedence in the literature and the other from SeeK-Path. The rSCAN functional highlights the significance of the caution required while using a 2-D representation of 3-D reciprocal space. Figure 5.7d shows a band gap; if this 2-D band structure was the only Brillouin space explored, then a justified claim could be made that FeAs has a band gap which is incorrect. It is only through the other path (see Figure 5.7c) do we see the Fermi-pockets and the metallic behaviour.

As suggested by Griffin *et al.* [146], the bands crossing the Fermi level could influence the generation and favouring direction of the spin density wave; we would add that the low occupation of other bands also contributes. However, more sophisticated investigations involving spin-orbit coupling and non-co-linear magnetism are required. Furthermore, these calculations will demand tighter energy tolerances between self-consistent cycles, similar to that needed by phonons ($E_{tol}=1\times10^{-10}$eV and tighter) to detect the meV differences in magnetic states.

### 5.5.2 FeSe

The lattice parameters of the optimised unit cell, showed a poor comparison with experimental for the LDA functional with an underestimation of the length of around 10%. This discrepancy is roughly the same as found with FeAs. The magnetic moments are larger than other first-principles inves-

tigations using the LDA functional. The difference between these results could come from the variations in approximations used, as Sudebi *et al.* [168] focused on investigating and modelling the spin density wave, which could account for the decreased magnetic moments.

The geometry optimisations using the PBE and rSCAN functionals converged to a structure closer to experiment with a maximum deviation of 1.5%. The position of the Se ions along the Z-direction differed by about 6%. However, the structures are very close to experiment and should not be the source of significant disparities with experiment. The strength of the magnetic moments increases with the complexity of the functional used. We observe this trend in both FeAs and FeSe, which contain spin density waves, fast varying densities and anisotropy, all of which are difficult for local and semi-local exchanges to model.

The folded band structure for FeSe using the PBE functional under the cold smearing scheme showed minor differences with the band structure using the same functional from Ma *et al.* [167]. The shape and positioning of the bands, on the whole, agree with their electronic band structure. However, the main difference is the appearance of the electron hole in the X-$\Gamma$ direction. This is not found in other DFT calculations or ARPES measurements [168, 169, 171].
The difference in the size of the hole pockets compared to ARPES measurement could result from the size of the smearing width, which is set to 0.02525eV (293K). The ARPES measurements were conducted at temperatures below 120K [171]. The computational ramifications of using the equivalent smearing width are SCF cycles which are very difficult to converge. Therefore, further investigations are required to explore the effect of the smearing width. In addition, confirmation of the existence of the small hole pocket in the direction $\Gamma$-$\bar{X}$ requires further investigation. The reasoning comes from the poor sampling rate of k-points creating the hole. Only five k-points make this hole pocket; however, the k-point spacing was 0.001

Å$^{-1}$ with the MP grid 33 × 33 × 30; therefore, to increase the number of k-points in this region of the Brillouin zone, a smaller path is required. Finally, the other possibility to explain the presence of the electron pocket in the X-Γ direction is the ionic positions of the crystal. The folded band structure is in good overall agreement with the band structure from Ma *et al.*, and so it is unlikely that there are significant structural differences. However, further investigation is required to provide confidence in the similarity of the two structures.

The rSCAN functional predicts a small Fermi surface with a single electron pocket. This prediction is in disagreement with ARPES and de Haas measurements, which predict two hole pockets and two electron pockets [171]. Further investigation into the smearing scheme and broadening is required to fully understand if this is an effect of rSCAN alone or the combined effect of the rSCAN functional and the cold smearing scheme. In addition, the comparison with the experimental measurements from ARPES and de Haas techniques were conducted at a temperature below 120K, which is different to our smearing of 293K. Another aspect to consider is the positioning of the Fermi-level; the iterative process in CASTEP can incorrectly place the chemical potential (see Section 2.3.3.1). This would require the same process with FeAs, using a denser density of states grid in OPTADOS to better estimate the Fermi-energy. Further, the two hole pockets at the Z-point measured in ARPES experiments by Watson *et al.* are found in their GGA calculation only through consideration of spin-orbit coupling, which causes a split in the degeneracy of the $\alpha$ and $\beta$ bands of an energy scale $\Delta_{SO} \approx 20$meV. Therefore, requiring further investigations involving tightly converged calculations to model the effects of spin-orbit coupling.

Comparing the band structures of the PBE functional for FeAs and FeSe, we observe that FeAs is closer to the de Haas measurements of the Fermi surface than FeSe. However, both are in reasonable agreement

with their respective literature and provide a good platform for comparison with the rSCAN functional.

The band structures for FeAs and FeSe using the rSCAN functional show a decrease in conduction and valance band overlap, with a complete separation in FeSe. The manifestation of this in both materials suggests that this has transferability across the iron pnictides. However, the electronic band structures for both materials have more disagreement with experimental measurements of the Fermi surface than those found with PBE. With FeAs, the shape of the bands closest and forming the Fermi surface better agreed with de Haas measurements; however, the electron pocket is not present. The Z point (the Z-$\bar{R}$ direction) in FeSe has a slight elongation which also agrees better with experimental measurements of that band; however, this only occurs because another maximum of the band emerges at $\bar{R}$ and it does not contribute to the shape of the Fermi surface. However, to have confidence in the folded band structure of FeSe, further investigations into band occupations, the position of the Fermi-level and spin-orbit coupling are required to better compare to ARPES and de Haas measurements.

As a final note, our results in this chapter have demonstrated that rSCAN has overestimated the magnetic moments, reduced the size of the band gap and produced bands in better qualitative description to experiment. The strength of the magnetic moment produced by SCAN is not uncommon within the literature as Fu and Singh [180] report. The SCAN XC functional overestimated the magnetic moments of mono Fe, Co and Ni, producing a worse fit with experiment than PBE. This is common to the research in this chapter with rSCAN.

## 5.6   Conclusion

In conclusion, the comparison of the XC functionals for FeAs has revealed the importance of which functional is used as results vary greatly. For example, the LDA functional performed poorly with underestimating the unit cell volume by 9% and converging to a non-magnetic state. However, PBE and rSCAN functionals converged to magnetic states and underestimated (PBE) and overestimated (rSCAN) the unit cell volume by less than 3%. In addition, the rSCAN functional was the only XC functional used which exhibited itinerancy, a physical property of FeAs.

Despite each functional either underestimating or overestimating the unit cell volume, the system relaxed into the *Pnma* symmetry, which agrees with experimental results.

The rSCAN XC functional uniquely showed a difference in the number of bands crossing the Fermi-level and exhibits a band-gap in the Y-$\Gamma$ direction. This band gap has not been detected by any other XC functional. The position of the Fermi-level was confirmed through OPTADOS, which positioned it 51meV lower than that calculated through CASTEP. Through CASTEP's higher verbosity output, the valance bands above the Fermi-level were confirmed to be unoccupied and therefore could not be below the Fermi-energy. Therefore, we propose that the formation of this band-gap is due to the band crossing elsewhere in the Brillouin zone lowering the occupation substantially enough to force a band-gap, as seen in Figure 5.7.

For the iron pnictide, FeSe, the comparison of the LDA, PBE and rSCAN XC functionals shows the LDA functional underestimate the lattice parameters the most by around 10%. The PBE and rSCAN functional agree with experimental lattice parameters with a maximum discrepancy of around 1.5%. We observe the increase in strength of the magnetic moments with the complexity of the functional used, rSCAN providing the largest

Fe-site magnetic moment. Further, all three functionals present residual magnetism on the Se ions of around $0.06\mu_B$. There is a difference with other DFT calculations on the strength of those moments, originating from the different approximations used.

The PBE functional produced a folded band structure which is in reasonable agreement with experiment but differs significantly in the existence of an electron pocket in the X-$\Gamma$ direction. This electron pocket is not found in ARPES measurements and requires further investigations to discover the source of the pocket.

Finally, the folded band structure for FeSe calculated from the rSCAN functional under the cold smearing scheme fails to capture the hole pocket at the Z point as measured in ARPES experiments [171]. There is an increase in the gap between the conduction and valance bands, resulting in a small band gap of 8meV in the $\Gamma$-$\bar{X}$ direction. However, the k-point sampling rate is too low to attribute confidence in this band gap. Also in this direction is a small electron pocket, although further calculations are required to confirm if this band is occupied. Further, to have confidence in the chemical potential value requires OPTADOS calculations, as rSCAN predicts a small band gap which could be a consequence of the iterative nature of CASTEPs Fermi-level. The ARPES measurements from Watson *et al.* [171] indicate the significance of spin-orbit in splitting the degeneracy of the $\alpha$ and $\beta$ bands at the Z point forming the hole pocket. While rSCAN does not predict a hole at the Z point, the effects of spin-orbit coupling are impactful on the band structure and so further calculations are required to more accurately model the band structure.

## 5.7 Future Works

In order to truly understand the source of the band gap exhibited by the rSCAN XC functional and the anisotropy that relates to it, a more detailed

Hamiltonian is needed. The Hamiltonian would need to include the relativistic effects of spin-orbit coupling and non-co-linear magnetism to reveal the implications of the band gap on the spin density wave and vice versa. The investigation should also include a more thorough understanding of the transport properties in the different Brillouin directions and their impact on the magnetic moments. The LDA, PBE and rSCAN XC functionals, to some extent, underestimate the magnetic properties of the iron pnictides, so further work is needed to determine if it is a limitation of the functionals or the level of theory employed.

# Chapter 6

# Conclusions

The work presented in this thesis aimed to investigate various magnetic properties of materials and then review the validity of the methods used. Chapter 2 contained the theoretical introduction to density-functional theory and the practical computational adaptation, allowing DFT codes to function. The theoretical basis also included the *ad hoc* magnetic extension to the first-principles methods.

Magnetoresistance describes the functional and valuable relationship between the magnetism and transport properties of a material. This relationship is usually found within double-perovskites and has previously only been found in metals or half-metals.

Chapter 3 investigated the unusual insulating double perovskite $Tl_2NiMnO_6$, which exhibited the magnetic phenomenon, magnetoresistance. The investigation used electronic band structures and effective masses to examine the relationship between the insulating behaviour and transport properties. The double perovskite exhibited some level of disorder, and to avoid computationally expensive methods; the VCA was used to model the occupational disorder. The material exhibited strong ferromagnetism, with the majority spin channel dominant under the Fermi-energy. Employing Hubbard-U for the on-site correction revealed a previously indistinguishable band gap. The band gap in both the density of states and the band structure was sufficiently small enough to show semiconducting behaviour and not insulating. The broadness of the density of states and residual magnetism on the non-magnetic sites shows itinerancy within the system. Itinerancy would be expected in the case where magnetism and transport properties are intertwined. By fitting parabolas to the maxima and min-

ima of the bands closest the Fermi-level revealed the effective masses of the electrons and the holes, showing that holes play a predominant part in transport. There was a difference in the effect masses of the holes between the $\Gamma$-A and A-E directions, indicating anisotropy,and a difference in transport properties between those directions. This is a potential consequence of the colossal magnetoresistance. However, further investigations involving relativistic first-principles calculations would be needed to validate this relationship.

Molecular magnets are at the computational extreme, so numerous in ions and electrons that only national supercomputers can hope to calculate their complex ground state properties. Chapter 4 aimed to investigate the nature of the discrepancy between experimentally determined total magnetism and the *ab initio* values of the molecular magnet, $Cr_{10}$. This chapter also investigates the $Cr_8$ molecular magnet to use as a comparison with the $Cr_{10}$, highlighting the differences and influence of the number of next-nearest neighbour interactions. $Cr_{10}$ has frustrated next-nearest neighbours, while $Cr_8$ does not. The impact of this frustrated is visible in $Cr_{10}$ spin density isosurfaces. Further differences come from magnetic ground states which is ferromagnetic fro $Cr_{10}$ and antiferromagnetic for $Cr_8$.

The investigation, through hydrogen saturation, determined a higher applicable symmetry to the $Cr_{10}$ molecule ($D_5$), which allowed for a DFT approach that did not rely on crystal symmetry ($Cr_8$) but used ionic constraints to maintain the $D_5$ point group symmetry.

Comparison of the magnetic properties between the $D_5$ symmetry and the previous literature $C_1$ symmetry revealed a noticeable difference. For the $D_5$ symmetry the magnetic moments were closer to experiment and had more reliable exchange interaction parameters, due to structural consistency. However, the exchange constants were larger in magnitude than the experimental ones; although similar in size to other *ab initio* investigations. We are unable to determine the source of this discrepancy. It

is possible that including non-co-linear magnetism and spin-orbit coupling could provide excitations in better agreement with experiment. However, the nearest neighbour Heisenberg model used to fit the experimental data may be too simplistic and so there is no guarantee of agreement.

The fixed spin moment constraint revealed that the ground state for the $Cr_{10}$ molecule is ferromagnetic with $S_{tot}=30\mu_B$. This is in contrast with experimental susceptibility measurements which indicated a ground state magnetism of $S_{tot}=18\mu_B$, corresponding to two anti-parallel spins to the other eight. The LDA functional does not predict the next-nearest neighbours influence to the same extent as the PBE and rSCAN functionals, which visibly show it in the spin density isosurfaces. The magnetic dependency on the XC functional indicates that the XC holes are an influential factor.

Magnetostriction was also examined on a fundamental level as a magnetostrictive force which revealed magnetostriction is possible within the material. However, further investigations using very fine and well converged spin-orbit coupling calculations are needed to reveal the nature of the magnetostriction.

Iron pnictides have exhibited complex magnetism through spin density waves and superconductivity. Chapter 5 aimed to investigate if the rSCAN XC functional can provide new insights into the band structure and subsequently the complex magnetism represented by the spin density waves in FeAs and FeSe. The investigation into FeAs tested three different co-linear magnetic configurations relating to all the possible spin parallel-antiparallel pairs. Comparison of the LDA, PBE and rSCAN XC functionals allowed for an understanding that the magnetic properties modelled depend highly upon the XC functional chosen.

Of these functionals, LDA compared the worst with experiment by converging to non-magnetic states for each of the magnetic arrangements investigated. This characteristic continued into the geometry optimisation with

LDA underestimating the lattice parameters and subsequently the unit cell volume by around 9%. On the other hand, PBE converged to magnetic states but exhibited localised moments instead of itinerancy, which is experimentally determined through resistivity measurements. The PBE functional underestimates the lattice parameters and cell volume by 2%, which is a significant improvement on LDA.

Finally, rSCAN performed well, converging to a magnetic ground state for each configuration and exhibiting itinerancy. The rSCAN functional performs reasonably well with PBE but overestimates the lattice parameters and volume by 2.68%. Furthermore, the magnetic moments on the Fe ions with the rSCAN functional were larger than PBE by a mean value of $1.41\mu_B$. For both PBE and rSCAN, the strength of the on-site magnetic moment depended upon the number of antiferromagnetic pairs. The high sensitivity of the magnetic moments to the XC functional used suggests a great deal of sensitivity to spin fluctuations. This suggests the possible existence of competing electronic states such as orbital ordering which has been observed in other FeAs based superconductors, such as $Sr_2VO_3FeAs$ [181].

For FeSe, the trend in the results appeared similar to FeAs. LDA underestimated the lattice parameters by around 10% while PBE and rSCAN predicted parameters closer with experiment and other DFT calculations. However, all three XC functional converged to an antiferromagnetic ground state with a residual magnetic moment on the Se ions. The strength of the Fe magnetic moments, as with FeAs, increased in magnitude with the complexity of the functional used. This observation, provides weight to the suggestion of orbitally ordered states, which have been mooted in FeSe [182]. However, as with FeAs, this is beyond the scope of this investigation and would require more research into the legitimacy of attributing this behaviour to orbital ordering.

These differences could also be down to the local and semi-local ex-

change of the LDA, PBE and rSCAN, which ultimately struggle to handle the fast-varying spin density. However, further research would be needed to determine whether the fault lays the local and semi-local exchanges or if it is a failing of the level of theory employed.

The electronic band structures are highly sensitive to the smearing scheme used. The Gaussian scheme proved unsuitable as it artificially raised the Fermi-level to give the impression of occupation in empty bands. The cold smearing schemed reduced this oversight. However, an external program, OPTADOS, provided a lower Fermi-level through a denser sampling of the Brillouin zone. This caused significant changes in the rSCAN electronic band structures, whereby a band gap opened in a region of the Brillouin zone previously modelled as metallic (Y-$\Gamma$). In addition, other regions of the Brillouin zone (Y-$\Gamma$ and $\Delta$-D) have increased density around the Fermi-level, suggesting a possible cause for the decreased occupancy elsewhere. The implications this has upon the spin density wave and non-co-linear behaviours need further investigation.

In comparison with the de Haas measurement to determine the extreme points of the Fermi surface, the PBE band structure overestimated the size of the electron and hole pockets, but correctly predicted their positions in the Brillouin zone. The rSCAN functional predicted the shapes of the electron and hole pockets in better agreement with experiment, however upon using the OPTADOS calculated Fermi-level, the electron pocket disappeared.

The FeSe folded band structure using the PBE functional showed that the behaviour of the bands at the Fermi-level are highly susceptible to the tuning parameters such as k-point density, smearing scheme and broadening. However, there is good agreement in the positioning of the hole pockets in comparison to the ARPES measurements from Watson *et al.*. On the other hand, the band structure calculated using the rSCAN functional showed greater disagreement with the ARPES measurements; fail-

ing to predict the Z point hole pocket. However, the k-point sampling rate of the rSCAN band structure is too low to extract meaningful observations confidently.

We observe similar characteristics from the rSCAN functional in both the FeSe and FeAs band structures. Both band structures see an increase in distance (or a decrease in overlap) between the conduction and valance bands around the Fermi-level. However, in the FeAs band structure, the shape of the bands forming the electron and hole pockets better resemble the shape described by de Haas measurements.

The first-principles investigations in this thesis have shown the subtlety of magnetic phenomena in *ab initio* results. For instance, we observed magnetic states with little difference in their final energies, small differences in the spin densities of different XC functionals and high susceptibility of electronic structures on computational parameters. There were limitations to the methods used in this thesis which prevented a comprehensive understanding of the fundamental magnetic mechanisms responsible for the observed phenomena. For example, spin-polarised co-linear DFT was unable to fully describe any spin fluctuations the systems studied in thesis, as the magnetic moments were treated as Ising-like.

The overall application of the rSCAN functional to the different systems in this thesis have shown a greater degree of agreement with experimental geometries and provided a deeper understanding of the effects of exchange interactions. However, rSCAN predicted band structures with key experimental features missing; as made clear with the iron pnictide superconductors electron and hole pockets.

Finally, as a note to a reader starting in magnetic *ab initio* research: do not fall into the fallacy of using DFT codes as a 'black box'. Question the output of the DFT codes; this thesis has shown, through comparing XC functionals, how complex magnetism is subtle in DFT output.

# Notes

# Bibliography

[1] A. A. Mills, "The Lodestone: History, Physics, and Formation", Annals of Science **61**, 273–319 (2004).

[2] B. Bhushan, "Historical evolution of magnetic data storage devices and related conferences", Microsystem Technologies **24**, 4423–4436 (2018).

[3] J. H. Van Vleck, *The theory of electric and magnetic susceptibilities,* English, OCLC: 845050 (Clarendon Press, Oxford, 1932).

[4] Jürgen Kübler, *Theory of Itinerant Electron Magnetism*, International Series of Monographs on Physics (Oxford University Press, Oxford, New York, Oct. 2000).

[5] A. V. Gold, "Review paper: Fermi surfaces of the ferromagnetic transition metals", en, Journal of Low Temperature Physics **16**, 3–42 (1974).

[6] T. Moriya, "Theory of itinerant electron magnetism", en, Journal of Magnetism and Magnetic Materials **100**, 261–271 (1991).

[7] T. Moriya, "Recent progress in the theory of itinerant electron magnetism", en, Journal of Magnetism and Magnetic Materials **14**, 1–46 (1979).

[8] P. W. Anderson, "New Approach to the Theory of Superexchange Interactions", Physical Review **115**, Publisher: American Physical Society, 2–13 (1959).

[9] M. A. Ruderman and C. Kittel, "Indirect Exchange Coupling of Nuclear Magnetic Moments by Conduction Electrons", Physical Review **96**, Publisher: American Physical Society, 99–102 (1954).

[10] T. Kasuya, "A Theory of Metallic Ferro- and Antiferromagnetism on Zener's Model", Progress of Theoretical Physics **16**, 45–57 (1956).

[11] K. Yosida, "Magnetic Properties of Cu-Mn Alloys", Physical Review **106**, Publisher: American Physical Society, 893–898 (1957).

[12] J. C. Slater, "The Theory of Complex Spectra", Physical Review **34**, Publisher: American Physical Society, 1293–1322 (1929).

[13] N. Singh, "The story of magnetism: from Heisenberg, Slater, and Stoner to Van Vleck, and the issues of exchange and correlation", en, arXiv:1807.11291 [cond-mat, physics:physics], arXiv: 1807.11291 (2018).

[14] E. C. Stoner, "Collective electron ferromagnetism", Proceedings of the Royal Society of London. Series A. Mathematical and Physical Sciences **165**, Publisher: Royal Society, 372–414 (1938).

[15] W. Jiang, H. Huang, and F. Liu, "A Lieb-like lattice in a covalent-organic framework and its Stoner ferromagnetism", en, Nature Communications **10**, 2207 (2019).

[16] S. J. Clark, M. D. Segall, C. J. Pickard, P. J. Hasnip, M. I. J. Probert, K. Refson, and M. C. Payne, "First principles methods using CASTEP", en, Zeitschrift für Kristallographie - Crystalline Materials **220**, Publisher: Oldenbourg Wissenschaftsverlag Section: Zeitschrift für Kristallographie - Crystalline Materials, 567–570 (2005).

[17] P. Hohenberg and W. Kohn, "Inhomogeneous Electron Gas", Physical Review **136**, Publisher: American Physical Society, B864–B871 (1964).

[18] J. C. Slater and J. C. Phillips, *Quantum Theory of Molecules and Solids Vol. 4: The Self-Consistent Field for Molecules and Solids*, Vol. 4, Publisher: American Institute of Physics (Dec. 1974).

[19] Charles Kittel, *Quantum Theory of Solids, 2nd Revised Edition — Wiley*, en-gb (1967).

[20] W. Kohn and L. J. Sham, "Self-Consistent Equations Including Exchange and Correlation Effects", Physical Review **140**, Publisher: American Physical Society, A1133–A1138 (1965).

[21] L. J. Sham and W. Kohn, "One-Particle Properties of an Inhomogeneous Interacting Electron Gas", Physical Review **145**, Publisher: American Physical Society, 561–567 (1966).

[22] J. P. Perdew, K. Burke, and Y. Wang, "Generalized gradient approximation for the exchange-correlation hole of a many-electron system", Physical Review B **54**, Publisher: American Physical Society, 16533–16539 (1996).

[23] J. Tao, J. P. Perdew, V. N. Staroverov, and G. E. Scuseria, "Climbing the Density Functional Ladder: Nonempirical Meta–Generalized Gradient Approximation Designed for Molecules and Solids", Physical Review Letters **91**, Publisher: American Physical Society, 146401 (2003).

[24] J. Sun, B. Xiao, and A. Ruzsinszky, "Communication: Effect of the orbital-overlap dependence in the meta generalized gradient approximation", The Journal of Chemical Physics **137**, Publisher: American Institute of Physics, 051101 (2012).

[25] Y. Zhao and D. G. Truhlar, "A new local density functional for main-group thermochemistry, transition metal bonding, thermochemical kinetics, and noncovalent interactions", The Journal of Chemical Physics **125**, Publisher: American Institute of Physics, 194101 (2006).

[26] J. M. del Campo, J. L. Gázquez, S. B. Trickey, and A. Vela, "A new meta-GGA exchange functional based on an improved constraint-based GGA", en, Chemical Physics Letters **543**, 179–183 (2012).

[27] J. Sun, A. Ruzsinszky, and J. P. Perdew, "Strongly Constrained and Appropriately Normed Semilocal Density Functional", Physical Review Letters **115**, Publisher: American Physical Society, 036402 (2015).

[28] A. P. Bartók and J. R. Yates, "Regularized SCAN functional", The Journal of Chemical Physics **150**, Publisher: American Institute of Physics, 161101 (2019).

[29] M. C. Payne, M. P. Teter, D. C. Allan, T. A. Arias, and J. D. Joannopoulos, "Iterative minimization techniques for ab initio total-energy calculations: molecular dynamics and conjugate gradients", Reviews of Modern Physics **64**, Publisher: American Physical Society, 1045–1097 (1992).

[30] C. Shannon, "Communication in the presence of noise", Proceedings of the IEEE **72**, Conference Name: Proceedings of the IEEE, 1192–1201 (1984).

[31] J. W. Cooley and J. W. Tukey, "An algorithm for the machine calculation of complex Fourier series", en, Mathematics of Computation **19**, 297–301 (1965).

[32] H. J. Monkhorst and J. D. Pack, "Special points for Brillouin-zone integrations", Physical Review B **13**, Publisher: American Physical Society, 5188–5192 (1976).

[33] C. Fu and K. Ho, "First-principles calculation of the equilibrium ground-state properties of transition metals: Applications to Nb and Mo", Physical Review B **28**, Publisher: American Physical Society, 5480–5486 (1983).

[34] N. Marzari, D. Vanderbilt, A. De Vita, and M. C. Payne, "Thermal Contraction and Disordering of the Al(110) Surface", Physical Review Letters **82**, Publisher: American Physical Society, 3296–3299 (1999).

[35] M. Methfessel and A. T. Paxton, "High-precision sampling for Brillouin-zone integration in metals", Physical Review B **40**, Publisher: American Physical Society, 3616–3621 (1989).

[36] A. K. Rajagopal, "Theory of Inhomogeneous Electron Systems: Spin-Density-Functional Formalism", en, in *Advances in Chemical Physics* (John Wiley & Sons, Ltd, 1980), pp. 59–193.

[37] Eschrig, H., *The Fundamentals of Density Functional Theory*, en, Teubner Texte zur Physik (Vieweg+Teubner Verlag, 1996).

[38] Messiah C., *Quantum Mechanics*, Vol. 2 (North-Holland, Amsterdam, 1978).

[39] J.D.Bjorken and S.D.Drell, *Relativistic Quantum Mechanics*, 1964.

[40] Sakurai J. J., *Advanced quantum Mechanics* (Addison-Wesley, Redwood City, 1967).

[41] G. Baym, *Lectures On Quantum Mechanics*, English, 1st edition (The Benjamin / Cummings Publishing Company, Boulder, Colo., Jan. 1969).

[42] Strange P., *Relativistic quantum mechanics* (Cambridge University Press, Cambridge, 1999).

[43] W. Gordon, "The current of Dirac's electron theory", de, Zeitschrift für Physik **50**, 630–632 (1928).

[44] U. v. Barth and L. Hedin, "A local exchange-correlation potential for the spin polarized case. i", en, Journal of Physics C: Solid State Physics **5**, Publisher: IOP Publishing, 1629–1642 (1972).

[45] A. K. Rajagopal and J. Callaway, "Inhomogeneous Electron Gas", Physical Review B **7**, Publisher: American Physical Society, 1912–1919 (1973).

[46]L. Noodleman, "Valence bond description of antiferromagnetic coupling in transition metal dimers", en, The Journal of Chemical Physics **74**, Publisher: American Institute of PhysicsAIP, 5737 (1998).

[47]A. A. Belik and W. Yi, "High-pressure synthesis, crystal chemistry and physics of perovskites with small cations at the A site", eng, Journal of Physics. Condensed Matter: An Institute of Physics Journal **26**, 163201 (2014).

[48]L. Ding, P. Manuel, D. D. Khalyavin, F. Orlandi, Y. Kumagai, F. Oba, W. Yi, and A. A. Belik, "Unusual magnetic structure of the high-pressure synthesized perovskites ACrO3 (A= Sc, In, Tl)", Physical Review B **95**, Publisher: American Physical Society, 054432 (2017).

[49]P. Kayser, J. A. Alonso, A. Muñoz, and M. T. Fernández-Díaz, "Structural and magnetic characterization of the double perovskites R2NiRuO6 (R = Pr-Er): A neutron diffraction study", en, Acta Materialia **126**, 114–123 (2017).

[50]J. v. d. Brink and D. I. Khomskii, "Multiferroicity due to charge ordering", en, Journal of Physics: Condensed Matter **20**, Publisher: IOP Publishing, 434217 (2008).

[51]Y. Tokura, S. Seki, and N. Nagaosa, "Multiferroics of spin origin", en, Reports on Progress in Physics **77**, Publisher: IOP Publishing, 076501 (2014).

[52]R. J. Cava, B. Batlogg, J. J. Krajewski, R. Farrow, L. W. Rupp, A. E. White, K. Short, W. F. Peck, and T. Kometani, "Superconductivity near 30 K without copper: the Ba 0.6 K 0.4 BiO 3 perovskite", en, Nature **332**, Number: 6167 Publisher: Nature Publishing Group, 814–816 (1988).

[53]Y. Tokura and N. Nagaosa, "Orbital Physics in Transition-Metal Oxides", Science **288**, Publisher: American Association for the Advancement of Science, 462–468 (2000).

[54]W. D. Ratcliff and J. W. Lynn, "Chapter 5 - Multiferroics", en, in *Experimental Methods in the Physical Sciences*, Vol. 48, edited by F. Fernandez-Alonso and D. L. Price, Neutron Scattering - Magnetic and Quantum Phenomena (Academic Press, Jan. 2015), pp. 291–338.

[55]A. Buurma, G. Blake, T. Palstra, and U. Adem, "Multiferroic Materials: Physics and Properties", en, in *Reference Module in Materials Science and Materials Engineering* (Elsevier, 2016), B9780128035818092456.

[56]G. Catalan and J. F. Scott, "Physics and Applications of Bismuth Ferrite", en, Advanced Materials **21**, 2463–2485 (2009).

[57]J. Wang, J. B. Neaton, H. Zheng, V. Nagarajan, S. B. Ogale, B. Liu, D. Viehland, V. Vaithyanathan, D. G. Schlom, U. V. Waghmare, N. A. Spaldin, K. M. Rabe, M. Wuttig, and R. Ramesh, "Epitaxial BiFeO3 Multiferroic Thin Film Heterostructures", en, Science **299**, 1719–1722 (2003).

[58]T. Rojac, M. Kosec, B. Budic, N. Setter, and D. Damjanovic, "Strong ferroelectric domain-wall pinning in BiFeO3 ceramics", Journal of Applied Physics **108**, Publisher: American Institute of Physics, 074107 (2010).

[59] M. Čebela, D. Zagorac, K. Batalović, J. Radaković, B. Stojadinović, V. Spaso-jević, and R. Hercigonja, "BiFeO3 perovskites: A multidisciplinary approach to multiferroics", en, Ceramics International **43**, 1256–1264 (2017).

[60] P. Sanyal, "Theory of the magnetism in La 2 NiMnO 6", (2017).

[61] D. Choudhury, P. Mandal, R. Mathieu, A. Hazarika, S. Rajan, A. Sundaresan, U. V. Waghmare, R. Knut, O. Karis, P. Nordblad, and D. D. Sarma, "Near-Room-Temperature Colossal Magnetodielectricity and Multiglass Properties in Partially Disordered La2MnO6", Physical Review Letters **108**, Publisher: American Physical Society, 127201 (2012).

[62] D. Sánchez, J. A. Alonso, M. García-Hernández, M. J. Martínez-Lope, J. L. Martínez, and A. Mellergård, "Origin of neutron magnetic scattering in antisite-disordered Sr2FeMoO6 double perovskites", Physical Review B **65**, Publisher: American Physical Society, 104426 (2002).

[63] D. D. Sarma, E. V. Sampathkumaran, S. Ray, R. Nagarajan, S. Majumdar, A. Kumar, G. Nalini, and T. N. GuruRow, "Magnetoresistance in ordered and dis-ordered double perovskite oxide, Sr2FeMoO6", Solid State Communications **114**, arXiv: cond-mat/0003237, 465–468 (2000).

[64] M. García-Hernández, J. L. Martínez, M. J. Martínez-Lope, M. T. Casais, and J. A. Alonso, "Finding Universal Correlations between Cationic Disorder and Low Field Magnetoresistance in FeMo Double Perovskite Series", Physical Review Letters **86**, Publisher: American Physical Society, 2443–2446 (2001).

[65] K.-I. Kobayashi, T. Kimura, H. Sawada, K. Terakura, and Y. Tokura, "Room-temperature magnetoresistance in an oxide material with an ordered double-perovskite structure", en, Nature **395**, Bandiera_abtest: a Cg_type: Nature Re-search Journals Number: 6703 Primary_atype: Research Publisher: Nature Pub-lishing Group, 677–680 (1998).

[66] M.-R. Li, M. Retuerto, Z. Deng, P. W. Stephens, M. Croft, Q. Huang, H. Wu, X. Deng, G. Kotliar, J. Sánchez-Benítez, J. Hadermann, D. Walker, and M. Greenblatt, "Giant Magnetoresistance in the Half-Metallic Double-Perovskite Ferrimagnet Mn2FeReO6", en, Angewandte Chemie International Edition **54**, _eprint: https://onlinelibrary.wiley.com/doi/pdf/10.1002/anie.201506456, 12069–12073 (2015).

[67] A. M. Arévalo-López, G. M. McNally, and J. P. Attfield, "Large Magnetiza-tion and Frustration Switching of Magnetoresistance in the Double-Perovskite Ferrimagnet Mn2FeReO6", en, Angewandte Chemie International Edition **54**, 12074–12077 (2015).

[68] S. M. Zhou, Y. Q. Guo, J. Y. Zhao, S. Y. Zhao, and L. Shi, "Nature of short-range ferromagnetic ordered state above TC in double perovskite La2NiMnO6", Applied Physics Letters **96**, Publisher: American Institute of Physics, 262507 (2010).

[69] D. Serrate, J. M. D. Teresa, and M. R. Ibarra, "Double perovskites with ferro-magnetism above room temperature", en, Journal of Physics: Condensed Matter **19**, Publisher: IOP Publishing, 023201 (2006).

70H. Kato, T. Okuda, Y. Okimoto, Y. Tomioka, Y. Takenoya, A. Ohkubo, M. Kawasaki, and Y. Tokura, "Metallic ordered double-perovskite Sr2CrReO6 with maximal Curie temperature of 635 K", Applied Physics Letters **81**, Publisher: American Institute of Physics, 328–330 (2002).

71M. K. Kim, J. Y. Moon, S. H. Oh, D. G. Oh, Y. J. Choi, and N. Lee, "Strong magnetoelectric coupling in mixed ferrimagnetic-multiferroic phases of a double perovskite", en, Scientific Reports **9**, 5456 (2019).

72R. Morrow, J. R. Soliz, A. J. Hauser, J. C. Gallagher, M. A. Susner, M. D. Sumption, A. A. Aczel, J. Yan, F. Yang, and P. M. Woodward, "The effect of chemical pressure on the structure and properties of A2CrOsO6 (A=Sr, Ca) ferrimagnetic double perovskite", en, Journal of Solid State Chemistry **238**, 46–52 (2016).

73Y. Izumiyama, Y. Doi, M. Wakeshima, Y. Hinatsu, Y. Shimojo, and Y. Morii, "Magnetic properties of the antiferromagnetic double perovskite Ba2PrRuO6", en, Journal of Physics: Condensed Matter **13**, Publisher: IOP Publishing, 1303–1313 (2001).

74J. Zhang, W.-J. Ji, J. Xu, X.-Y. Geng, J. Zhou, Z.-B. Gu, S.-H. Yao, and S.-T. Zhang, "Giant positive magnetoresistance in half-metallic double-perovskite Sr2CrWO6 thin films", en, Science Advances **3**, Publisher: American Association for the Advancement of Science Section: Research Article, e1701473 (2017).

75Y. Guo, L. Shi, S. Zhou, J. Zhao, and W. Liu, "Near room-temperature magnetoresistance effect in double perovskite La2NiMnO6", Applied Physics Letters **102**, Publisher: American Institute of Physics, 222401 (2013).

76H.-T. Jeng and G. Y. Guo, "First-principles investigations of orbital magnetic moments and electronic structures of the double perovskites Sr2FeMoO6, Sr2FeReO6 and Sr2CrWO6", Physical Review B **67**, Publisher: American Physical Society, 094438 (2003).

77E. Carvajal, R. Oviedo-Roa, M. Cruz-Irisson, and O. Navarro, "First-Principles Study of Fe-Mo Double Perovskites", en, Revista Mexicana de Física **58**, 4 (2012).

78C. J. Bartel, J. M. Clary, C. Sutton, D. Vigil-Fowler, B. R. Goldsmith, A. M. Holder, and C. B. Musgrave, "Inorganic Halide Double Perovskites with Optoelectronic Properties Modulated by Sublattice Mixing", Journal of the American Chemical Society **142**, Publisher: American Chemical Society, 5135–5145 (2020).

79L. Nordheim, German, Ann. Phys. **9** (1931).

80L. Bellaiche and D. Vanderbilt, "The virtual crystal approximation revisited: Application to dielectric and piezoelectric properties of perovskites", Physical Review B **61**, arXiv: cond-mat/9908364, 7877–7882 (2000).

[81] L. Ding, D. D. Khalyavin, P. Manuel, J. Blake, F. Orlandi, W. Yi, and A. A. Belik, "Colossal magnetoresistance in the insulating ferromagnetic double perovskites Tl2NiMnO6: A neutron diffraction study", Acta Materialia **173**, 20–26 (2019).

[82] W. E. Pickett and D. J. Singh, "Electronic structure and half-metallic transport in the La1-xCaxMnO3 system", Physical Review B **53**, Publisher: American Physical Society, 1146–1160 (1996).

[83] A. Bechiri, F. Benmakhlouf, and N. Bouarissa, "Band structure of III–V ternary semiconductor alloys beyond the VCA", en, Materials Chemistry and Physics **77**, 507–510 (2003).

[84] K. Kassali and N. Bouarissa, "Pseudopotential calculations of electronic properties of Ga1xInxN alloys with zinc-blende structure", Solid-State Electronics **44**, 501–507 (2000).

[85] N. Bouarissa, "The effect of compositional disorder on electronic band structure in GaxIn1xAsySb1yalloys lattice matched to GaSb", en, Superlattices and Microstructures **26**, 279–287 (1999).

[86] L. Bellaiche, S.-H. Wei, and A. Zunger, "Band gaps of GaPN and GaAsN alloys", Applied Physics Letters **70**, Publisher: American Institute of Physics, 3558–3560 (1997).

[87] L.-W. Wang, L. Bellaiche, S.-H. Wei, and A. Zunger, ""Majority Representation" of Alloy Electronic States", Physical Review Letters **80**, Publisher: American Physical Society, 4725–4728 (1998).

[88] C. Chen, E. G. Wang, Y. M. Gu, D. M. Bylander, and L. Kleinman, "Unexpected band-gap collapse in quaternary alloys at the group-III-nitride/GaAs interface: GaAlAsN", Physical Review B **57**, Publisher: American Physical Society, 3753–3756 (1998).

[89] S. de Gironcoli, P. Giannozzi, and S. Baroni, "Structure and thermodynamics of SixGe1-x alloys from ab initio Monte Carlo simulations", Physical Review Letters **66**, Publisher: American Physical Society, 2116–2119 (1991).

[90] N. Marzari, S. de Gironcoli, and S. Baroni, "Structure and phase stability of GaxIn1-x solid solutions from computational alchemy", Physical Review Letters **72**, Publisher: American Physical Society, 4001–4004 (1994).

[91] A. M. Saitta, S. de Gironcoli, and S. Baroni, "Structural and Electronic Properties of a Wide-Gap Quaternary Solid Solution: Zn, Mg,S, Se", Physical Review Letters **80**, Publisher: American Physical Society, 4939–4942 (1998).

[92] D. A. Papaconstantopoulos and W. E. Pickett, "Tight-binding coherent potential approximation study of ferromagnetic La2/3Ba1/3MnO3", Physical Review B **57**, Publisher: American Physical Society, 12751–12756 (1998).

[93] P. Slavenburg, "TiFe1-x Cox alloys and the influence of antistructural atoms", Physical Review B **55**, Publisher: American Physical Society, 16110–16121 (1997).

[94] N. J. Ramer and A. M. Rappe, "Virtual-crystal approximation that works: Locating a compositional phase boundary in PbZr1-xTixO3", Physical Review B **62**, Publisher: American Physical Society, R743–R746 (2000).

[95] A. J. Morris, R. J. Nicholls, C. J. Pickard, and Jonathan R. Yates, "The OptaDOS code", Comp. Phys. Comm. (2012).

[96] R. J. Nicholls, A. J. Morris, C. J. Pickard, and J. R. Yates, "OptaDOS - a new tool for EELS calculations", **371**, Conference Name: Journal of Physics Conference Series, 012062 (2012).

[97] H. Tan, H. Liu, Y. Li, W. Duan, and S. Zhang, "Understanding the origin of bandgap problem in transition and post-transition metal oxides", The Journal of Chemical Physics **151**, Publisher: American Institute of Physics, 124703 (2019).

[98] Y. Hinuma, G. Pizzi, Y. Kumagai, F. Oba, and I. Tanaka, "Band structure diagram paths based on crystallography", en, Computational Materials Science **128**, 140–184 (2017).

[99] A. Togo and I. Tanaka, "Spglib: a software library for crystal symmetry search", arXiv:1808.01590 [cond-mat], arXiv: 1808.01590 (2018).

[100] N. W. Ashcroft and N. D. Mermin, *Solid State Physics* (1976).

[101] J. Ziman, *Electrons and Phonons: The Theory of Transport Phenomena in Solids*, eng, Oxford Classic Texts in the Physical Sciences (Oxford University Press, Oxford, 2001).

[102] C. C. Hu, *Modern Semiconductor Devices for Integrated Circuits*, English (Pearson, 2009).

[103] B. V. Zeghbroeck, *The Principles of Semiconductor Devices* (2006).

[104] O. Kahn, *Molecular magnetism*, English (Wiley-VCH, New York (N.Y.), 1993).

[105] M. Verdaguer, "Rational synthesis of molecular magnetic materials:a tribute to Olivier Kahn", en, Polyhedron **20**, 1115–1128 (2001).

[106] S. Sharmin, A. Ardavan, S. J. Blundell, A. I. Coldea, E. J. L. McInnes, and D. Low, "Electron paramagnetic resonance studies of the high-spin molecule Cr10(OMe)20(O2CCMe3)10", en, Applied Physics Letters **86**, 032507 (2005).

[107] E. Coronado, "Molecular magnetism: from chemical design to spin control in molecules, materials and devices", en, Nature Reviews Materials **5**, 87–104 (2020).

[108] E. J. L. McInnes, C. Anson, A. K. Powell, A. J. Thomson, S. Poussereau, and R. Sessoli, "Solvothermal synthesis of [Cr10(-O2CMe)10(-OR)20] 'chromic wheels' with antiferromagnetic (R = Et) and ferromagnetic (R = Me) Cr(iii)···Cr(iii) interactions", en, Chemical Communications, 89–90 (2001).

[109] A. V. Postnikov, J. Kortus, and M. R. Pederson, "Density functional studies of molecular magnets", en, physica status solidi (b) **243**, 2533–2572 (2006).

[110] R. Georges, J. J. Borrás-Almenar, E. Coronado, J. Curély, and M. Drillon, "One-Dimensional Magnetism: An Overview of the Models", en, in *Magnetism: Molecules to Materials* (John Wiley & Sons, Ltd, 2004), pp. 1–47.

[111] M. Drillon, E. Coronado, D. Beltran, and R. Georges, "Classical treatment of a heisenberg linear chain with spin alternation; application to the MnNi(EDTA)-6H2O complex", en, Chemical Physics **79**, 449–453 (1983).

[112] J. Seiden, "Static properties of an alternating isotropic chain of 1/2 quantum spins and classical spins", fr, Journal de Physique Lettres **44**, Publisher: Les Editions de Physique, 947–952 (1983).

[113] E. Coronado, M. Drillon, P. R. Nugteren, L. J. De Jongh, D. Beltran, and R. Georges, "Low-temperature investigation of the ferrimagnetic chains MnM'6H2O [M' = cobalt, nickel, and copper(II)]: thermal and magnetic properties", Journal of the American Chemical Society **111**, Publisher: American Chemical Society, 3874–3880 (1989).

[114] H. Miyasaka, M. Julve, M. Yamashita, and R. Clérac, "Slow dynamics of the magnetization in one-dimensional coordination polymers: single-chain magnets", eng, Inorganic Chemistry **48**, 3420–3437 (2009).

[115] R. Sessoli, M.-E. Boulon, A. Caneschi, M. Mannini, L. Poggini, F. Wilhelm, and A. Rogalev, "Strong magneto-chiral dichroism in a paramagnetic molecular helix observed by hard X-ray", Nature physics **11**, 69–74 (2015).

[116] L. Thomas, F. Lionti, R. Ballou, D. Gatteschi, R. Sessoli, and B. Barbara, "Macroscopic quantum tunnelling of magnetization in a single crystal of nanomagnets", en, Nature **383**, Number: 6596 Publisher: Nature Publishing Group, 145–147 (1996).

[117] R. Sessoli, D. Gatteschi, A. Caneschi, and M. A. Novak, "Magnetic bistability in a metal-ion cluster", en, Nature **365**, Number: 6442 Publisher: Nature Publishing Group, 141–143 (1993).

[118] D. Shao and X.-Y. Wang, "Development of Single-Molecule Magnets", en, Chinese Journal of Chemistry **38**, 1005–1018 (2020).

[119] V. Bellini, A. Olivieri, and F. Manghi, "Density-functional study of the Cr 8 antiferromagnetic ring", en, Physical Review B **73**, 184431 (2006).

[120] M. Wojciechowski, B. Brzostowski, and G. Kamieniarz, "DFT Estimation of Exchange Coupling Constant of Cr $_8$ Molecular Ring using the Hybrid Functional B3LYP", en, Acta Physica Polonica A **127**, 407–409 (2015).

[121] B. Brzostowski, R. Lemański, T. Ślusarski, D. Tomecka, and G. Kamieniarz, "Chromium-based rings within the DFT and Falicov–Kimball model approach", en, Journal of Nanoparticle Research **15**, 1528 (2013).

[122] Zhurko G. A., *Chemcraft - graphical software for visualization of quantum chemistry computations*, 2005.

[123] J. v. Slageren, R. Sessoli, D. Gatteschi, A. A. Smith, M. Helliwell, R. E. P. Winpenny, A. Cornia, A.-L. Barra, A. G. M. Jansen, E. Rentschler, and G. A. Timco, "Magnetic Anisotropy of the Antiferromagnetic Ring [Cr8F8Piv16]", en, Chemistry – A European Journal **8**, 277–285 (2002).

[124] K. Schwarz and P. Mohn, "Itinerant metamagnetism in YCO2", en, Journal of Physics F: Metal Physics **14**, Publisher: IOP Publishing, L129–L134 (1984).

[125] A. V. Postnikov, G. Bihlmayer, and S. Blügel, "Exchange parameters in Fe-based molecular magnets", en, Computational Materials Science, Proceedings of the Second Conference of the Asian Consortium for Computational Materials Science — ACCMS-2 **36**, 91–95 (2006).

[126] E. Fohtung, "Magnetostriction Fundamentals", en, in *Reference Module in Materials Science and Materials Engineering* (Elsevier, Jan. 2021).

[127] P. B. Meisenheimer, R. A. Steinhardt, S. H. Sung, L. D. Williams, S. Zhuang, M. E. Nowakowski, S. Novakov, M. M. Torunbalci, B. Prasad, C. J. Zollner, Z. Wang, N. M. Dawley, J. Schubert, A. H. Hunter, S. Manipatruni, D. E. Nikonov, I. A. Young, L. Q. Chen, J. Bokor, S. A. Bhave, R. Ramesh, J.-M. Hu, E. Kioupakis, R. Hovden, D. G. Schlom, and J. T. Heron, "Engineering new limits to magnetostriction through metastability in iron-gallium alloys", en, Nature Communications **12**, Number: 1 Publisher: Nature Publishing Group, 2757 (2021).

[128] R. Q. Wu, L. J. Chen, A. Shick, and A. J. Freeman, "First-principles determinations of magneto-crystalline anisotropy and magnetostriction in bulk and thin-film transition metals", en, Journal of Magnetism and Magnetic Materials, International Conference on Magnetism (Part II) **177-181**, 1216–1219 (1998).

[129] D. I. Bower and L. F. Bates, "The magnetostriction coefficients of nickel", Proceedings of the Royal Society of London. A. Mathematical and Physical Sciences **326**, Publisher: Royal Society, 87–96 (1971).

[130] A. C. Tam and H. Schroeder, "Precise measurements of a magnetostriction coefficient of a thin soft-magnetic film deposited on a substrate", Journal of Applied Physics **64**, Publisher: American Institute of Physics, 5422–5424 (1988).

[131] R. M. Martin, *Electronic Structure: Basic Theory and Practical Methods* (Cambridge University Press, Cambridge, 2004).

[132] Philip Peter Rushton, "Towards a Non-Local Density Functional Description of Exchange and Correlation", English, PhD thesis (University of Durham, Nov. 2002).

[133] Y. Yamamoto, A. Salcedo, C. M. Diaz, M. S. Alam, T. Baruah, and R. R. Zope, "Comparison of regularized SCAN functional with SCAN functional with and without self-interaction for a wide-array of properties", arXiv:2004.13393 [cond-mat, physics:physics], arXiv: 2004.13393 (2020).

[134] E. Bellido, P. González-Monje, A. Repollés, M. Jenkins, J. Sesé, D. Drung, T. Schurig, K. Awaga, F. Luis, and D. Ruiz-Molina, "Mn 12 single molecule magnets deposited on -SQUID sensors: the role of interphases and structural modifications", en, Nanoscale **5**, Publisher: Royal Society of Chemistry, 12565–12573 (2013).

[135] R. W. Saalfrank, A. Scheurer, I. Bernt, F. W. Heinemann, A. V. Postnikov, V. Schünemann, A. X. Trautwein, M. S. Alam, H. Rupp, and P. Müller, "The {FeIII[FeIII(L1)2]3} star-type single-molecule magnet", en, Dalton Transactions, Publisher: The Royal Society of Chemistry, 2865–2874 (2006).

[136]R. S. Edwards, S. Maccagnano, E.-C. Yang, S. Hill, W. Wernsdorfer, D. Hendrickson, and G. Christou, "High-frequency electron paramagnetic resonance investigations of tetranuclear nickel-based single-molecule magnets", Journal of Applied Physics **93**, Publisher: American Institute of Physics, 7807–7809 (2003).

[137]A. Ferguson, J. Lawrence, A. Parkin, J. Sanchez-Benitez, K. V. Kamenev, E. K. Brechin, W. Wernsdorfer, S. Hill, and M. Murrie, "Synthesis and characterisation of a Ni4 single-molecule magnet with S4 symmetry", en, Dalton Transactions, Publisher: The Royal Society of Chemistry, 6409–6414 (2008).

[138]Y. Kamihara, T. Watanabe, M. Hirano, and H. Hosono, "Iron-Based Layered Superconductor La[O1-xFx]FeAs (x = 0.050.12) with Tc = 26 K", Journal of the American Chemical Society **130**, Publisher: American Chemical Society, 3296–3297 (2008).

[139]M. R. Norman, "High-temperature superconductivity in the iron pnictides", en, Physics **1**, Publisher: American Physical Society (2008).

[140]C. Wang, L. Li, S. Chi, Z. Zhu, Z. Ren, Y. Li, Y. Wang, X. Lin, Y. Luo, S. Jiang, X. Xu, G. Cao, and Z. Xu, "Thorium-doping–induced superconductivity up to 56 0.167emK in Gd 1-x Th x FeAsO", en, EPL (Europhysics Letters) **83**, Publisher: IOP Publishing, 67006 (2008).

[141]Z. P. Yin, S. Lebègue, M. J. Han, B. P. Neal, S. Y. Savrasov, and W. E. Pickett, "Electron-Hole Symmetry and Magnetic Coupling in Antiferromagnetic LaFeAsO", Physical Review Letters **101**, Publisher: American Physical Society, 047001 (2008).

[142]D. N. Basov and A. V. Chubukov, "Manifesto for a higher T c", en, Nature Physics **7**, Bandiera_abtest: a Cg_type: Nature Research Journals Number: 4 Primary_atype: Reviews Publisher: Nature Publishing Group, 272–276 (2011).

[143]K. Ishida, Y. Nakai, and H. Hosono, "To What Extent Iron-Pnictide New Superconductors Have Been Clarified: A Progress Report", Journal of the Physical Society of Japan **78**, Publisher: The Physical Society of Japan, 062001 (2009).

[144]S. Nandi, M. G. Kim, A. Kreyssig, R. M. Fernandes, D. K. Pratt, A. Thaler, N. Ni, S. L. Bud'ko, P. C. Canfield, J. Schmalian, R. J. McQueeney, and A. I. Goldman, "Anomalous Suppression of the Orthorhombic Lattice Distortion in Superconducting BaFe(1-x)Co(x2)As2 Single Crystals", Physical Review Letters **104**, Publisher: American Physical Society, 057006 (2010).

[145]D. Parker and I. I. Mazin, "Non-nesting spin-density-wave antiferromagnetism in FeAs from first principles", Physical Review B **83**, Publisher: American Physical Society, 180403 (2011).

[146]S. M. Griffin and N. A. Spaldin, "A density functional theory study of the influence of exchange-correlation functionals on the properties of FeAs", en, Journal of Physics: Condensed Matter **29**, 215604 (2017).

[147]M. M. Korshunov and I. Eremin, "Theory of magnetic excitations in iron-based layered superconductors", Physical Review B **78**, Publisher: American Physical Society, 140509 (2008).

[148]T. A. Maier and D. J. Scalapino, "Theory of neutron scattering as a probe of the superconducting gap in the iron pnictides", Physical Review B **78**, Publisher: American Physical Society, 020514 (2008).

[149]T. Yildirim, "Strong Coupling of the Fe-Spin State and the As-As Hybridization in Iron-Pnictide Superconductors from First-Principle Calculations", Physical Review Letters **102**, Publisher: American Physical Society, 037003 (2009).

[150]K. Selte, A. Kjekshus, A. F. Andresen, M. J. Tricker, and S. Svensson, "Magnetic Structure and Properties of FeAs.", en, Acta Chemica Scandinavica **26**, 3101–3113 (1972).

[151]K. Segawa and Y. Ando, "Magnetic and Transport Properties of FeAs Single Crystals", Journal of the Physical Society of Japan **78**, Publisher: The Physical Society of Japan, 104720 (2009).

[152]A. Blachowski, K. Ruebenbauer, J. Zukrowski, and Z Bukowski, *Magnetic anisotropy and lattice dynamics in FeAs studied by Mossbauer spectroscopy — Elsevier Enhanced Reader*, en.

[153]E. E. Rodriguez, C. Stock, K. L. Krycka, C. F. Majkrzak, P. Zajdel, K. Kirshenbaum, N. P. Butch, S. R. Saha, J. Paglione, and M. A. Green, "Noncollinear spin-density-wave antiferromagnetism in FeAs", en, Physical Review B **83**, 134438 (2011).

[154]F.-C. Hsu, J.-Y. Luo, K.-W. Yeh, T.-K. Chen, T.-W. Huang, P. M. Wu, Y.-C. Lee, Y.-L. Huang, Y.-Y. Chu, D.-C. Yan, and M.-K. Wu, "Superconductivity in the PbO-type structure alpha-FeSe", eng, Proceedings of the National Academy of Sciences of the United States of America **105**, 14262–14264 (2008).

[155]M. K. Wu, F. C. Hsu, K. W. Yeh, T. W. Huang, J. Y. Luo, M. J. Wang, H. H. Chang, T. K. Chen, S. M. Rao, B. H. Mok, C. L. Chen, Y. L. Huang, C. T. Ke, P. M. Wu, A. M. Chang, C. T. Wu, and T. P. Perng, "The development of the superconducting PbO-type -FeSe and related compounds", en, Physica C: Superconductivity, Superconductivity in Iron-Pnictides **469**, 340–349 (2009).

[156]Y. Mizuguchi and Y. Takano, "Review of Fe Chalcogenides as the Simplest Fe-Based Superconductor", Journal of the Physical Society of Japan **79**, Publisher: The Physical Society of Japan, 102001 (2010).

[157]D. J. Singh, "Superconductivity and magnetism in 11-structure iron chalcogenides in relation to the iron pnictides", Science and Technology of Advanced Materials **13**, Publisher: Taylor & Francis _eprint: https://doi.org/10.1088/1468-6996/13/5/054304, 054304 (2012).

[158]L. Malavasi and S. Margadonna, "Structure–properties correlations in Fe chalcogenide superconductors", en, Chemical Society Reviews **41**, Publisher: The Royal Society of Chemistry, 3897–3911 (2012).

[159]S. Medvedev, T. M. McQueen, I. A. Troyan, T. Palasyuk, M. I. Eremets, R. J. Cava, S. Naghavi, F. Casper, V. Ksenofontov, G. Wortmann, and C. Felser, "Electronic and magnetic phase diagram of beta-Fe(1.01)Se with superconductivity at 36.7 K under pressure", eng, Nature Materials **8**, 630–633 (2009).

[160] S. Margadonna, Y. Takabayashi, M. T. McDonald, K. Kasperkiewicz, Y. Mizuguchi, Y. Takano, A. N. Fitch, E. Suard, and K. Prassides, "Crystal structure of the new FeSe1x superconductor", en, Chemical Communications, Publisher: The Royal Society of Chemistry, 5607–5609 (2008).

[161] J. P. Sun, K. Matsuura, G. Z. Ye, Y. Mizukami, M. Shimozawa, K. Matsubayashi, M. Yamashita, T. Watashige, S. Kasahara, Y. Matsuda, J.-Q. Yan, B. C. Sales, Y. Uwatoko, J.-G. Cheng, and T. Shibauchi, "Dome-shaped magnetic order competing with high-temperature superconductivity at high pressures in FeSe", eng, Nature Communications **7**, 12146 (2016).

[162] S. Kasahara, T. Watashige, T. Hanaguri, Y. Kohsaka, T. Yamashita, Y. Shimoyama, Y. Mizukami, R. Endo, H. Ikeda, K. Aoyama, T. Terashima, S. Uji, T. Wolf, H. v. Löhneysen, T. Shibauchi, and Y. Matsuda, "Field-induced superconducting phase of FeSe in the BCS-BEC cross-over", en, Proceedings of the National Academy of Sciences **111**, Publisher: National Academy of Sciences Section: Physical Sciences, 16309–16313 (2014).

[163] A. E. Böhmer, F. Hardy, F. Eilers, D. Ernst, P. Adelmann, P. Schweiss, T. Wolf, and C. Meingast, "Lack of coupling between superconductivity and orthorhombic distortion in stoichiometric single-crystalline FeSe", Physical Review B **87**, Publisher: American Physical Society, 180505 (2013).

[164] Q. Wang, Y. Shen, B. Pan, Y. Hao, M. Ma, F. Zhou, P. Steffens, K. Schmalzl, T. R. Forrest, M. Abdel-Hafiez, D. A. Chareev, A. N. Vasiliev, P. Bourges, Y. Sidis, H. Cao, and J. Zhao, "Strong Interplay between Stripe Spin Fluctuations, Nematicity and Superconductivity in FeSe", Nature Materials **15**, arXiv: 1502.07544, 159–163 (2016).

[165] Q. Wang, Y. Shen, B. Pan, X. Zhang, K. Ikeuchi, K. Iida, A. D. Christianson, H. C. Walker, D. T. Adroja, M. Abdel-Hafiez, X. Chen, D. A. Chareev, A. N. Vasiliev, and J. Zhao, "Magnetic ground state of FeSe", en, Nature Communications **7**, 12182 (2016).

[166] T. Frawley, R. Schoonmaker, S. H. Lee, C.-H. Du, P. Steadman, J. Strempfer, K. A. Ziq, S. J. Clark, T. Lancaster, and P. D. Hatton, "Elucidation of the helical spin structure of FeAs", en, Physical Review B **95**, 064424 (2017).

[167] F. Ma, W. Ji, J. Hu, Z.-Y. Lu, and T. Xiang, "First-Principles Calculations of the Electronic Structure of Tetragonal -FeTe and -FeSe Crystals: Evidence for a Bicollinear Antiferromagnetic Order", en, Physical Review Letters **102**, 177003 (2009).

[168] A. Subedi, L. Zhang, D. J. Singh, and M. H. Du, "Density functional study of FeS, FeSe, and FeTe: Electronic structure, magnetism, phonons, and superconductivity", Physical Review B **78**, Publisher: American Physical Society, 134514 (2008).

[169] J. Maletz, V. B. Zabolotnyy, D. V. Evtushinsky, S. Thirupathaiah, A. U. B. Wolter, L. Harnagea, A. N. Yaresko, A. N. Vasiliev, D. A. Chareev, A. E. Böhmer, F. Hardy, T. Wolf, C. Meingast, E. D. L. Rienks, B. Büchner, and S. V. Borisenko, "Unusual band renormalization in the simplest iron-based superconductor FeSe1-x", Physical Review B **89**, Publisher: American Physical Society, 220506 (2014).

[170] H. Eschrig and K. Koepernik, "Tight-binding models for the iron-based superconductors", Physical Review B **80**, Publisher: American Physical Society, 104503 (2009).

[171] M. D. Watson, T. K. Kim, A. A. Haghighirad, N. R. Davies, A. McCollam, A. Narayanan, S. F. Blake, Y. L. Chen, S. Ghannadzadeh, A. J. Schofield, M. Hoesch, C. Meingast, T. Wolf, and A. I. Coldea, "Emergence of the nematic electronic state in FeSe", Physical Review B **91**, Publisher: American Physical Society, 155106 (2015).

[172] K. Selte, A. Kjekshus, J. Sletten, L. Torbjörnsson, P.-E. Werner, U. Junggren, B. Lamm, and B. Samuelsson, "The Crystal Structure of FeAs.", en, Acta Chemica Scandinavica **23**, 2047–2054 (1969).

[173] P. S. Lyman and C. T. Prewitt, "Room- and high-pressure crystal chemistry of CoAs and FeAs", en, Acta Crystallographica Section B: Structural Science **40**, Number: 1 Publisher: International Union of Crystallography, 14–20 (1984).

[174] A. Baum, H. N. Ruiz, N. Lazarević, Y. Wang, T. Böhm, R. Hosseinian Ahangharnejhad, P. Adelmann, T. Wolf, Z. V. Popović, B. Moritz, T. P. Devereaux, and R. Hackl, "Frustrated spin order and stripe fluctuations in FeSe", en, Communications Physics **2**, 1–7 (2019).

[175] P. Kratzer and J. Neugebauer, "The Basics of Electronic Structure Theory for Periodic Systems", Frontiers in Chemistry **7**, 106 (2019).

[176] J. Aarons, M. Sarwar, D. Thompsett, and C.-K. Skylaris, "Perspective: Methods for large-scale density functional calculations on metallic systems", en, The Journal of Chemical Physics **145**, 220901 (2016).

[177] D. J. Campbell, C. Eckberg, K. Wang, L. Wang, H. Hodovanets, D. Graf, D. Parker, and J. Paglione, "Quantum Oscillations in the Anomalous Spin Density Wave State of FeAs", Physical Review B **96**, arXiv: 1703.03833, 075120 (2017).

[178] Luke Charles Rhodes, "Theoretical and experimental study of the electronic structure of FeSe", English, PhD thesis (Royal Holloway, University of London, 2019).

[179] I. I. Mazin, M. D. Johannes, L. Boeri, K. Koepernik, and D. J. Singh, "Problems with reconciling density functional theory calculations with experiment in ferropnictides", Physical Review B **78**, Publisher: American Physical Society, 085104 (2008).

[180] Y. Fu and D. J. Singh, "Density functional methods for the magnetism of transition metals: SCAN in relation to other functionals", en, Physical Review B **100**, 045126 (2019).

[181] J. M. Ok, S.-H. Baek, C. Hoch, R. K. Kremer, S. Y. Park, S. Ji, B. Büchner, J.-H. Park, S. I. Hyun, J. H. Shim, Y. Bang, E. G. Moon, I. I. Mazin, and J. S. Kim, "Frustration-driven C 4 symmetry order in a naturally-heterostructured superconductor Sr2VO3FeAs", en, Nature Communications **8**, 2167 (2017).

[182] A. Kreisel, S. Mukherjee, P. J. Hirschfeld, and B. M. Andersen, "Spin excitations in a model of FeSe with orbital ordering", Physical Review B **92**, arXiv: 1510.02357, 224515 (2015).

# Appendix A

# Proof of The Allowed N-Fold axes

Allow the principal axis for rotation to be the Z-axis. The point

$$\mathbf{r} = x\hat{\mathbf{i}} + y\hat{\mathbf{j}} + z\hat{\mathbf{k}}$$

can rotate by $\theta$ to produce the point

$$\mathbf{r}' = (x\cos(\theta) - y\sin(\theta))\hat{\mathbf{i}} + (x\sin(\theta) + y\cos(\theta))\hat{\mathbf{j}} + z\hat{\mathbf{k}}.$$

In matrix formulation, the point $\mathbf{r}$ becomes:

$$\mathbf{r} = \begin{pmatrix} x \\ y \\ z \end{pmatrix}$$

The rotation matrix ($\mathbf{R}$) represents the rotation of of the point $\mathbf{r}$ by $\theta$:

$$\mathbf{R} = \begin{pmatrix} \cos(\theta) & -\sin(\theta) & 0 \\ \sin(\theta) & \cos(\theta) & 0 \\ 0 & 0 & 1 \end{pmatrix}$$

to produce the point

$$\mathbf{r}' = \begin{pmatrix} x\cos(\theta) - y\sin(\theta) \\ x\sin(\theta) + y\cos(\theta) \\ z \end{pmatrix} = \begin{pmatrix} x' \\ y' \\ z' \end{pmatrix} = \mathbf{R}\mathbf{r}$$

The structure of the molecule remains unchanged for any n-fold rotation axis through the angle $\theta = \frac{2\pi}{n}$.

For a crystal, the $\hat{\mathbf{i}}, \hat{\mathbf{j}}, \hat{\mathbf{k}}$ directions are better suited as the Bravais lattice vectors $a_1, a_2$ and $a_3$ in the directions $x, y, z$.

$$\mathbf{a}_1 = a_{1x}\hat{\mathbf{i}} + a_{1y}\hat{\mathbf{j}} + a_{1z}\hat{\mathbf{k}}$$

$$\mathbf{a}_2 = a_{2x}\hat{\mathbf{i}} + a_{2y}\hat{\mathbf{j}} + a_{2z}\hat{\mathbf{k}}$$

$$\mathbf{a}_3 = a_{3x}\hat{\mathbf{i}} + a_{3y}\hat{\mathbf{j}} + a_{3z}\hat{\mathbf{k}}$$

These vectors are linearly independent and, therefore, span over all space. The matrix, A, containing all elements of $a_1, a_2$ and $a_3$:

$$A = \begin{pmatrix} a_{1x} & a_{1y} & a_{1z} \\ a_{2x} & a_{2y} & a_{2z} \\ a_{3x} & a_{3y} & a_{3z} \end{pmatrix}$$

Matrix A has an inverse as $\det(A) = \mathbf{a}_1 \cdot (\mathbf{a}_2 \times \mathbf{a}_3) \neq 0$. The position vector $\mathbf{r} = x\hat{\mathbf{i}} + y\hat{\mathbf{j}} + z\hat{\mathbf{k}}$ can then be redefined as $c_1\mathbf{a}_1 + c_2\mathbf{a}_2 + c_3\mathbf{a}_3$, which satisfies:

$$A \begin{pmatrix} c_1 \\ c_2 \\ c_3 \end{pmatrix} = \begin{pmatrix} x \\ y \\ z \end{pmatrix}$$

Applying this redefinition to the rotation $\mathbf{R} \begin{pmatrix} x \\ y \\ z \end{pmatrix} = \begin{pmatrix} x' \\ y' \\ z' \end{pmatrix}$, the points $r, r'$ becomes:

$$r = c_1\mathbf{a}_1 + c_2\mathbf{a}_2 + c_3\mathbf{a}_3$$

$$r' = c_1'\mathbf{a}_1 + c_2'\mathbf{a}_2 + c_3'\mathbf{a}_3$$

Therefore,

$$R \begin{pmatrix} x \\ y \\ z \end{pmatrix} = \begin{pmatrix} x' \\ y' \\ z' \end{pmatrix} \implies RA \begin{pmatrix} c_1 \\ c_2 \\ c_3 \end{pmatrix} = A \begin{pmatrix} c'_1 \\ c'_2 \\ c'_3 \end{pmatrix} \implies A^{-1}RA \begin{pmatrix} c_1 \\ c_2 \\ c_3 \end{pmatrix} = \begin{pmatrix} c'_1 \\ c'_2 \\ c'_3 \end{pmatrix}$$

With

$$Tr(R_A) = 1 + 2cos(\theta)$$

Whereby $R_A = A^{-1}RA$.

For the rotation to keep the crystal unperturbed, the lattice point $a_1$ must rotate onto a point $n_1a_1 + n_2a_2 + n_3a_3$ with integer values of $a_1, a_2$ and $a_3$. As a result:

$$R_A = \begin{pmatrix} 1 \\ 0 \\ 0 \end{pmatrix} = \begin{pmatrix} n_1 \\ n_2 \\ n_3 \end{pmatrix}$$

Where the coefficients $c_1 = 1, c_2 = 0, c_3 = 0$ and $c'_{1,2,3} = n_{1,2,3}$. From this, the trace of $R_A$ is also an integer. The values of $cos(\theta)$ are bound between -1 and 1. Simultaneously, the values of $1 + 2cos(\theta)$ are only defined between -1 and 3. Mapping out all the integer values within this interval provides:

$$-1 = 1 + 2cos(\theta) \therefore \theta = \pi$$
$$0 = 1 + 2cos(\theta) \therefore \theta = \frac{2\pi}{3}$$
$$1 = 1 + 2cos(\theta) \therefore \theta = \frac{\pi}{2}$$
$$2 = 1 + 2cos(\theta) \therefore \theta = \frac{\pi}{3}$$
$$3 = 1 + 2cos(\theta) \therefore \theta = 2\pi$$

Therefore n, respectively, becomes:

$$n = \frac{2\pi}{\pi} = 2$$
$$n = \frac{2\pi}{\frac{2\pi}{3}} = 3$$
$$n = \frac{2\pi}{\frac{\pi}{2}} = 4$$
$$n = \frac{2\pi}{\frac{\pi}{3}} = 6$$
$$n = \frac{2\pi}{2\pi} = 1$$

Thus, the allowed n-fold axes do not include a 5-fold axis.

# Appendix B

# Ionic Constraints

Boron Trifluoride The $Cr_{10}$ molecule is complex, and to determine the methodology of ionic constraints, a more straightforward choice of system was the Boron Trifluoride ($BF_3$) molecule. This system comprises a central Bromine ion with three Florine ions bonded in a planar triangular fashion, as seen in Figure B.1. The symmetry of the $BF_3$ molecule is a $D_{3h}$ point group. This symmetry group encapsulates a $C_3$ rotation, with the z-axis as the primary axis, running through the Bromine ion and orthogonal to the molecule's planar nature. A $C_2$ rotation axis is in line with B-F bonds on each of the Florine ions, totalling three unique $C_2$ rotations perpendicular to the $C_3$ rotation axis. The molecule rests with the x-axis running through the Bromine and a Florine ion, as seen in Figure B.1, making the rotation matrices easier to utilise.
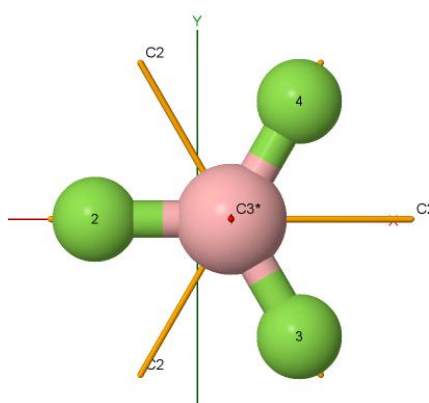


Figure B.1: The $BF_3$ molecule, with the $D_{3h}$ symmetry operations visible. The Boron ion is pink (displaced to allow for clarity of z-axis) and the Flourine ions are the green.

The $C_2$ rotation matrix along the x-axis and $C_3$ rotation matrix along the z-axis, respectively, take the forms:

$$C_2 = \begin{pmatrix} 1 & 0 & 0 \\ 0 & \cos{(\pi)} & -\sin{(\pi)} \\ 0 & \sin{(\pi)} & \cos{(\pi)} \end{pmatrix} = \begin{pmatrix} 1 & 0 & 0 \\ 0 & -1 & 0 \\ 0 & 0 & -1 \end{pmatrix}$$

$$C_3 = \begin{pmatrix} \cos{(\frac{2\pi}{3})} & -\sin{(\frac{2\pi}{3})} & 0 \\ \sin{(\frac{2\pi}{3})} & \cos{(\frac{2\pi}{3})} & 0 \\ 0 & 0 & 1 \end{pmatrix} = \begin{pmatrix} -\frac{1}{2} & -\frac{\sqrt{3}}{2} & 0 \\ \frac{\sqrt{3}}{2} & -\frac{1}{2} & 0 \\ 0 & 0 & 1 \end{pmatrix} \quad \text{(B.0.1)}$$

The maximum number of allowed constraints to employ is 4×3=12, due to the number of degrees of freedom, 3N, and the total number of ions, four. There are two other $C_2$ rotation axes in the molecule, intersecting the F ions, four and three; see Figure B.1. Making a total of three $C_2$ axes, implementing all of the x,y,z constraints would exceed the total number of constraints allowed. Due to this molecule's planar nature, there is no reason to optimise this molecule in the z-direction; therefore, the ions' z-coordinates can remain unchanged. Fixing these z-coordinates in place decreases the number of constraints as they only need to be mentioned four times. Further to this, the boron ion exists in all three rotation axes as stationary; therefore, both the x- and y- coordinates do not need to change, and the boron ion can be constrained not to move. Thus, reducing further the number of constraints required.

To represent the $C_2$ rotation axes that do not lie on the x-axis but intersect the F ions, three and four, the $C_3$ rotation around the z-axis combined with the x-axis $C_2$ symmetry operator generates them. The reason for this rests in the angular difference between the $C_2$ rotation axes $(\frac{2\pi}{3}^{rads})$. This difference corresponds to a $C_3$ rotation. Multiplying the transpose of the $C_3$ rotation matrix with the $C_2$ matrix and then multiplying the result with the $C_3$

rotation matrix will provide the shifted $C_{2\theta\text{CCW}}$ rotation axis, Equation B.0.2 (right to left) , which goes through the Florine ion counter-clockwise to the x-axis (ion three).

$$C_{2\theta\text{CCW}} = C_3 \times C_2 \times C_3^{\mathsf{T}} \tag{B.0.2}$$

therefore,

$$C_{2\theta\text{CCW}} = \begin{pmatrix} -\frac{1}{2} & \frac{\sqrt{3}}{2} & 0 \\ \frac{\sqrt{3}}{2} & \frac{1}{2} & 0 \\ 0 & 0 & -1 \end{pmatrix}$$

Implicitly included in the new $C_{2\theta\text{CCW}}$ rotation matrix is the $C_3$ rotation due to the use of the $C_3$ rotation matrix to shift the axis.

Shifting the $C_2$ axis clockwise around the molecule employs the same method as the counter-clockwise $C_{2\theta\text{CCW}}$ rotation matrix. However, we first multiple the $C_2$ rotation matrix by the $C_3$ rotation matrix, then multiply the result by the transpose of the $C_3$ rotation matrix, which provides the clockwise shifted $C_2$ rotation matrix, $C_{2\theta\text{CW}}$ – See Equation B.0.3 (right to left).

$$C_{2\theta CW} = C_3^{\mathsf{T}} \times C_2 \times C_3 \tag{B.0.3}$$

therefore,

$$C_{2\theta CW} = \begin{pmatrix} -\frac{1}{2} & -\frac{\sqrt{3}}{2} & 0 \\ -\frac{\sqrt{3}}{2} & \frac{1}{2} & 0 \\ 0 & 0 & -1 \end{pmatrix}$$

With the three rotation matrices, all of the symmetry operation in the $BF_3$ molecule are either explicitly or implicitly represented. Enforcing these rotations via constraints requires the correct permutation for each of the symmetry axes, see Tables B.1-B.3.

| Initial Ion's Number | Rotated Pair |
|:---:|:---:|
| 2 | 2 |
| 4 | 3 |

Table B.1: The rotated pairs of F ions following the $C_2$ symmetry operation around the x-axis.

| Initial Ion's Number | Rotated Pair |
| --- | --- |
| 3 | 3 |
| 4 | 2 |

Table B.2: The rotated pairs of F ions following the $C_{2\theta CCW}$ symmetry operation around the axes intersecting the third F ion.

| Initial Ion's Number | Rotated Pair |
| --- | --- |
| 4 | 4 |
| 2 | 3 |

Table B.3: The rotated pairs of F ions following the $C_{2\theta CW}$ symmetry operation around the axes intersecting the fourth F ion.

These permutations allow for the removed constraints not to affect the same mapped ions, which would under constrain the molecule. Likewise, it allows for the determination and subsequent removal of any constraints which describe the same rotation and cause linear dependency. The constraints that describe all three of the rotations, $C_2$, $C_{2\theta CCW}$ and $C_{2\theta CW}$ , generate linear dependency due to the two shifted C2 axes' inclusion. Removing either one of them removes this and allows for the molecule's symmetry to be upheld.

# Appendix C
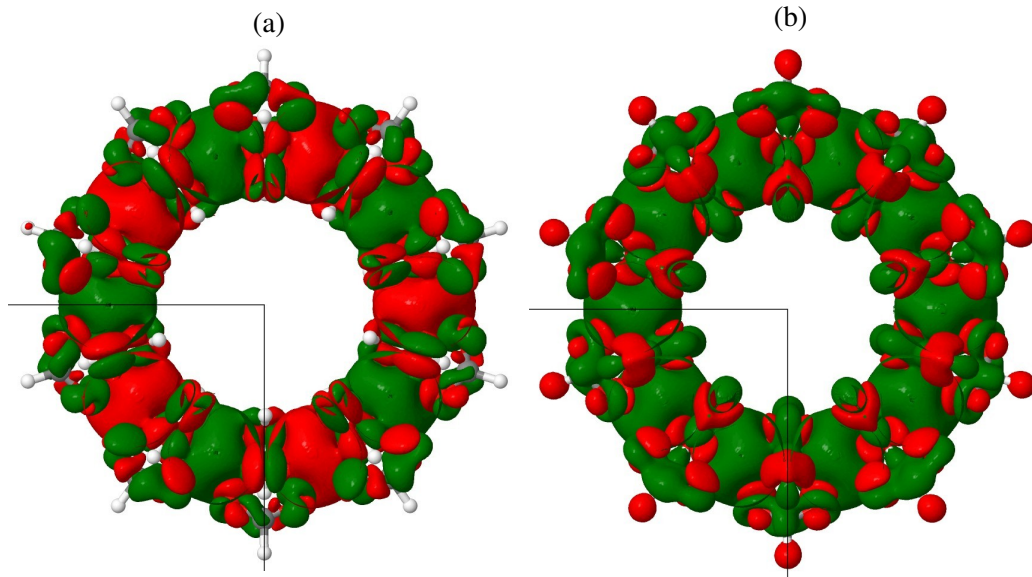
# Isosurfaces of Cr$_{10}$ Molecule



Figure C.1: The Fixed Spin Moment spin density for the AFM (S=0$\mu_B$) (a) and FM (S=30$\mu_B$) (b) states for the LDA XC-functional. Whereby red isosurfaces represent spin down densities and green isosurfaces represent spin up densities.
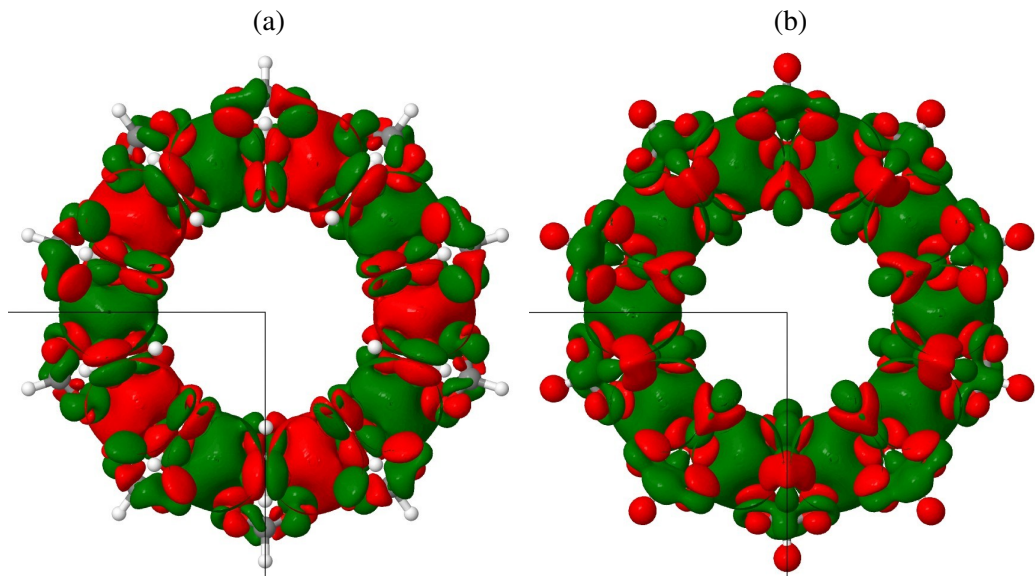
Figure C.2: The Fixed Spin Moment spin density for the AFM (S=0$\mu_B$) (a) and FM (S=30$\mu_B$) (b) states for the PBE XC-functional. Whereby red isosurfaces represent spin down densities and green isosurfaces represent spin up densities.